UNIVERSITY OF CALIFORNIA,
IRVINE

Identifying Quantitative Biomarkers in Electroencephalogram for the Evaluation of Developmental and Epileptic Encephalopathies

DISSERTATION

submitted in partial satisfaction of the requirements
for the degree of

DOCTOR OF PHILOSOPHY

in Biomedical Engineering

by

Derek Kuan-Yu Hu

Dissertation Committee:
Associate Professor Beth A. Lopour, Chair
Professor Frithjof Kruggel
Professor Ramesh Srinivasan

2023

DEDICATION

To

my parents, Pony Ma and Paul Hu,
who have provided me with every bit of love and support in my journeys,

my principle investigator, Beth Lopour,
who has offered me the greatest mentorship and care,

and my colleagues and friends,
who have provided solace, encouragement, and a place to call home,

I sincerely thank you all.

TABLE OF CONTENTS

	Page
LIST OF FIGURES	iv
LIST OF TABLES	vi
ACKNOWLEDGEMENTS	vii
VITA	viii
ABSTRACT OF THE DISSERTATION	ix
CHAPTER I: Background	1
CHAPTER II: Evolution of cortical functional networks in healthy infants	18
CHAPTER III: Effect of interictal epileptiform discharges on EEG-based functional connectivity networks	44
CHAPTER IV: Interrater reliability of interictal EEG waveforms in Lennox-Gastaut syndrome	67
CHAPTER V: Discovering EEG biomarkers of Lennox-Gastaut syndrome through unsupervised time-frequency image analysis	87
REFERENCES	117

LIST OF FIGURES

		Page
Figure 2.1	The effect of edge density on in graph theory measures in broadband functional connectivity	28
Figure 2.2	The effect of edge density on in graph theory measures in delta functional connectivity	28
Figure 2.3	The effect of edge density on in graph theory measures in theta functional connectivity	29
Figure 2.4	The effect of edge density on in graph theory measures in alpha functional connectivity	29
Figure 2.5	The effect of edge density on in graph theory measures in beta functional connectivity	30
Figure 2.6	Mean cross-correlation functional connectivity for healthy infants	31
Figure 2.7	Mean network strength by age in cross-correlation connectivity	31
Figure 2.8	Mean wPLI functional connectivity for healthy infants	33
Figure 2.9	Mean network strength by age in wPLI connectivity	34
Figure 2.10	Graph theory measures as a function of age in cross-correlation	35
Figure 2.11	Small-world measure in wPLI connectivity	36
Figure 2.12	Normalized global clustering coefficient in wPLI connectivity	36
Figure 2.13	Normalized characteristic path length in wPLI connectivity	37
Figure 3.1	Summary of the functional connectivity analysis	46
Figure 3.2	Sample of EEG data segmentation	47
Figure 3.3	Morphology of the simulated IED	49
Figure 3.4	Representative example of FCNs with different simulated IEDs amplitude	54
Figure 3.5	Effect of spike amplitude on 2D correlation and connectivity strength	55
Figure 3.6	Representative example of FCNs with different simulated IED burden	56

Figure 3.7	Effect of spike burden on 2D correlation and connectivity strength	56
Figure 3.8	2D correlation coefficient between control and IS patient groups	57
Figure 3.9	Relative graph edit distance for intra-subject network comparisons	59
Figure 3.10	2D correlation coefficients for all intra-subject network comparisons	60
Figure 4.1	A representative example of event identification	72
Figure 4.2	Examples of TFIs and time-varying power spectrum features	72
Figure 4.3	An example of the blinded visual analysis of an EEG event	74
Figure 4.4	Different event detection thresholds yielded similar cluster centroids	76
Figure 4.5	Heatmap of the number of events in each cluster for control and LGS subjects	77
Figure 4.6	Radar plots of the different feature values for each cluster centroid	78
Figure 4.7	Confusion matrix for event classification	80
Figure 4.8	Confusion matrix for pathological, physiological, and other groups	84
Figure 5.1	An example of EOI identification	95
Figure 5.2	Examples of EOIs with different feature values	96
Figure 5.3	Normalized histograms of events in each feature	99
Figure 5.4	Normalized histograms of events with different power thresholds	100
Figure 5.5	Event distribution of clusters primarily originating from LGS subjects	101
Figure 5.6	Mean cluster centroid values for each feature	102
Figure 5.7	Mean cluster centroid values using different event detection thresholds	102
Figure 5.8	Mean cluster centroid values using a different number of clusters	103
Figure 5.9	Breakdown of reviewer classification in clusters containing significantly more LGS events than control events	106
Figure 5.10	Mean features of automatically detected sleep spindles	107

LIST OF TABLES

		Page
Table 2.1	Demographics for healthy participants	20
Table 2.2	Mean EEG, artifact, wake, and sleep duration for each age group	22
Table 2.3	Mean percentage of artifact, wake, and N2 sleep for each EEG in each age group	23
Table 2.4	P-values for the small-world measure between cross-correlation and wPLI functional connectivity	37
Table 3.1	Patient demographics and clinical data	53
Table 3.2	P-values for the comparison of connectivity strength between different FCN networks in individual subjects	61
Table 4.1	Interrater reliability for the classification of subject and event types	79
Table 4.2	Event agreement rate for subject and event types	79
Table 4.3	Rater accuracy for subject type	79
Table 4.4	Rater accuracies for subject labels in each cluster and subject group	83
Table 5.1	Feature categories with significantly more LGS or control events	110

Acknowledgements

My journey to this doctoral degree has never been done alone and was done through the help of numerous people. I would like to first thank my advisor Dr. Beth Lopour, who has always been there to me as a colleague, mentor, and friend. Working alongside her for the past six years has been an incredible part of my life and I cannot imagine being here without her diligence and thoughtfulness. I would also like to thank my committee members, Dr. Frithjof Kruggel and Dr. Ramesh Srinivasan for their valuable suggestions and support.

I would also like to thank the clinical and research collaborators throughout my work. Dr. Daniel Shrey's clinical work and communication with our research team has been invaluable to my studies. Dr. Shaun Hussain has also played a monumental role in our research with his clinical expertise and his feedback on our work. I look forward to continuing my work with these collaborators going forward.

Another valuable part of my doctoral degree is all my friends who have supported me in this process. I would first like to thank the current and former members of the Lopouratory, who have been exceptional role models, kind and compassionate lab mates, and lifelong friends. I would also like to thank all my friends who I have made along the way and those who have been with me throughout, your kindness and support has been invaluable, and I hope I can reciprocate these feelings to you all as well.

In addition, I would like to thank my parents and siblings back home for all their unwavering support throughout this process. My family has never hesitated to help me in times of need and words cannot express how lucky I am to have such incredible people by my side.

I would also like to thank Frontiers for permission to include Chapter Two of my dissertation, which was originally published in Frontiers in Network Physiology. I would also like to thank Frontiers for permission to include Chapter Three of my dissertation, which was originally published in Clinical Neurophysiology. Financial support was provided by the University of California, Irvine, the Children's Hospital of Orange County, NIH Grant ULTR001414, the Lennox-Gastaut Syndrome Foundation, and the John C. Hench Foundation.

Vita

Derek Kuan-Yu Hu

Education

2017	B.S. in Biomedical Engineering University of Utah
2020	M.S. in Biomedical Engineering University of California, Irvine
2023	Ph.D. in Biomedical Engineering University of California, Irvine

Publications

Hu, D.K.; Goetz, P.W.; To, P.D.; Garner, C.; Magers, A.L.; Skora, C.; Tran, N.; Yuen, T.; Hussain, S.A.; Shrey, D.W.; Lopour, B.A.; Evolution of Cortical Functional Networks in Healthy Infants. *Front. Netw. Physiol.* 2022, 2:893826

Goetz, P.W.; **Hu, D.K**.; To, P.D.; Garner, C.; Yuen, T.; Skora, C.; Shrey, D.W.; Lopour, B.A.; Scalp EEG markers of normal infant development using visual and computational approaches. *43rd Annual International Conference of the IEEE Engineering in Medicine & Biology Society (EMBC)*, 2021, 6528-6532

Smith, R.J.; **Hu, D.K**.; Shrey, D.W.; Rajaraman, R.; Hussain, S.A.; Lopour, B.A.; Computational characteristics of interictal EEG as objective markers of epileptic spasms. *Epilepsy Res.* 2021 176, 106704

Li, L.Y.; Schiffman, J.; **Hu, D.K**.; Lopour, B.A.; Martin, E.A. An Effortful Approach to Social Affiliation in Schizophrenia: Preliminary Evidence of Increased Theta and Alpha Connectivity during a Live Social Interaction. *Brain Sci.* 2021, 11, 1346.

Hu, D. K., Mower, A., Shrey, D. W., and Lopour, B. A. *Effect of interictal epileptiform discharges on EEG-based functional connectivity networks*. *Clin. Neurophysiol.* 2020, 131, 1087–1098

Hu, D. K., Li, L. Y., Lopour, B. A., and Martin, E. A. *Schizotypy dimensions are associated with altered resting state alpha connectivity*. *Int. J. Psychophysiol.* 2020. 155, 175–183.

ABSTRACT OF THE DISSERTATION

Identifying Quantitative Biomarkers in the Electroencephalogram for the Evaluation of Developmental and Epileptic Encephalopathies

By

Derek Kuan-Yu Hu

Doctor of Philosophy in Biomedical Engineering

University of California, Irvine, 2023

Associate Professor Beth A. Lopour, Chair

Developmental epileptic encephalopathies, such as infantile epileptic spasms syndrome (IESS) and Lennox-Gastaut Syndrome (LGS), are severe epilepsy syndromes that begin early in life. These syndromes are characterized by drug-resistant seizures, which can cause developmental delays and lifelong impairments. A favorable clinical outcome is reliant on a prompt diagnosis, but this is complicated by the variability in individual cases and the evolution of the epileptic encephalopathy into other refractory epilepsies. The electroencephalogram (EEG) is an indispensable tool to help evaluate these syndromes, as it provides a noninvasive measure of time-varying neural activity and can contain waveforms that are indicators of epilepsy. Furthermore, the application of computational techniques, such as functional connectivity and time-frequency analysis, can help identify and quantify the features of these waveforms, providing an objective measurement to guide clinical diagnosis and decision making.

Therefore, we aimed to develop quantitative EEG biomarkers for IESS and LGS for three purposes: (1) to improve diagnosis by providing clinicians a normalized baseline for healthy development, (2) to evaluate the functional network changes associated with pathological EEG waveforms, and (3) to discover EEG biomarkers that cannot be reliably

detected using visual review. First, we measured the changes in EEG functional connectivity networks during normal development in the first two years of life. We showed that an increase in network strength was typical during normal infant development, while the network structure remained stable. This work can serve as a baseline for future investigations in IESS, which is associated with altered functional connectivity networks. Second, we assessed the functional connectivity changes in patients with IESS during interictal epileptiform discharges (IEDs), a common epilepsy-associated waveform seen in EEG recordings. We found an increase in connectivity strength during IEDs that could be attributed to the underlying pathophysiology of the disease, rather than an increase in connectivity due to the broadly distributed waveform. Lastly, we developed a novel method for the discovery of EEG biomarkers using unsupervised analysis of the time-frequency decomposition. We applied this method to patients with LGS and confirmed that it could detect established EEG biomarkers of the disease. It also highlighted novel candidate biomarkers that occurred more frequently in patients with LGS than healthy controls but were not recognized as salient waveforms during visual review by epileptologists. A separate study confirmed the low interrater reliability for classifying EEG waveforms associated with LGS, which emphasizes the need for this type of objective, automated algorithm. In all, this work advanced computational EEG techniques, such as functional connectivity and time-frequency analysis, to complement standard visual review. In the long-term, incorporating such methods into clinical practice can lead to improvements in diagnosis and patient care which were previously not possible.

CHAPTER I

Introduction

1.1. Epilepsy

1.1.1 Definitions and overview of epilepsy

Epilepsy is one of the most common neurological diseases, affecting over 50 million people worldwide. The prevalence of active epilepsy cases varies by patient demographics, from 5-8 per 1000 cases in high income countries to 10 per 1000 in low-income countries, with higher reported rates in rural areas (Moshé et al. 2015). A person is defined as having epilepsy by the International League Against Epilepsy (ILAE) if they have any of the following conditions: (1) at least two unprovoked or reflex seizures occurring over 24 hours apart; (2) one unprovoked or reflex seizure with a high probability of further seizures after experiencing two unprovoked seizures within a 10 year window; or (3) a diagnosis of an epilepsy syndrome (Fisher et al. 2014). Patients with epilepsy typically experience seizures, which are transient occurrences of signs and/or symptoms due to abnormal, excessive, or synchronous neuronal activity in the brain. During these seizure episodes, the patient's cognitive ability and physical function are impeded (Fisher et al. 2014).

The impacts of epilepsy are devastating, resulting in higher rates of psychiatric and physical comorbidities, leading to premature deaths (Moshé et al. 2015). Psychiatric comorbidities can negatively affect disease prognosis and increase the risk of death. For example, a third of people with epilepsy are also diagnosed with anxiety or depressive disorder, twice as much as the general population (Rai et al. 2012; Keezer et al. 2016). Physical comorbidities such as migraine, heart disease, peptic ulcers, and arthritis are up to eight times more common in people with epilepsy compared to the general population (Keezer et al. 2016). Perhaps most concerning, the mortality rates of epilepsy are two to five times higher compared

to the general population in high-income countries and 37 times in low-income countries (Moshé et al. 2015). Specifically, cases of sudden death are 16-24 times greater in patients with epilepsy compared to the general population, with sudden unexpected death in epilepsy accounting for 38% of all deaths after 40 years in a follow-up study on childhood-onset epilepsy (Sillanpää and Shinnar 2010).

1.1.2 Overview of infantile and pediatric epilepsies

While the prevalence of epilepsy is lowest early in life, there are approximately 470,000 children in the US with epilepsy, with 50,000 new diagnoses every year (Fiest et al. 2017). Of these cases, epilepsy syndromes are particularly devastating in children, who are most susceptible to seizures in the first year of life.

Epilepsy syndromes that begin in childhood are divided into three main groups: (1) self-limited focal epilepsies; (2) genetic generalized epilepsy syndromes; and (3) developmental and or epileptic encephalopathies (Specchio et al. 2022). Self-limited focal epilepsies of childhood are often idiopathic and account for approximately 25% of all pediatric epilepsies. The symptoms associated with this type of epilepsy syndrome are often considered “benign”, with brief and mild seizure symptoms that cease by puberty. Genetic generalized epilepsy syndromes of childhood are associated with genetic etiologies that vary between patients. Lastly, developmental epileptic encephalopathies are diseases where the epileptic activity contributes to severe cognitive and developmental impairments (Scheffer et al. 2017).

1.1.3 Etiology in epileptic encephalopathies

Prior to clinical diagnosis, there is a need to consider the etiology of the epilepsy. Identifying the etiology of epilepsy can help determine what caused the seizures to begin and aid clinicians in providing a corresponding treatment (Berg et al. 2010). According to the ILAE classification of the epilepsies, etiologies are currently categorized into six different groups: structural, genetic, metabolic, infectious, immune, and unknown (Scheffer et al. 2017).

Structural abnormalities are typically one of the first etiologies tested in a patient, which is done using neuroimaging, such as magnetic resonance imaging (MRI). These can be caused by various conditions such as stroke, trauma, infection, and genetic malformations (Scheffer et al. 2017). In cases of developmental and epileptic encephalopathies, structural etiologies are the most common, as they were identified in over 70% of cases of infantile spasms (Shields 2006), most often using computed tomography (CT) and MRI (Specchio et al. 2022). Genetic etiologies are also common in young children. For example,30-50% of severe developmental and epileptic encephalopathies in infants were attributed to genetic abnormalities (McTague et al. 2016). Genetic mutations can be caused by environmental factors such as sleep deprivation, stress, and illness, all of which are more likely to occur with epilepsy (Scheffer et al. 2017). Genetic defects can also cause metabolic disorders which can disrupt the biochemical balance throughout the body such as porphyria, uremia, aminoacidopathies, or pyridoxine-dependent seizures (Scheffer et al. 2017). Infections are the most common cause of epilepsy worldwide and can be related to cases of neurocysticercosis, tuberculosis, HIV, cerebral malaria, subacute, cerebral toxoplasmosis, and congenital infections such as Zika virus (Scheffer et al. 2017). Immune etiologies can be connected to inflammation in the autoimmune-mediated central nervous system. Lastly, an unknown etiology means that the cause of epilepsy was unable to be determined based on available testing.

While certain etiologies are associated with a positive developmental outcome (Shields 2006), there are a large number of widely varying etiologies in cases of epileptic encephalopathies, which can complicate the diagnosis. In one case study on 207 infants with infantile spasms, an epileptic encephalopathy, 33% of subjects had an unknown etiology, 6% were not fully investigated, and 61% had proven etiologies such as hypoxic-ischemic encephalopathy, chromosomal malfunctions, brain malformations, stroke, and tuberous sclerosis (Osborne et al. 2010). In another study on Lennox-Gastaut Syndrome (LGS), another developmental epileptic encephalopathy, underlying pathologies consisted of encephalitis,

meningitis, tuberous sclerosis, brain malformations, birth injury, hypoxic-ischemia injury, and trauma (Khan and Al Baradie 2012).

1.2 Electroencephalography in pediatric epilepsies

In addition to tests to determine the etiology, scalp electroencephalogram (EEG) is a non-invasive diagnostic test that remains an essential tool for the evaluation of epilepsy. EEG provides clinicians with quantitative measurements of the neuronal activations in different regions of the brain with good temporal resolution. In cases of infantile epilepsies, clinicians are recommended to record 24 hours of overnight video EEG with a focus on capturing non-REM sleep, as there is a reduction of muscle, movement, and blinking artifacts during sleep (Pellock et al. 2010). One focus of EEG review is on identifying epileptiform waveforms, which are associated with pathological neural activity and have been correlated with disease severity (Staley et al. 2011).

1.2.1 Characteristics of normal infant EEG

Normal infant EEG is characterized by slow, high amplitude delta activity in the first year of life, with the introduction of a posterior dominant rhythm in the theta band at 6 months of age and in the alpha frequency band by 3 years of age (Britton et al. 2016). The EEG during sleep also contains non-epileptiform transient waveforms, which are distinguishable from background activity but are not associated with epilepsy. Some of these waveforms consist of sleep spindles, which typically emerge at 2 to 3 months of age, vertex sharp transients, which develop between 2 to 5 months of age, and K-complexes, which also develop between 2 to 5 months of age (Britton et al. 2016). These physiological waveforms can serve as biomarkers of health. For example, the presence and burden of fast sleep spindles have been associated with memory and processing speed in healthy individuals (Shinomiya et al. 1999a; Schiller et al. 2022).

1.2.2 Characteristics of pediatric epilepsy EEG

In comparison to the slow, consistent EEG background seen in healthy infants, the EEG in patients with epilepsy contains pathological waveforms that can vary between different epilepsy syndromes; we describe some commonly occurring characteristics here. Burst suppression is a common EEG waveform seen in epilepsy, which consists of intermittent bursts of fast, high amplitude activity that can occur during seizures (in ictal periods) or between seizures (interictal periods). Interictal spikes, also called interictal epileptiform discharges (IEDs), are another common epileptiform waveform in the EEG, defined by brief paroxysmal electrographic discharges that are observed between recurrent seizures. These events are commonly seen in EEG review, are associated with the pathogenesis of epilepsy, and serve as a potential biomarker of the disease (Staley et al. 2011). Another EEG characteristic is the focal and generalized slowing of the background, which provides evidence for diffuse or focal cerebral dysfunction and can also represent developmental slowing in children (Sela et al. 2002; Britton et al. 2016).

One challenge associated with visual EEG review is that normal, physiological EEG waveforms are frequently misinterpreted as pathological. This can lead to the overdiagnosis of epilepsy and unnecessarily prolonged treatment (Nayak and Anilkumar 2023). For example, benign epileptiform transients of sleep are low amplitude, brief, sharply contoured spikes that are often misclassified as epileptiform discharges (Sheng et al. 2023), while sleep spindles and k-complexes can have similar frequency behavior to paroxysmal fast activity.

1.3 Developmental epileptic encephalopathies

Of the pediatric epilepsy syndromes, developmental epileptic encephalopathies are the most severe, as they are generally unresponsive to standard therapies and can cause devastating neurocognitive effects during development (Khan and Al Baradie 2012; Scheffer et al. 2017). The primary goal of treatment for epileptic encephalopathies is the cessation of

seizures and the normalization of the EEG, which has been associated with the best cognitive and developmental outcomes (Lux et al. 2004; Pellock et al. 2010). One major challenge of treatment is the disease progression, as the epilepsy often evolves into different forms of epileptic encephalopathies with age. This evolution of the epilepsy can prolong both diagnosis and treatment, causing further developmental impairments in patients (Khan and Al Baradie 2012). Here, we discuss some of the main developmental epileptic encephalopathies seen in neonates, infants, and children.

1.3.1 Ohtahara syndrome

Ohtahara syndrome is the earliest form of the age-dependent neonatal epileptic encephalopathies, with an incidence of 1 in 50,000 to 100,000 births. Symptoms of Ohtahara syndrome appear within the first three months of life and are diagnosed based on the seizure patterns and EEG activity (Khan and Al Baradie 2012). Seizures are often manifested as tonic spasms but can also be tonic/clonic, clonic, myoclonic, atonic, absence, and partial seizures. Ohtahara syndrome is characterized in the EEG as burst suppressions occurring during wakefulness and sleep (Khan and Al Baradie 2012). This epileptic syndrome is associated with a high mortality rate, as half of all diagnosed patients are likely to die during infancy or childhood (Murakami et al. 1993; Fusco et al. 2001; Ohtahara and Yamatogi 2003).

The challenges in treating this disease are the intractable seizures, poor disease prognosis, and mortality rate. Seizure control is a slow and frustrating process, often requiring varied types and dosages of anticonvulsants such as vigabatrin, dilantin, zonegran, adrenocorticotropic hormone (ACTH), and prednisone. The disease progression is often associated with psychomotor delays that can worsen as the epilepsy evolves into other epileptic encephalopathies (Khan and Al Baradie 2012).

1.3.2 Infantile epileptic spasms syndrome

Infantile epileptic spasms syndrome (IESS) is a developmental epileptic encephalopathy that occurs during infancy from 3 to 12 months of age. The incidence of IESS is 2-5 per 10,000 newborns, which accounts for 10% of epilepsies that begin prior to the age of 36 months (Pavone et al. 2014; Symonds et al. 2021). It has a mortality rate estimated at 31% before the age of 36 months (Riikonen 2001). The diagnosis of IESS requires the presence of epileptic spasms, which are brief, abrupt, tonic contractions of axial muscles involving the extensor or flexor (Pavone et al. 2014; Zuberi et al. 2022). The onset of epileptic spasms can be subtle, with outward symptoms consisting of innocuous activities such as yawning, grasping, facial grimacing, isolated eye movements, blinking, and transient focal motor activities (Pellock et al. 2010). For example, some spasms can be as subtle as a small head nod (Hrachovy and Frost 2003; Pellock et al. 2010). Detecting epileptic spasms is challenging due to the variability in frequency, duration, and movement associated with the spasms.

IESS is associated with abnormal EEG, and developmental regression, although these are not mandatory for diagnosis (Zuberi et al. 2022). In IESS, the EEG consists of fast beta activity superimposed on diffuse, high-amplitude slow waves, contrasting the low-amplitude slow waves seen in healthy subjects. Hypsarrhythmia occurs in the EEG during interictal periods of sleep and is characterized as multi-focal, asynchronous, independent epileptiform discharges and sharp waves contained within a disorganized background with large amplitude slow waves (Stamps et al. 1959; Pellock et al. 2010; Khan and Al Baradie 2012). While hypsarrhythmia is not present in all subjects (Bower and Jeavons 1959; Stamps et al. 1959; Romero Milà et al. 2022), it is a unique and defining feature of IESS. Hypsarrhythmia has also been shown to be a prognostic parameter in IESS, where a prolonged hypsarrhythmia duration is associated with an increased risk of developmental delay (Kivity et al. 2004; Primec et al. 2006). Other EEG biomarkers of IESS may also be good indicators of seizure control and outcome, as continued IEDs predicted the relapse of IESS after ACTH treatment (Hayashi et al. 2016). IESS subjects with no hypsarrhythmia and no epileptiform EEG activity after treatment

were also reported to have a significantly lower seizure relapse rate than those with these features (Yamada et al. 2014). Despite the utility of these EEG patterns, the determination of hypsarrhythmia has poor interrater reliability (Hussain et al. 2015; Mytinger et al. 2015). This highlights the need for a quantifiable, reliable, and unbiased method of interictal EEG analysis for IESS.

In cases of IESS, minimizing the time from spasm onset to treatment is imperative to developmental success (Primec et al. 2006). Of the current initial treatment methods for IESS, ACTH and vigabatrin are the two anti-seizure medications with the most favorable outcomes (Pellock et al. 2010; Knupp et al. 2016). ACTH has been shown to have better neurodevelopmental outcomes than vigabatrin in children with IESS (Kivity et al. 2004; Pellock et al. 2010; Go et al. 2012; Knupp et al. 2016). There are mixed findings on the optimal dosage and duration of ACTH treatment, where favorable outcomes have been reported for both low dosages (Go et al. 2012) and high dosages of (Kivity et al. 2004). The use of corticosteroids, such as prednisolone, have also been used in initial therapy and been shown to improve developmental outcomes in refractory patients (Lux et al. 2004; Mohamed et al. 2011; Go et al. 2012; Khan and Al Baradie 2012). Other agents that are efficacious include valproate, levetiracetam, topiramate, zonisamide, lamotrigine, and benzodiazepines (Khan and Al Baradie 2012). In most studies, it was found that patients who were treated quickly after the onset of spasms had a greater chance of treatment success, while patients with prolonged time to treatment onset often had poor developmental outcomes (Kivity et al. 2004; Primec et al. 2006; Riikonen 2010; Yamada et al. 2014).

One challenge in treating IESS is the broad range of potential causes of this encephalopathy, including cerebral malformations, infection, hemorrhage, hypoxic ischemic injury, metabolic disorders, and genetic conditions (Khan and Al Baradie 2012). Delays in diagnosis and treatment can often lead to poor developmental outcomes and can result in the

evolution to lifelong epilepsies, with 50-70% of IESS cases evolving into other seizure types and 20-50% of drug resistant IESS cases evolving into LGS (Pavone et al. 2014).

1.3.3 Lennox-Gastaut Syndrome

Lennox-Gastaut Syndrome is a severe developmental epileptic encephalopathy that develops during childhood, with onset between 18 months to 8 years of age (Arzimanoglou et al. 2009; Khan and Al Baradie 2012; Specchio et al. 2022). Cases of LGS represent 1-4% of childhood epilepsies, with most cases of LGS having a history of infantile epilepsy syndromes and 30% of cases evolving from IESS (Cross et al. 2017). LGS is characterized by (1) multiple types of drug-resistant seizures with onset prior to 18 years (one seizure must be tonic); (2) cognitive and behavioral impairment; and (3) diffuse slow spike-and-wave and generalized paroxysmal fast activity on EEG (Specchio et al. 2022).

One major challenge in LGS diagnosis is fulfilling all the clinical and EEG requirements. Currently, the diagnosis of LGS requires the occurrence of tonic seizures, other seizure types, EEG abnormalities, and cognitive impairment (Specchio et al. 2022). Collectively, these indicators each take time to surface, which results in only 0.6% of all LGS cases diagnosed at initial seizure onset (Specchio et al. 2022). Tonic seizures consist of an increase in axial and limb muscle contraction that lasts from 3 seconds to 2 minutes, while the second seizure type may include any other seizure type such as atypical absence, atonic, myoclonic, focal impaired awareness, generalized tonic-clonic, or epileptic spasms (Specchio et al. 2022). LGS diagnosis also requires the presence of a spike-wave pattern in the EEG, which is a key biomarker of the progression of LGS (Khan and Al Baradie 2012). The delayed treatment of LGS causes further intellectual and psychological deficits over the course of childhood, with 20-60% already having developmental delay at the onset of LGS and 90% of patients having some sort of mental impairment that persists into adulthood (Gallop et al. 2009).

LGS diagnosis requires the use of sleep EEG to identify generalized 2-6 Hz spike-waves and other abnormalities. Spike-waves are the most prominent feature in LGS interictal sleep EEG; they appear as a spike less than 70 milliseconds long or a sharp wave of 70-200 milliseconds duration, followed by a negative high-voltage slow wave (350-400 ms), with this pattern repeating at a frequency less than 2.5 Hz (Specchio et al. 2022). Other EEG abnormalities typically take the form of burst suppressions, short bursts of high amplitude activity. For example, generalized paroxysmal fast activity (GPFA) in the EEG is characterized as bursts of diffuse or bilateral fast activity lasting less than a few seconds and exceeding 10 Hz (Specchio et al. 2022). While GPFAs are not mandatory for LGS diagnosis, this type of waveform is mostly unique to LGS subjects, indicative of LGS activity, and occurs during interictal sleep. One challenge in identifying these EEG waveforms in LGS is the change in EEG with age and disease evolution, as diffuse multi-focal slow spike-waves tend to become more frontal over time (Rijckevorsel 2008). Another challenge is the inconsistent occurrence and rater agreement of these waveforms, as slow spike-waves and GPFA do not regularly occur in EEG and also have low interrater reliability and agreement (Jing et al. 2020). Because the features of LGS can evolve slowly over time, proactively monitoring EEG abnormalities and assessing cognitive performance and behavior are recommended as indicators of disease progression.

Due to the intractable seizures and complexity of LGS, the focus of treatment is often on improving the patient's quality of life through seizure control, as opposed to total seizure freedom (Cross et al. 2017). Initial treatment options typically include the use of various anti-seizure medications such as valproic acid and benzodiazepines such as clobazam, clonazepam, clorazepate, nitrazepam, vigabatrin, zonisamide, lamotrigine, topiramate and rufinamide, which have been proven effective by double-blind placebo-controlled studies (Khan and Al Baradie 2012). Treatments vary between patients, as each LGS patient undergoes multiple and different seizure types and can respond differently to each combination of medications (Rijckevorsel 2008). Alternative approaches, such as the ketogenic diet, may be

useful in patients with LGS refractory to medical treatment. Surgical options for LGS include corpus callosotomy, vagus nerve stimulation, and focal cortical resection (Rijckevorsel 2008; Arzimanoglou et al. 2009; Khan and Al Baradie 2012).

1.4 Computational EEG analysis in epileptic encephalopathies

While the identification of abnormal EEG patterns is crucial for the clinical diagnosis of epileptic encephalopathies, there are characteristics of the EEG that cannot be assessed by visual review of the data. Several computational analysis techniques have been applied to EEG data to create quantitative diagnostic biomarkers that can differentiate healthy controls from individuals with epileptic encephalopathies. For instance, EEG amplitude and spectral power in children with IS are significantly higher in all frequency bands compared to healthy controls in both wakefulness and sleep (Smith et al. 2018, 2021b; Romero Milà et al. 2022). Similarly, entropy has been used to differentiate infants with IS from healthy controls in the delta and theta bands during wakefulness and sleep (Smith et al. 2021b; Romero Milà et al. 2022). Computational techniques have also identified potential quantitative biomarkers of treatment response, as changes in long-range temporal connections mirrored the patient's post-treatment EEG for hypsarrhythmia (Smith et al. 2017). Here, we discuss additional computational techniques for analysis of the EEG in individuals with epileptic encephalopathies.

1.4.1 Functional connectivity

Functional connectivity networks (FCNs) are a brain mapping technique based on the statistical interdependencies of spatially distinct time-varying neural signals. FCNs can be derived from various continuous physiological signals, such as EEG and functional magnetic resonance imaging, where they represent the regional interactions on a macroscopic level (Matos et al. 2022). Rather than measuring the direct anatomical relationships between these brain regions, functional networks are inferred and depend on the choice of the coupling

measure. Based on the measure, the network is either binary or weighted with directed or bidirectional connections. FCNs can be summarized by a matrix, where each element corresponds to a connection pair between two different brain regions.

To summarize the FCN as a quantitative biomarker, graph theory measures are often used to reduce the FCN to a few characteristic values. Graph theory measures can quantify features, such as the global, regional, and topological characteristics of the network (Rubinov and Sporns 2010; Matos et al. 2022). Global measures, such as the connectivity strength, can be used to represent all connections in the FCN as a single value. Regional measures, such as the degree, correspond to the connectivity characteristics in individual brain regions. Topological features, such as the clustering coefficient and path length, evaluate the network structure by measuring properties like the number of interconnected groups of connected triplets, or the ability to efficiently transfer information between different brain regions. The location of significant functional connections can also be assessed. For example, asymmetry measures the proportion of connections in the anterior/posterior and left/right hemispheres (Matos et al. 2022). Lastly, a given connectivity network can be compared to preexisting network models, such as regular, random, and small-world networks, which each function differently and exhibit different features based on how the regions are connected (Kramer and Cash 2012).

FCNs are extensively used in epilepsy research, as epilepsy is considered a network disorder that exhibits pathological changes before and during seizures (Kramer and Cash 2012). During a seizure, the abnormal electrical activity can spread from a central focus outward while recruiting other pathological and normal brain tissue in a cascade of activity. This phenomenon can be analyzed using coupling analysis and represented as a functional network (Kramer and Cash 2012). We can then compare these changes to healthy FCNs, which have been found to have a core functional network organization that is topologically stable over multiple hours across different states of consciousness (Chu-Shore et al. 2012). Healthy

networks have also been found to have a stereotyped sequence over normal cortical development across healthy children (Chu et al. 2014).

Collectively, EEG-based FCNs have potential as a clinical biomarker of disease severity, which can potentially predict long-term outcome. This is seen in interictal EEG studies, which report network alterations due to focal epilepsies compared to healthy controls (van Diessen et al. 2016). Functional connectivity has also been used to explain the mechanisms of EEG waveforms such as hypsarrhythmia in IESS subjects, where multi-focal independent spikes were correlated to blood-oxygen-level-dependent imaging oscillations on the cerebral cortex (Siniatchkin et al. 2007). FCNs can also serve as a potential biomarker of treatment response in IESS, as pre-treatment subjects had stronger FCNs than healthy controls, but the IESS networks more closely resembled those of the control subjects following successful treatment (Shrey et al. 2018a).

Despite the promising utility of FCNs for clinical purposes, there are several barriers to their implementation. It is difficult to differentiate physiological versus pathological changes in the network. This is particularly challenging in cases of infantile epileptic encephalopathies, as infants are developing and undergoing major structural changes at the same time as exhibiting pathological activity. There is no consensus on the typical developmental changes in FCNs from the neonatal period to late infancy (Vértes and Bullmore 2015), which can hinder the use of FCNs as a biomarker for patients in this age range. Another challenge is the stability and consistency of FCNs in evaluating epileptic encephalopathies, particularly during broadly distributed waveforms such as IEDs. While prior studies have shown that interictal EEG functional networks are stronger in IESS compared to healthy infants (Smith et al. 2021b) and the alteration of FCNs may reflect pathological activity (Ponten et al. 2009; Horstmann et al. 2010; Adebimpe et al. 2015; Coito et al. 2016), it is unknown whether this connectivity change is always present or is temporarily altered during the epileptiform discharge. Answering this

question could improve the robustness of FCNs as a quantitative biomarker for the evaluation of epileptic encephalopathies.

1.4.2 Time-frequency analysis

Time-frequency analysis is a technique that decomposes a signal into both the time and frequency domains simultaneously. This technique is particularly useful in EEG, where many key waveforms and events are characterized based on the neuronal oscillations of the signal. Rather than assessing the EEG as a function of amplitude over time, time-frequency analysis can be implemented to assess the power of the signal in different frequency bands and provide additional information about the frequency variations over time.

Many automated algorithms have been developed to analyze EEG waveforms based on the time-frequency characteristics. One benefit to using time-frequency analysis over the timeseries is the ability to characterize both spectral and temporal dynamics of the signal. For example, IEDs are often associated with an oscillation at a specific frequency. Time-frequency analysis can characterize what is happening before, during, and after an IED in both time and frequency, which gives us additional information on the various features of the signal (Jabran et al. 2020).

Another benefit of this technique is the ability to create automated detectors for specific time-frequency features, which can be used as an alternative or complement to visual EEG review. Interictal spike detectors can detect spikes based on various features derived from the time-frequency analysis (Gaspard et al. 2014) or based on a template calculated using the average of multiple spikes (Karoly et al. 2016). Time-frequency analysis has also been implemented to create automated detectors for interictal spikes in refractory epilepsies (Jacobs et al. 2011; Jabran et al. 2020), sleep spindles (Ahmed et al. 2009), and GPFAs in patients with LGS (Omidvarnia et al. 2021). These detectors can apply detection criteria consistently across patients and centers, which can avoid biases from individual reviewers (Jing et al. 2020).

Time-frequency analysis can also help us visualize features of the EEG that cannot be seen during standard clinical review. For instance, EEG waveforms called high-frequency oscillations (HFOs) are defined as transient electrographic events distinct from the background that consist of four or more oscillations at a frequency >80 Hz (Jacobs et al. 2011). While HFOs were first described and analyzed in microelectrodes and animal models, HFOs have now been detected in scalp EEG and have been correlated with the seizure onset zone and underlying mechanisms of epilepsy (Jacobs and Zijlmans 2020). Although HFOs are barely visible when the EEG is viewed with standard review settings due to their small amplitude and short duration, time-frequency analysis has been used to automatically detect HFOs and characterize the features of them (Krikid et al. 2022).

One challenge of implementing time-frequency analysis in epileptic encephalopathies is the reliance on clinical review for validation, which is often treated as the gold standard despite having low interrater agreement (Reus et al. 2022). Because of this, detectors often rely on empirical definitions of EEG waveforms, which are derived from clinical descriptions of the data. This, in turn, means that there is no strong basis for the further development and improvement of automated detectors, as detected events are compared to manual markings as a "ground truth", despite having imprecise definitions and high variance between reviewers.

1.5 Scope of the dissertation

In this doctoral dissertation, we develop and validate various computational techniques to study EEG and the physiological and pathological waveforms contained therein. This work aims to provide a computational approach to complement clinical interpretation of EEG data and to discover quantitative biomarkers to aid in the diagnosis of epilepsy and evaluation of the disease progression.

In Chapter 2, we use FCNs to analyze the evolution of cortical network organization in the EEG of 240 healthy infants from zero to two years of age (Hu et al. 2022). In this cohort, we

find no differences in network structure, but there is an increase in network strength during the first year of normal development. This work serves as an age-matched baseline for future investigations in infantile neurological diseases, where we can assess the changes in network strength and structure as a potential indicator of patient health.

One confounding factor when analyzing FCNs in epilepsy is the irregular occurrence of transient waveforms such as IEDs, which can impact the measurement of the network. In Chapter 3, we assess the pathological network changes in patients with IESS during IEDs and compare them to healthy controls with simulated IED waveforms (Hu et al. 2020a). Here, we show that the increase in connectivity strength during IEDs is attributed to the underlying pathophysiology of IESS, rather than the presence of the IED waveform, suggesting the activation of some pathological network mechanism during the IED. We also show that the network structure remains unchanged by the addition of transient IEDs, indicating the robustness of FCNs as a quantitative biomarker.

Lastly, we develop a novel unsupervised time-frequency image analysis method to automatically detect EEG events that are candidate biomarkers for epilepsy. In Chapter 4, we use our unsupervised time-frequency analysis to identify 1,350 EEG events in patients with LGS, which are subsequently visually classified by three pediatric epileptologists. We show that events with rater agreement consist of EEG waveforms commonly seen in LGS, such as IEDs and GPFAs. This validates the automated detection method. Interestingly, most events with disagreement are not due to misidentification, but rather clinicians disagreeing on the threshold for choosing each label. In Chapter 5, we apply clustering to the EEG events, and we demonstrate that this time-frequency approach can objectively identify previously known biomarkers of LGS, such as GPFAs, while also discovering novel candidate biomarkers that were not apparent during visual review.

Overall, this work aims to utilize computational analysis of scalp EEG recordings to aid clinicians in the initial diagnosis of epilepsy and the early evaluation of medication, one of the

most critical times of treatment (Camfield et al. 2011; Piña-Garza et al. 2017; Berg, Anne; Levy and Testa 2018). These computational techniques can provide quantifiable metrics to complement clinical EEG review and provide new biomarkers of patient health, thus enabling more accurate diagnosis and faster treatment evaluation of developmental epileptic encephalopathies.

CHAPTER II

Evolution of Cortical Functional Networks in Healthy Infants

2.1 Introduction

The development of the infant brain (0-2 years old) is characterized by the evolution of neuronal oscillations in various frequency bands, which can be measured non-invasively using electroencephalography (EEG). Such cortical rhythms can be mapped as functional connectivity networks (FCNs) based on the statistical relationships between these neuronal oscillations across spatially distinct regions. Prior studies have reported strong EEG functional connections predominantly in the frontal and parieto-occipital regions in newborn infants (Omidvarnia et al. 2014; Tóth et al. 2017), with a subsequent shift in network topology from a randomized structure towards a more efficient and organized network during infancy (Xie et al. 2019) and childhood (Boersma et al. 2011). These FCNs also have properties that are specific to certain EEG frequency bands. Newborn infants exhibit clustered, fronto-parietal connections in the theta and alpha bands (Tóth et al. 2017). From infancy to age 18, healthy subjects show an increase in broadband connectivity strength, decrease in high gamma connectivity strength, decreases in delta and theta band clustering, and increase in gamma band clustering (Chu et al. 2014). Such frequency band-specific FCNs can indicate different neural mechanisms, as delta and theta networks integrate long-range neuronal assemblies, while gamma and higher frequencies reflect more localized networks (Fries 2005, 2015; Buzsáki and Watson 2012; Bastos and Schoffelen 2016).

While studies have examined EEG FCNs around the time of birth (Omidvarnia et al. 2014; Tokariev et al. 2016; Tóth et al. 2017), within a span of several months during infancy (Xie et al. 2019), or during early childhood (Boersma et al. 2011; Bathelt et al. 2013), there has yet to be a study that focuses exclusively on the evolution of connectivity during the first two years of

life. Chu et al. (2014) analyzed EEG connectivity in this age range, but primarily focused on developmental changes across a wider age range of 0-18 years. Moreover, no consensus has been reached on the typical developmental changes in FCNs. Small-world topological features have been reported to disappear around 10 months of age (Xie et al. 2019), despite reports of small world networks in older children (Boersma et al. 2011; Bathelt et al. 2013). Graph theory (GT) measures in FCNs such as path length have also produced mixed results, with both decreases (Miskovic et al. 2015) and increases (Boersma et al. 2011) in alpha band path length with age during childhood. Increases in clustering coefficient and path length from childhood to adolescence have been reported (Smit et al. 2012), while other studies found no correlations between subject age and GT measures in childhood (Bathelt et al. 2013). These differing results may be attributed to several factors, including the variance across EEG datasets and the choice of functional connectivity technique, e.g. linear versus nonlinear, bivariate versus multivariate, and phase-based versus amplitude-based measures (Olejarczyk et al. 2017; Siems and Siegel 2020).

Therefore, the goal of this study was to characterize the changes in functional connectivity networks over the course of normal infant development using two complementary computational methods. We measured EEG FCNs in a large cohort of healthy infants (n=240), ranging from 0-24 months old. For each subject, networks were derived separately for wakefulness and sleep in the delta, theta, alpha, beta, and broadband frequency bands. Two complementary methods were used to calculate the FCNs: cross-correlation and weighted phase lag index. Differences between age groups were quantified using connectivity strength and GT measures. By focusing specifically on healthy infants and directly comparing results across various connectivity techniques, this work further elucidates the evolution of FCNs during normal brain ontogeny and serves as a baseline for the study of early life neurological diseases.

2.2 Methods

2.2.1 Subject information and electroencephalography recordings

Approval for this retrospective observational study was obtained from the Institutional Review Board of the Children's Hospital of Orange County (CHOC), with the requirement for informed consent waived. A total of 240 subjects aged 0–24 months were retrospectively identified from the clinical record at CHOC, with visits between 1 January 2012 and 1 January 2019. Subjects were included if they had 1) no known neurological disorders, 2) routine EEG studies that were interpreted as normal by a board certified pediatric epileptologist (DS), 3) no use of neuroactive medications, and 4) no premature birth (gestational age >38 weeks). Subjects were divided into eight age groups (n = 30 for each group) in 3-month intervals (e.g., 0–3 months, 3–6 months, etc.) based on the subject's age at the time of EEG recording. Three subjects in the 0–3-months age group were excluded from the analysis due to excessive artifactual noise across multiple channels. The demographics of the study population are summarized in Table 2.1.

Table 2.1 Demographics for healthy participants

Group	**Age in mos.** ***M*** **(SD)**	**Female** ***n*** **(%)**	**Subjects** ***n***	**Wakefulness** ***n*** **(%)**	**Sleep** ***n*** **(%)**
0-3 m.	1.54 (0.94)	12 (40.00)	30	24 (80.00)	22 (73.33)
3-6 m.	4.67 (0.93)	16 (53.33)	30	29 (96.67)	26 (86.67)
6-9 m.	7.41 (0.83)	19 (63.33)	30	30 (100.00)	29 (96.67)
9-12 m.	10.24 (0.74)	19 (63.33)	30	29 (96.67)	24 (80.00)
12-15 m.	13.57 (0.87)	17 (56.67)	30	29 (96.67)	23 (76.67)
15-18 m.	16.33 (0.97)	15 (50.00)	30	28 (93.33)	27 (90.00)
18-21 m.	19.01 (0.73)	17 (56.67)	30	29 (96.67)	22 (73.33)

21-24 m.	22.54 (0.92)	16 (53.33)	30	29 (96.67)	24 (80.00)

2.2.2 Electroencephalography acquisition and preprocessing

EEG data were recorded with a Nihon Kohden EEG acquisition system, with nineteen scalp electrodes (Fp1, Fp2, F3, F4, C3, C4, P3, P4, O1, O2, F7, F8, T3, T4, T5, T6, Fz, Cz, and Pz) placed according to the international 10–20 system, at a sampling rate of 200 Hz. One subject's EEG was recorded at 500 Hz and downsampled prior to analysis. All EEG studies lasted from 20 to 70 min and contained a mixture of wakefulness and sleep. Manual EEG sleep staging was performed for all subjects by registered polysomnographic technologists (CG, AM, and NT) in accordance with the American Academy of Sleep Medicine (AASM) guidelines. EEG studies for subjects younger than 3 months were scored as wake, active sleep, or quiet sleep according to standard criteria. For all subjects older than 3 months, EEG epochs were categorized as wake (W), rapid eye movement (REM), non-REM stage 1 (N1), non-REM stage 2 (N2), and non-REM stage 3 (N3) sleep. However, only wake and N2 sleep data were analyzed, as most subjects' studies contained a sufficient quantity of these stages for the connectivity analysis. N2 sleep was also chosen due to its high inter-scorer reliability during sleep staging and because of the stability of the FCN during this sleep stage in individual subjects over time (Chu-Shore et al. 2012; Rosenberg and Van Hout 2013).

Time periods in the EEG containing artifact were identified using an automatic extreme value detection algorithm similar to prior studies (Durka et al. 2003; Moretti et al. 2003; Smith et al. 2021a). To identify artifacts, the raw data were filtered using a broadband bandpass filter (1.5–40 Hz Butterworth filter), re-referenced to the common average, and normalized in each channel to have zero mean and unit variance. In each channel, artifacts were identified as periods where the absolute value of the voltage exceeded a threshold of 7.5 standard deviations above the mean value, with a buffer of 0.9 s added to the beginning and end of each period.

Impedance checks and photic stimulation were visually identified in the EEG and were also marked as artifact. For all subjects, the mean duration of EEG recordings and time in wakefulness and quiet/N2 sleep is provided in Table 2.2, and the percentage of artifactual data in the EEG recordings is given in Table 2.3.

For the connectivity analysis, the raw data were re-referenced to the common average and filters were applied for each connectivity technique as described in Chapter 2.2.3. Time periods containing an artifact in at least one channel were then removed from all channels. For each sleep stage, clean EEG segments with no detected artifact were then separated into two-s epochs for FCN analysis. All electronic data were deidentified and analyzed offline using custom MATLAB (Mathworks) scripts.

Table 2.2 *Mean EEG, artifact, wake, and sleep duration for each age group. The mean EEG duration also consists of N1 and N3 sleep*

Group	**Mean EEG duration, sec (std), [range]**	**Mean artifact duration, sec [std, range]**	**Mean wakefulness duration, sec [std, range]**	**Mean quiet/N2 sleep duration, sec [std, range]**
0-3 m.	2530 (814) [1740-3900]	1105 (500) [413-2291]	480 (314) [109-1255]	562 (425) [0-1557]
3-6 m.	2110 (355) [1560-3060]	485 (204) [92-969]	780 (429) [202-1757]	534 (312) [0-1183]
6-9 m.	2136 (384) [1320-3060]	396 (134) [227-877]	689 (389) [211-1606]	739 (303) [143-1525]
9-12 m.	2204 (459) [1200-3360]	502 (207) [224-1027]	877 (448) [0-1928]	597 (355) [0-1178]
12-15 m.	2194 (291) [1807-2940]	501 (168) [228-927]	844 (425) [212-1853]	692 (440) [0-1451]
15-18 m.	2318 (370)	566 (309)	873 (510)	614 (309)

	[1800-3120]	[266-1980]	[123-2051]	[0-1410]
18-21 m.	2254 (397)	532 (234)	948 (531)	522 (355)
	[1800-3420]	[281-1474]	[188-2024]	[0-951]
21-24 m.	2288 (342)	521 (192)	928 (497)	570 (343)
	[1800-3420]	[258-1114]	[199-2002]	[0-1236]

Table 2.3 Mean percentage of artifact, wake, and N2 sleep for each EEG in each age group. The mean percentage of artifact across all subjects was 25%.

Group	Artifact % (std)	Wake % (std)	Quiet/N2 sleep %(std)
0-3 m.	43.5 (12.9)	18.8 (10.1)	22.6 (16.9)
3-6 m.	22.8 (7.7)	36.6 (19.0)	25.9 (15.9)
6-9 m.	18.9 (6.2)	30.8 (12.7)	35.1 (14.0)
9-12 m.	23.0 (8.4)	39.2 (18.3)	27.7 (16.8)
12-15 m.	22.9 (7.3)	38.3 (18.8)	31.7 (19.9)
15-18 m.	25.0 (15.9)	36.0 (16.7)	27.3 (13.6)
18-21 m.	23.4 (7.6)	41.0 (20.8)	24.2 (17.4)
21-24 m.	22.6 (6.8)	39.8 (20.2)	25.6 (17.2)

2.2.3 Functional connectivity network calculations

Two functional connectivity metrics were used in this study: cross-correlation (CC) and weighted phase lag index (wPLI). CC is a linear, time domain measure applied to broadband data, and wPLI is a phase-based measure applied to individual frequency bands that is sensitive to both linear and nonlinear interactions (Vinck et al. 2011; He et al. 2019). For CC, broadband EEG data were analyzed after zero-phase shift digital filtering from 0.5 to 55 Hz; wPLI was analyzed in the delta (2–4 Hz), theta (4.5–7.5 Hz), alpha (8–12.5 Hz), and beta (13–30 Hz) frequency bands. For the FCN calculation of each subject, 120 two-s epochs of clean

EEG data were randomly selected within each brain state (wakefulness and quiet/N2 sleep), and CC and wPLI were calculated independently for each brain state. The number of epochs was chosen based on an analysis of the stability of the connectivity technique; if a subject had insufficient clean data for a particular brain state, their data were excluded from analysis. The number of subjects included in the FCN analysis for wakefulness and quiet/N2 sleep is shown in Table 2.1.

2.2.3.1 Cross-correlation

Cross-correlation is a linear measure of connectivity based on the maximal cross-correlation between two EEG channels at nonzero lags (Kramer et al. 2009; Chu-Shore et al. 2012). This technique has been previously applied to both epileptic and healthy infant EEG data (Shrey et al. 2018b; Hu et al. 2020b; Smith et al. 2021a). For each subject and brain state with sufficient data, we began the connectivity analysis by subdividing the 120 two-s epochs into 240 one-s epochs. The choice of epoch length for CC was based on prior work demonstrating the stability of this measurement for as few as ~100 epochs of one-s duration (Chu-Shore et al., 2012; Shrey et al., 2018; Smith et al., 2021). The connectivity for each one-s epoch was calculated as the maximal absolute value of the cross-correlation with a maximum lag time of ±200 ms. Additional steps accounted for the influence of volume conduction and the autocorrelation of each signal, and permutation resampling was used for significance testing; please see Hu et al. (2020) for details. The CC connectivity for each subject was reported as an adjacency matrix where each element represented the percentage of epochs with significant connectivity values, with values ranging from zero to one for each pair of channels.

2.2.3.2 Weighted phase lag index

The wPLI is a measure of functional connectivity based on the phase synchronization between channel pairs. For channels x and y, the wPLI in a data segment with n time points is defined as:

$$\mathrm{wPLI}_{xy} = \frac{n^{-1}\sum_{t=1}^{n}\left|imag\left(S_{xyt}\right)\right|sgn(imag\left(S_{xyt}\right))}{n^{-1}\sum_{t=1}^{n}\left|imag(S_{xyt})\right|} \qquad (2.1)$$

The wPLI measures the average sign of the imaginary component of the cross spectrum S_{xy} and weights the value by the magnitude of the imaginary component to reduce the effect of cross-spectral values near zero and pi. The wPLI was chosen because it is more sensitive to phase synchronization than PLI, while reducing the influence of both noise sources and volume conduction (Vinck et al. 2011).

For each subject, all 120 two-s epochs of clean EEG data were used to calculate the wPLI FCN, as this amount of data ensures the stability of the measure (Haartsen et al. 2020). In each frequency band, the instantaneous phase was obtained via the Hilbert transform of the filtered EEG signal for each channel. A connectivity matrix was then calculated for each epoch using Eq. 1 for each channel pair. The significance of each epoch was assessed by generating a null distribution of wPLI values for each pair of EEG channels under the assumption of no temporal relationship between the signals. This was done by calculating the wPLI of two randomly selected epochs for 1,000 iterations. The measured wPLI value for each channel pair in an epoch was considered significant if it exceeded the 95th percentile of the null distribution. Significant connections were assigned a value of one, while non-significant connections were assigned a value of zero. The FCN for each subject was then calculated by averaging the binary matrices over all epochs. Therefore, analogous to the CC measure, each element in the adjacency matrix represents the percentage of epochs with significant connectivity values.

2.2.4 Graph theory metrics

Graph theory has been successfully used to analyze networks in a broad range of human neuroscience studies (Sporns 2018), with applications to data modalities ranging from structural and functional brain measurements (Hallquist and Hillary 2018; Bellantuono et al. 2021) to genetics (Monaco et al. 2019). Here, differences in FCNs between groups were quantified using four different GT measures: 1) network strength, 2) normalized global clustering coefficient (nGCC), 3) normalized characteristic path length (nCPL), and 4) small-world measure (SW). These measures were found to be relevant in prior studies of neonatal (Omidvarnia et al. 2014; Tóth et al. 2017), infantile (Fan et al. 2011; Gao et al. 2011; Xie et al. 2019), and childhood development (Boersma et al. 2011; Bathelt et al. 2013). All metrics were calculated using functions from the Brain Connectivity Toolbox (Rubinov and Sporns 2010) and custom MATLAB (Mathworks) scripts.

The network strength was defined as the mean of the strongest ten percent of connections and was calculated for each subject, connectivity technique, and brain state (Garrison et al. 2015; Smith et al. 2021a). Topological changes in the network structure were quantified using GCC and CPL. A network with a high GCC indicates the presence of strongly connected electrode triplets, and a low CPL value indicates that the network can efficiently transfer information between nodes (Watts and Strogatz 1998). To reduce the effects of weak connections, the weighted connectivity matrices were thresholded at an edge density of 0.25. This threshold was chosen by testing edge densities from 0.05 to 0.80 (Figures 2.1-2.5). We found that edge densities under 0.1 had high variability and often resulted in unconnected graphs, while edge densities over 0.4 could produce fully connected graphs with nGCC and SW values near one. An edge density of 0.25 was chosen here, as it exhibited low variability between subjects while forming a connected graph. In addition, prior studies found that edge densities of 0.1–0.4 were appropriate for GCC, CPL, and SW measures (Mehraram et al. 2020; Carpels et al. 2021). The thresholded weighted matrix was then normalized by dividing each element by the maximum connectivity value to avoid the influence of network strength on the

GT measures (Onnela et al. 2005; Antoniou and Tsompa 2008; Mehraram et al. 2020; Carpels et al. 2021). This normalized matrix was used to calculate GCC, and it was also converted into a distance matrix to calculate CPL. The GCC and CPL measures were then reported as normalized values relative to 100 surrogate networks generated using an Erdős–Rényi random graph:

$$nGCC = \frac{GCC}{GCC_{rand}} \qquad (2.2)$$

$$nCPL = \frac{CPL}{CPL_{rand}} \qquad (2.3)$$

An nGCC value greater than one suggests that the network is more clustered than a randomized network, while an nCPL greater than one suggests that the network is configured to transfer information less efficiently than a randomized network.

The small-world characteristics of the FCNs were measured as the ratio of the normalized GCC and normalized CPL measures (Humphries and Gurney 2008):

$$SW = \frac{nGCC}{nCPL} \qquad (2.4)$$

Small-world networks are typically characterized by high values of GCC and low values of CPL. Compared to a randomized network with low clustering and short path length, a small-world FCN should then have an SW > 1.

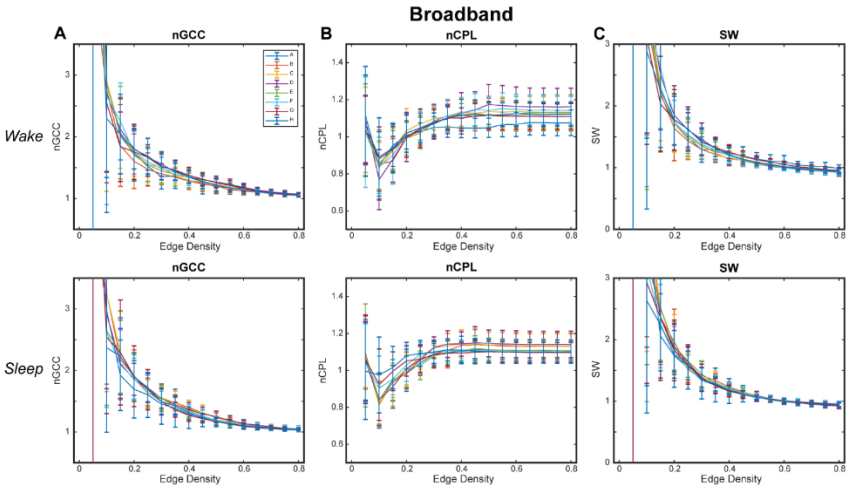

Figure 2.1 Changes in the (A) nGCC, (B) nCPL, and (C) SW as a function of varying edge density thresholds using broadband CC connectivity during wakefulness (top) and sleep (bottom), where lines A-H refer to each age group. Edge densities under 10% have high variability and can form unconnected graphs while edge densities over 40% result in networks resembling fully connected graphs, resulting in nGCC and SW values near 1. An edge density of 25% was chosen in the present study due to the lower variability between subjects while forming a connected graph. The overlap in error bars suggest that there is no significant difference between age groups, regardless of the edge density.

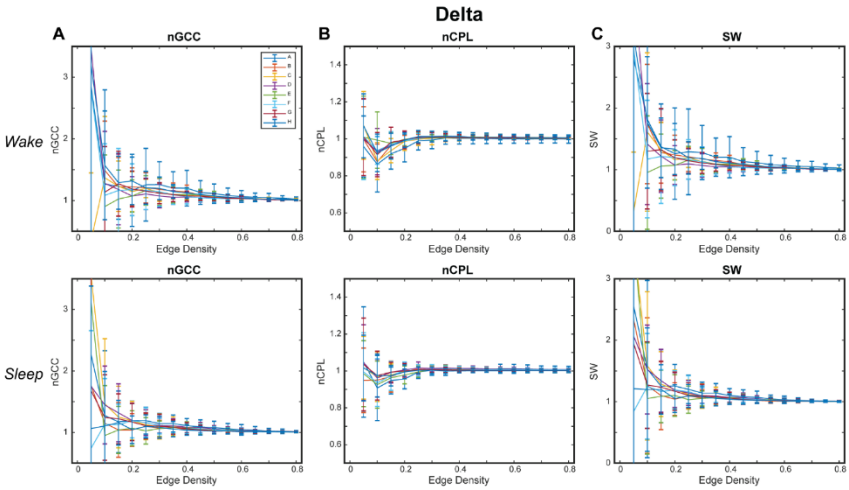

Figure 2.2 Changes in the (A) nGCC, (B) nCPL, and (C) SW as a function of varying edge density thresholds using delta wPLI connectivity during wakefulness (top) and sleep (bottom), where lines A-H refer to each age group. Edge densities under 10% have high variability and can form unconnected graphs while edge densities over 40% result in networks resembling fully connected graphs, resulting in nGCC and SW values near 1. An edge density of 25% was chosen in the present study due to the lower variability between subjects while forming a connected graph.

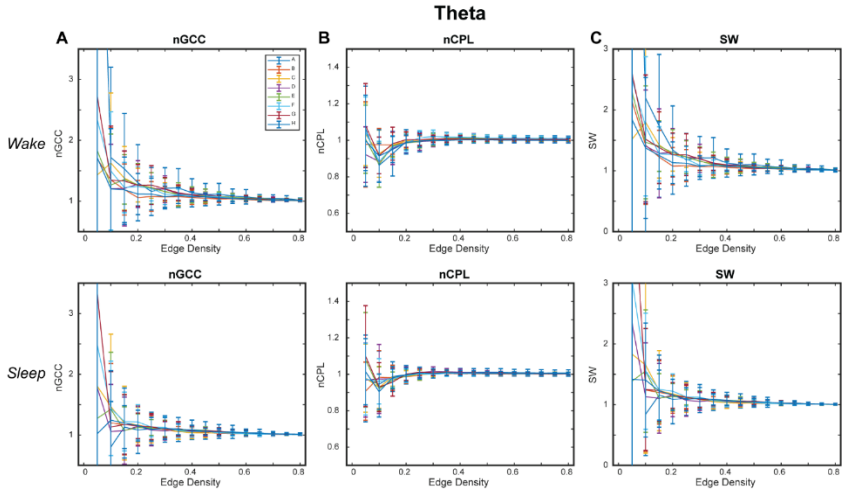

Figure 2.3 Changes in the (A) nGCC, (B) nCPL, and (C) SW as a function of varying edge density thresholds using theta wPLI connectivity during wakefulness (top) and sleep (bottom), where lines A-H refer to each age group. Edge densities under 10% have high variability and can form unconnected graphs while edge densities over 40% result in networks resembling fully connected graphs, resulting in nGCC and SW values near 1. An edge density of 25% was chosen in the present study due to the lower variability between subjects while forming a connected graph.

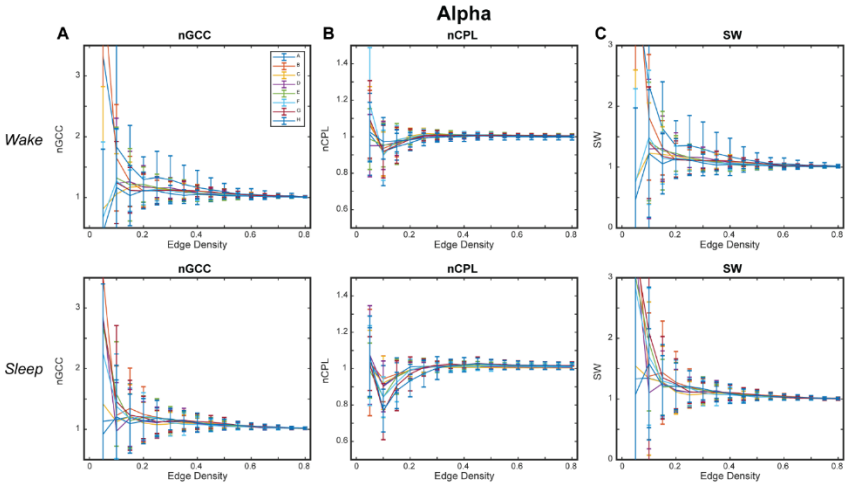

Figure 2.4 Changes in the (A) nGCC, (B) nCPL, and (C) SW as a function of varying edge density thresholds using alpha wPLI connectivity during wakefulness (top) and sleep (bottom), where lines A-H refer to each age group. Edge densities under 10% have high variability and can form unconnected graphs while edge densities over 40% result in networks resembling fully connected graphs, resulting in nGCC and SW values near 1. An edge density of 25% was chosen in the present study due to the lower variability between subjects while forming a connected graph.

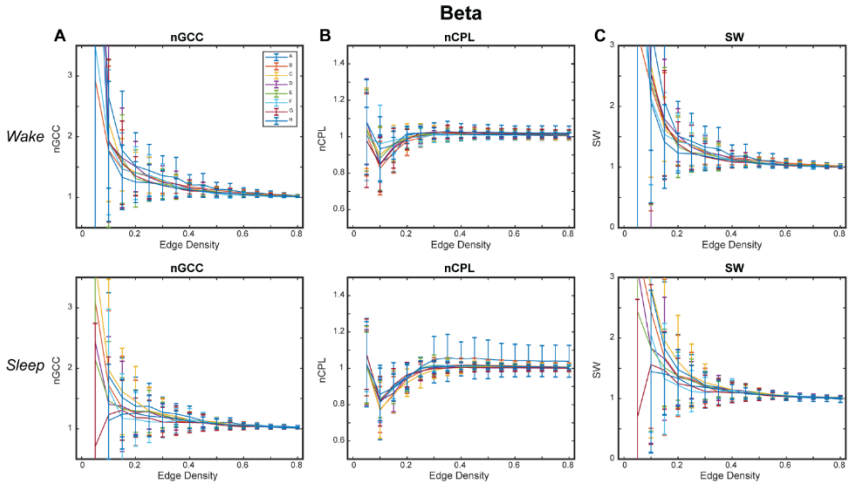

Figure 2.5 Changes in the (A) nGCC, (B) nCPL, and (C) SW as a function of varying edge density thresholds using beta wPLI connectivity during wakefulness (top) and sleep (bottom), where lines A-H refer to each age group. Edge densities under 10% have high variability and can form unconnected graphs while edge densities over 40% result in networks resembling fully connected graphs, resulting in nGCC and SW values near 1. An edge density of 25% was chosen in the present study due to the lower variability between subjects while forming a connected graph.

2.2.5 Statistical tests

Statistical analyses of the GT measures were conducted using one-way ANOVA tests across the eight age groups. Results were calculated independently for each connectivity method, frequency band, and sleep stage. The Bonferroni method was used to correct for multiple comparisons, accounting for 28 different age-group comparisons. The SW comparisons between CC and wPLI were measured in each age group using a one-tailed Wilcoxon signed-rank test, corrected using the Bonferroni method.

2.3 Results

2.3.1 CC FCNs increase in strength in early infancy

For the CC FCNs, both frontal connections (between electrodes Fp1, Fp2, Fz, F3, F4, F7, and F8) and occipital connections (between O1, O2, T5, and T6) were frequently among the top 10% strongest connections in the network; this was true across all age groups, during

wakefulness and sleep (Figure 2.6). However, the mean network strength increased after the first 3 months of infancy, as significant differences were found between subjects 0–3 months old and subjects 3–15 and 18–24-months old in wakefulness ($p < 0.01$, Figure 2.7A) and between 0–3 months old and 3–6-months old in sleep ($p < 0.05$, Figure 2.7B). For subjects older than 3 months, the only significant difference in network strength was a lower strength in subjects 15–18 months old relative to subjects 3–6 months old during sleep ($p < 0.05$, Figure 2.7B).

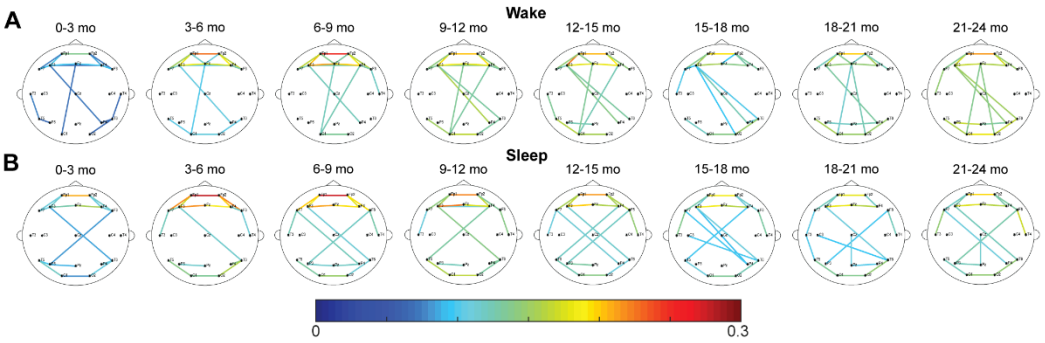

Figure 2.6 Average CC FCNs for healthy infants during (A) wakefulness and (B) sleep. The strongest 10% of connections in each age group are shown. The color of each connection represents the connection strength, defined as the percentage of epochs with significant connectivity values.

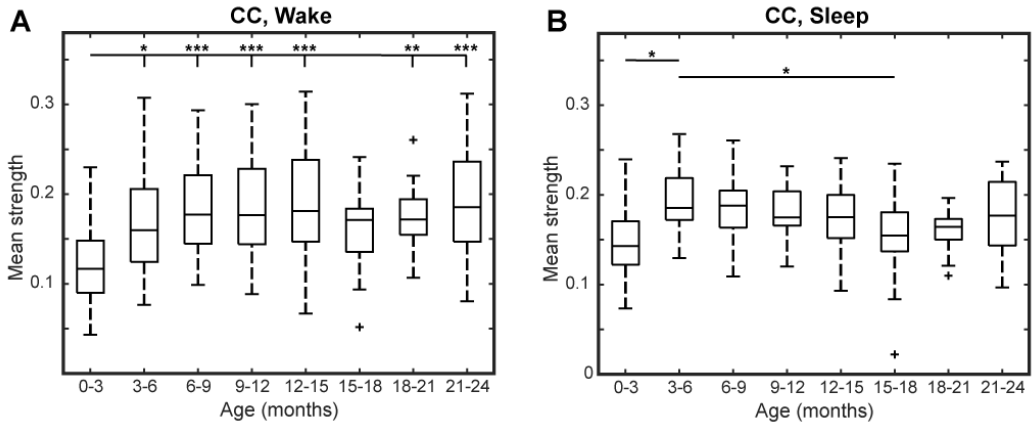

Figure 2.7 Mean network strength by age for healthy infants using CC connectivity during (A) wakefulness and (B) sleep. Here, mean network strength is defined as the mean of the 10% highest connectivity values. Significance levels are *$p < 0.05$, **$p < 0.01$, and ***$p < 0.001$, with p-values modified using the Bonferroni method.

2.3.2 WPLI FCNs in the alpha band increase in strength with age, particularly in the frontocentral region

The top 10% strongest wPLI connections for all age groups are shown in Figure 2.8A (delta band), Figure 2.8B (theta band), Figure 2.8C (alpha band), and Figure 2.8D (beta band). In the delta frequency band, the 0–3-months age group had significantly stronger connectivity than all other age groups, during both wakefulness and sleep ($p < 0.01$, Figure 2.9A). Connectivity strength in the theta band also decreased from the 0–3- months group to the 3–6 months group during wakefulness ($p < 0.05$), and to the 3–12 and 15–18 months groups during sleep ($p < 0.05$, Figure 2.9B). The only significant increases in connectivity strength in the delta and theta frequency bands were found in the theta band during wakefulness, where the FCNs in the 18–24 months group were stronger than in the 3–6 months group, and the 21–24 months group was stronger that the 6–9 months group ($p < 0.05$, Figure 2.9B).

In the alpha band during wakefulness, the FCN strength exhibited changes similar to those seen in the delta band, with significantly lower mean connectivity for subjects 3–24 months old compared to subjects 0–3 months old ($p < 0.05$, Figure 2.9C, top). In contrast, during sleep, the alpha band connectivity strength exhibited a significant increase during the first 2 years of life. Specifically, subjects in the 18–21 months age group had significantly stronger FCNs than subjects 3–9 months old ($p < 0.05$, Figure 2.9C bottom), and subjects 21–24 months old had significantly stronger FCNs than subjects 3–12 months old ($p < 0.01$, Figure 2.9C, bottom). Qualitatively, this change appeared to be driven by strong frontocentral connections (between electrodes Fp1, Fp2, Fz, F3, F4, F7, F8, C3, Cz, and C4), as the strongest 10% of connections for subjects 12–24 months old tended to be clustered in this region (Figure 2.8C, bottom).

The strongest 10% of connections in the beta band during sleep were also clustered in the frontocentral regions for subjects 3–24 months old, based on a qualitative visual analysis (Figure 2.8D). However, unlike the alpha band, there were no significant differences in

connectivity strength between age groups (Figure 2.9D, bottom). During wakefulness, the beta band FCNs exhibited stronger connections for subjects 0–3 months old compared to most age groups from 12 to 24 months old, similar to the trends in the delta and alpha bands during wakefulness ($p < 0.05$, Figure 2.9D, top). In the beta band, the 3–6 months group also exhibited stronger connections than the 21–24 months group ($p < 0.05$, Figure 2.9D, top).

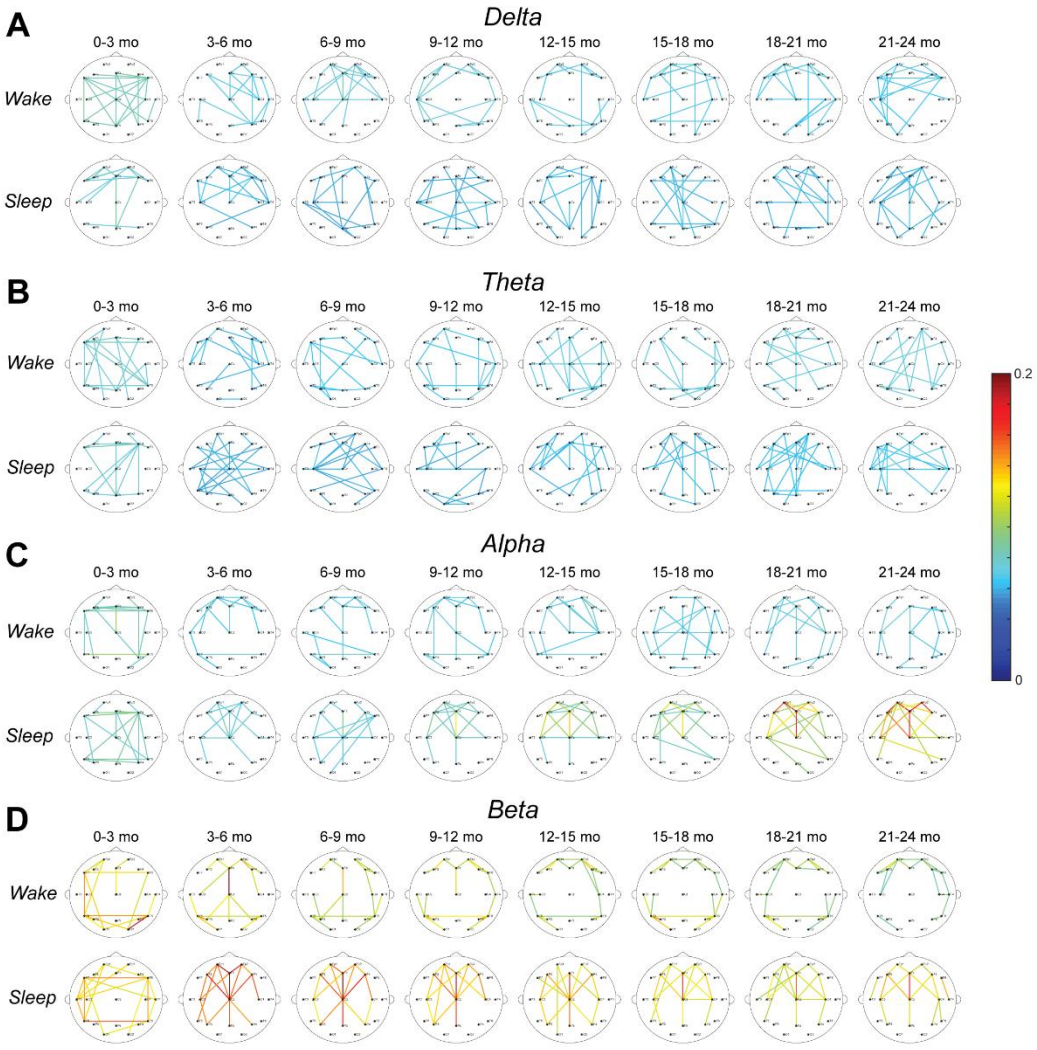

Figure 2.8 Average wPLI FCNs for healthy infants in the (A) delta, (B) theta, (C) alpha, and (D) beta band during wakefulness (top) and sleep (bottom). The strongest 10% of connections in each age group are shown. The color of each connection represents the connection strength, defined as the percentage of epochs with significant connectivity values.

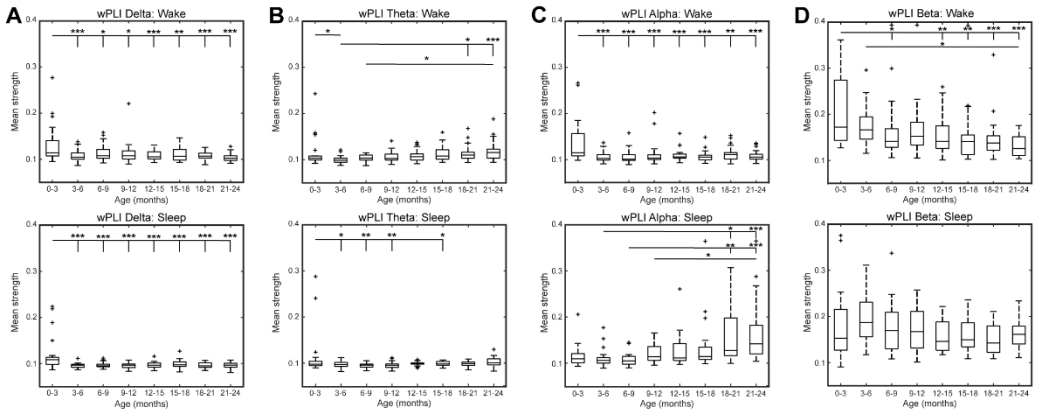

Figure 2.9 Mean network strength by age using wPLI connectivity in the (A) delta, (B) theta, (C) alpha, and (D) beta band during wakefulness (top) and sleep (bottom). Here, mean network strength is defined as the mean of the 10% highest connectivity values. Significance levels are *$p < 0.05$, **$p < 0.01$, and ***$p < 0.001$, with p-values modified using the Bonferroni method.

2.3.3 CC FCNs exhibit small-world features across all age groups

The nGCC across all subjects indicates the presence of nonrandom clusters within the network during wakefulness [$nGCC_{wake}$ = 1.75 (0.38), reported as the median (IQR) for all results] and sleep [$nGCC_{sleep}$ = 1.70 (0.39)] (Figure 2.10A). The nCPL across all subjects was close to one during wakefulness [$nCPL_{wake}$ = 1.05 (0.11)] and sleep [$nCPL_{sleep}$ = 1.06 (0.10)], suggesting that the efficiency of information transfer in the CC network was high, similar to a random network (Figure 2.10B). CC networks demonstrated a small-world structure across all age groups in wakefulness [SW_{wake} = 1.64 (0.49)] and sleep [SW_{sleep} = 1.59 (0.34)] (Figure 2.10C). There were no significant differences between age groups for nGCC (wakefulness and sleep), CPL (sleep), or SW (sleep). The nCPL during wakefulness was significantly larger in subjects 6–9 months old compared to 9–12 months old ($p < 0.05$, Figure 2.10B, top), and SW during wakefulness was significantly larger in subjects 9–12 months old compared to subjects 0–3 months old ($p < 0.01$, Figure 2.10C, top).

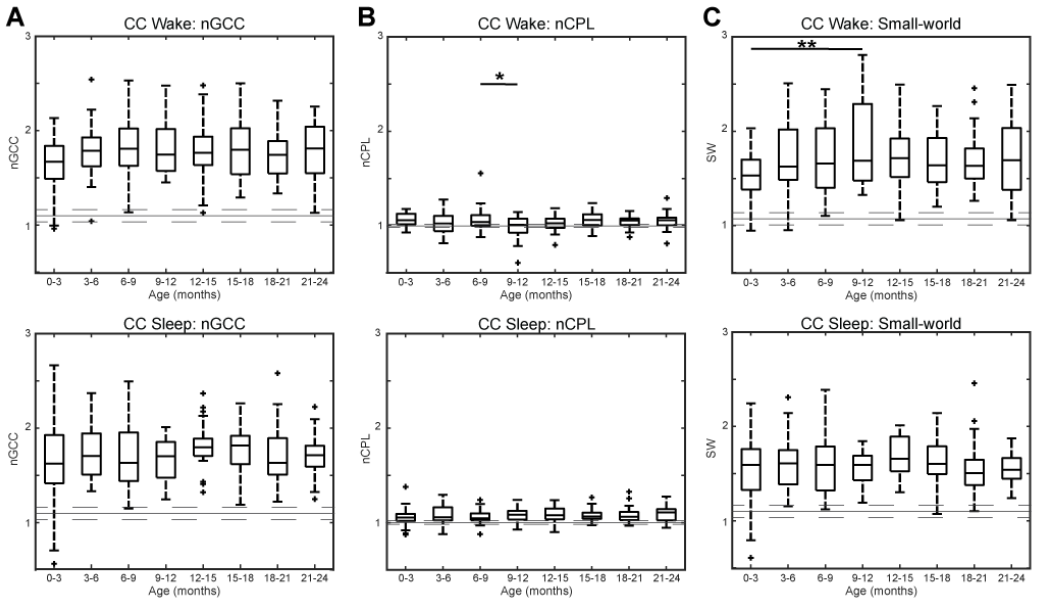

Figure 2.10 Graph theory measures by age for healthy infants using CC connectivity for the (A) normalized global clustering coefficient, (B) normalized characteristic path length, and (C) small-world measure during wakefulness (top) and sleep (bottom). For each subfigure, the solid gray line represents the median value using randomly rewired networks and the dashed gray lines represent the 25th and 75th percentiles. Significance levels are *p < 0.05, **p < 0.01, and ***p < 0.001, with p-values modified using the Bonferroni method.

2.3.4 WPLI FCNs have less clustering and are less small-world than CC networks

WPLI networks generally followed the same trend as CC networks, with nGCC values greater than one and nCPL values of approximately one in all frequency bands. The SW measures for all frequency bands are shown in Figure 2.11; see Figures 2.12, 2.13 for the nGCC and nCPL results, respectively. The wPLI FCNs were small-world, with SW values greater than one in the delta [SW_{delta}, wake = 1.18 (0.32), SW_{delta}, sleep = 1.12 (0.28)], theta [SW_{theta}, wake = 1.17 (0.27), SW_{theta}, sleep = 1.12 (0.30)], alpha [SW_{alpha}, wake = 1.15 (0.33), SW_{alpha}, sleep = 1.16 (0.33)], and beta [SW_{beta}, wake = 1.32 (0.46), SW_{beta}, sleep = 1.24 (0.52)] bands. The wPLI FCNs in the delta band had a significantly higher nGCC and SW during sleep at 0–3 months compared to 6–9 months and 18–21 months ($p < 0.05$, Figure 2.11A bottom and Figure 2.12A bottom). No significant differences in nGCC, nCPL, or SW were seen between age groups in the theta and alpha bands (Figures 2.11B,C and Figures 2.12B,C, 2.13B,C). The wPLI

networks in the beta band were typically less SW with age, with significantly smaller SW at 21–24 months compared to 0–3 months during wakefulness ($p < 0.05$) and smaller SW at 15–18 and 21–24 months compared to 6–9 months ($p < 0.05$) during sleep (Figure 2.11D). The CC networks had significantly higher SW values compared to wPLI networks for all groups aged 3–24 months in the delta, theta, and alpha bands during wakefulness and sleep (Table 2.4; Wilcoxon sign-rank test, Bonferroni corrected). In the beta band, CC networks were more small-world than wPLI networks across most age groups older than 3 months during wakefulness and 12 months during sleep (Table 2.4).

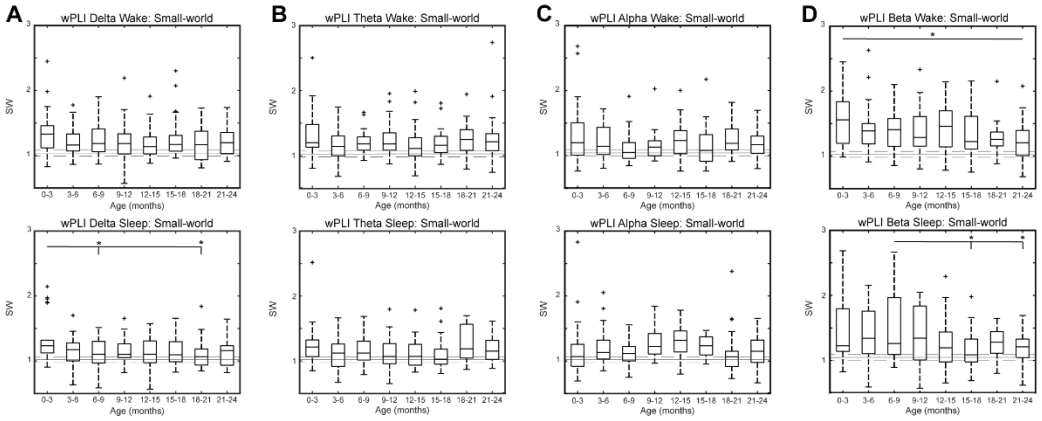

Figure 2.11 Small-world measure by age for healthy infants using wPLI connectivity in the (A) delta, (B) theta, (C) alpha, and (D) beta band during wakefulness (top) and sleep (bottom). For each subfigure, the solid gray line represents the median value using randomly rewired networks and the dashed gray lines represent the 25th and 75th percentiles. Significance levels are *$p < 0.05$, **$p < 0.1$, and ***$p < 0.001$, with p-values modified using the Bonferroni method.

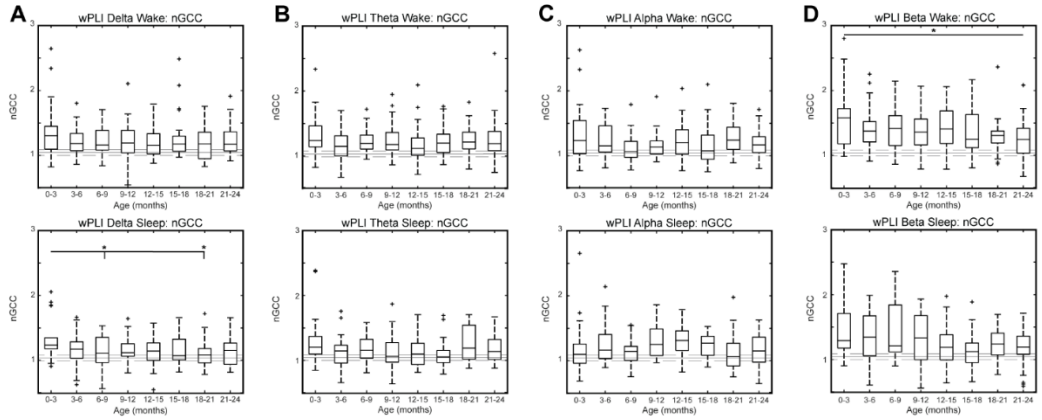

Figure 2.12. Normalized global clustering coefficient (nGCC) by age for healthy infants using wPLI connectivity in the (A) delta, (B) theta, (C) alpha, and (D) beta bands during wakefulness (top) and sleep (bottom). The solid line represents the median values using randomly rewired networks and the dashed lines represent the 25th and 75th percentiles. Significance levels are * p<.05, ** p<.01, *** p<.001, with p-values modified using the Bonferroni method.

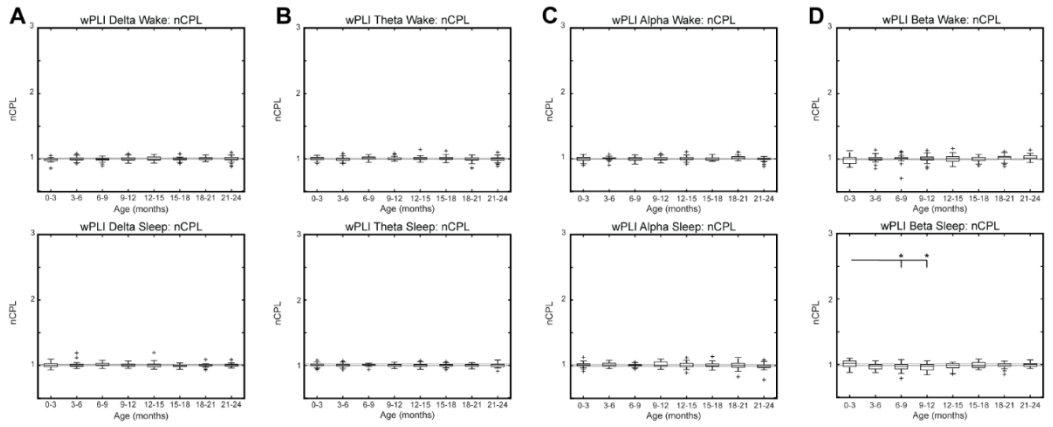

Figure 2.13. Normalized characteristic path length (nCPL) by age for healthy infants using wPLI connectivity in the (A) delta, (B) theta, (C) alpha, and (D) beta bands during wakefulness (top) and sleep (bottom). The solid line represents the median values using randomly rewired networks and the dashed lines represent the 25th and 75th percentiles. Significance levels are * p<.05, ** p<.01, *** p<.001, with p-values modified using the Bonferroni method.

Table 2.4. *P-values for the statistical comparisons of the small-world measure between CC and wPLI FCNs in individual subjects. Significant p-values are bolded and corrected for FDR using Bonferroni correction (n=8).*

		SW comparison			
State	*Age group*	*CC>Delta*	*CC>Theta*	*CC>Alpha*	*CC>Beta*
Wake	0-3 m.	0.21	0.027	0.063	0.57
	3-6 m.	**4.65e-6**	**3.10e-6**	**6.92e-6**	**4.34e-4**
	6-9 m.	**1.99e-5**	**1.35e-6**	**1.85e-6**	**0.0034**
	9-12 m.	**1.24e-5**	**4.21e-6**	**1.35e-6**	**2.12e-4**
	12-15 m.	**6.92e-6**	**6.27e-6**	**7.64e-6**	**0.0022**
	15-18 m.	**8.99e-5**	**1.47e-5**	**4.26e-6**	**5.87e-4**

	18-21 m.	**2.06e-6**	**1.24e-5**	**4.65e-6**	**3.16e-5**
	21-24 m.	**9.17e-5**	**3.47e-5**	**2.40e-5**	**1.18e-4**
Sleep	0-3 m.	0.077	0.012	**0.0010**	0.21
	3-6 m.	**2.42e-5**	**9.91e-6**	**6.96e-5**	0.025
	6-9 m.	**2.06e-6**	**6.92e-6**	**1.24e-5**	0.17
	9-12 m.	**7.66e-5**	**1.83e-5**	**7.97e-4**	0.050
	12-15 m.	**3.17e-5**	**3.17e-5**	**3.17e-5**	**2.48e-4**
	15-18 m.	**6.49e-6**	**2.10e-5**	**1.00e-5**	**2.10e-5**
	18-21 m.	**1.38e-4**	**0.0014**	**5.21e-4**	**9.14e-4**
	21-24 m.	**1.42e-5**	**1.42e-5**	**4.27e-5**	**2.34e-5**

2.4 Discussion

In this study, we measured age-related changes in functional connectivity in a large cohort of healthy infants (n = 240) using CC and wPLI. CC FCNs maintained a consistent small-world structure (SW > 1), with connections that increased in strength after the first 3 months of life. The wPLI FCNs in the delta and theta bands (wakefulness and sleep), alpha band (wakefulness), and beta band (wakefulness) exhibited significantly decreased strength after 3 months of age. However, in the alpha band during sleep, wPLI connectivity significantly increased in strength in infants older than 21 months. The wPLI networks also exhibited a small world structure, but the locations of the strongest connections differed from the CC networks. For both CC and wPLI, the graph theory metrics showed few significant differences between age groups, suggesting that these features of the network structure stay relatively consistent during infancy.

2.4.1 Connectivity changes in CC networks during infant development

The CC network structure in the present study was qualitatively similar to that found for healthy infant controls in our prior work, with the strongest connections located in the frontal and posterior head regions (Shrey et al. 2018b; Smith et al. 2021a). Our prior study also reported stronger FCNs during sleep compared to wakefulness in a cohort of infants with a mean age of 6.3 ± 3.1 months old (Smith et al. 2021a), and we saw similar results here in subjects 0–9 months old (Figure 2.7). Consistent with our results, Gao et al. (2011) found a significant increase in fMRI connectivity strength and global efficiency in the first year of infancy and a stable network strength during the second year. An EEG study using the same CC connectivity method on healthy subjects 0–18 years old during N2 sleep also reported low network strength during infancy that began to significantly increase after 5 years of age (Chu et al. 2014). Our results are generally consistent with prior studies suggesting that FCNs based on broadband EEG strengthen with age, presumably continuing into adulthood. This increase in connectivity strength may also reflect the myelination of white matter tracts during the first year of infancy, which correlates with increased fractional anisotropy on MRI diffusion tensor imaging (Hermoye et al. 2006). While we found significant changes that occur during the first 2 years of development, these changes appear to be subtle relative to those reported later in life.

2.4.2 Connectivity changes in wPLI networks during infant development

In the delta and theta frequency bands, the 10% strongest connections in the wPLI FCNs appeared highly variable across age groups, likely due to the application of thresholding to relatively weak networks (note the overall low strength for delta and theta in Figure 2.9). However, wPLI connectivity strength in delta, alpha, and beta frequencies during wakefulness, as well as delta and theta frequencies during sleep, were significantly higher in subjects 0–3 months than other age groups, consistent with prior work describing a decrease in density of

FCNs based on EEG coherence during the first 6 months of infancy in the delta, theta, and alpha bands (Chu et al. 2014). The increase in wPLI strength in the alpha band during sleep, with the 10% strongest connections located primarily in frontocentral regions, is complementary to prior wPLI studies of different age groups. For example, stronger alpha and theta band frontoparietal connections were seen in full-term infants relative to preterm newborns, suggesting developmental changes in these frequency bands (Omidvarnia et al. 2014; Tóth et al. 2017). Furthermore, the strongest wPLI functional connections were found in the alpha band in children 5–11 years old (Ortiz et al. 2012; Choi et al. 2019). The increase in alpha band connectivity during N2 sleep at around 21 months may also be related to the fact that sleep spindles are asynchronous in early infancy and become mostly synchronous by age two (Gruber and Wise 2016; Louis et al. 2016; Goetz et al. 2021). While adult sleep spindles primarily have peak frequencies in the beta band (12–15 Hz), the strong networks we reported in both the alpha and beta bands during N2 sleep are consistent with reports of two types of spindles in children: slow spindles (peak frequency 11–12.75 Hz) occurring in frontal channels (Fz, F3, and F4), and fast spindles (12.5–14.5 Hz) localized to centroparietal channels (Cz and Pz) (Shinomiya et al. 1999b). The presence of these two spindle types continues into adulthood, with the peak frequency of both spindle types increasing linearly with age (Shinomiya et al. 1999b; Schabus et al. 2007; Mölle et al. 2011).

We found that infant FCNs were small-world across all ages, frequency bands, and states of vigilance, concordant with prior reports of small-world EEG networks immediately following birth (Omidvarnia et al. 2014; Tóth et al. 2017) and during childhood (Boersma et al. 2011). The presence of small-world networks has also been reported in studies utilizing DTI (Yap et al. 2011), volume-based MRI (Fan et al. 2011), and MEG synchronization likelihood (Berchicci et al. 2015), where infant brain networks were small-world at birth and increased in clustering and efficiency with age. We saw a few significant changes in nGCC, nCPL, and SW across different age groups and frequency bands; however, these differences typically involved

only two to three age groups and did not suggest a consistent trend related to development. This may be related to the prior suggestion that the most dramatic changes in GT measures occur later in life, from childhood to adulthood (Chu et al. 2014; Berchicci et al. 2015).

2.4.3 Differences between CC and wPLI connectivity

We chose to quantify and characterize the functional networks of our subjects using two complementary computational techniques: cross-correlation and weighted phase lag index. Prior work has shown that the differences in networks produced by each method cannot wholly be explained by the differences in sensitivity to linear and nonlinear features of the data, suggesting that the results may be affected by other unknown elements as well (Siems and Siegel 2020). The differences in FCNs using different connectivity techniques may be explained by the distinct neural mechanisms underlying cortical phase- and amplitude-coupling, which are also frequency specific (Tokariev et al. 2016; Siems and Siegel 2020). Our results indicated several differences between CC and wPLI FCNs, notably an increase in CC connectivity strength after 3 months of age contrasted with a decrease in wPLI strength in the same time frame. Using different connectivity techniques on the same dataset highlighted distinct aspects of the infant functional networks.

The use of bivariate connectivity methods such as CC and wPLI may result in spurious connections in the FCNs due to the presence of volume conduction. In particular, this can occur when one source drives activity in multiple channels, resulting in false connectivity between all secondary channels (Blinowska and Kaminski 2013). However, the results in the present study should be minimally impacted by this for three reasons: 1) Our application of CC for functional connectivity includes a step to remove zero-lag connections, which has been shown to counteract volume conduction (Chu-Shore et al. 2012). 2) wPLI inherently reduces the impact of volume conduction by minimizing connections with phase differences at zero and pi (Vinck et al. 2011). 3) If we assume that any remaining effects of volume conduction would impact each

subject approximately equally, then any differences we noted in FCNs between subject groups (calculated with the same connectivity technique) should not be spuriously arising from volume conducted sources. Future studies could utilize multivariate connectivity methods to minimize any such spurious connections (Blinowska 2011).

2.4.4 Normalization and thresholding in FCNs

While our report of a small-world network configuration is consistent with prior literature, the result of SW > 1 is heavily influenced by the choice of thresholding technique applied to the adjacency matrix. Dividing each FCN by its strongest connection addresses the influence of connectivity strength on the nGCC, nCPL, and SW measures, but it may introduce bias to the GT measures because it gives equal weight to all FCNs, even those with very weak connections (van Wijk et al. 2010). Similarly, using a fixed edge density for GCC, CPL, and SW measures can potentially exclude strong edges or include weak edges in the network, causing spurious results (van den Heuvel et al. 2017). Here, we chose to preserve the weight of each connection to create a pseudo-binary network, as a means of retaining the relative strength in each connection and reducing the effect of weaker edges on the GT measures.

2.4.5 Limitations

Our results are limited by several factors that should be addressed in future investigations. The use of clinical infant EEG limits the number of nodes in the FCN to nineteen (corresponding to the number of electrodes), which restricts the topological characterization of the FCNs; future studies may wish to introduce higher density EEGs for more detailed topological analysis. In addition, GT metrics cannot be used to draw conclusion about the specific network structure; for example, dramatically different networks can have similar values for clustering or path length. This could be addressed by applying statistical tests to individual network connections across age groups. It is also worth noting that the EEGs obtained for the

study were recorded from infants referred for diagnostic evaluation of suspected seizures. While they were found to be neurologically normal with no abnormal EEG findings, future studies should consider prospective collection of data from healthy infants. Moreover, we did not directly identify and correct for eye movements in the EEG data, which could influence the connectivity results in the frontal brain regions. However, we expect minimal eye movements during N2 sleep, and the most relevant prior literature did not include this preprocessing step (Chu et al. 2014; Shrey et al. 2018b; Smith et al. 2021a), so the methods used here facilitate the most direct comparison of results. Finally, the use of a cross-sectional population made it impossible to assess developmental changes in individual cases; future developmental studies should aim to include longitudinally collected EEG data.

2.5 Conclusion

Studies of healthy brain networks in the infant brain are critical for understanding both normal brain development and disease states, such as epilepsy. This has the potential to lead to identification of novel functional connectivity biomarkers to aid clinical diagnosis and treatment, improving the care of children with neurological diseases.

CHAPTER III

Effect of Interictal Epileptiform Discharges on EEG-based Functional Connectivity Networks

3.1 Introduction

Functional connectivity is a brain mapping technique based on the statistical interdependencies of spatially-distinct time-varying neural signals. Functional connectivity networks (FCNs) can provide valuable information about cortical network organization in both healthy subjects and those with epilepsy (Van Den Heuvel and Pol 2010; Kramer and Cash 2012; Van Diessen et al. 2013). Of the wide variety of imaging modalities used for functional connectivity, scalp electroencephalogram (EEG) is desirable due to its accessibility, low cost, standardized clinical application, noninvasive nature, and high temporal resolution. EEG-based FCNs have been used to characterize pathological networks associated with temporal lobe epilepsy (Quraan et al. 2013), benign epilepsy with centrotemporal spikes (Clemens et al. 2016; Mahmoudzadeh et al. 2016), and generalized pharmacoresistant epilepsies (Horstmann et al. 2010). When these FCNs are based on cross-correlation or coherence techniques using at least 100 seconds of EEG data, the networks exhibit stability over time, making them suitable for assessing an underlying disease state (Chu-Shore et al. 2012). For example, in infantile spasms (IS) subjects, strong, stable FCNs were found to underlie the chaotic EEG waveforms associated with hypsarrhythmia (Shrey et al. 2018a).

In EEG-based FCNs, the inherent non-stationarity of the signal remains a challenge for analysis. For example, interictal epileptiform discharges (IEDs) are transient electrographic events that occur intermittently between seizures and are frequently recorded by EEG (de Curtis et al. 2012). In recent studies, IEDs have been shown to be correlated with a subject's FCN, suggesting that the alteration of the baseline functional network may reflect pathological activity

(Ponten et al. 2009; Horstmann et al. 2010; Adebimpe et al. 2015; Coito et al. 2016). While this prior work demonstrated that changes in FCNs occur during an IED, it is unknown whether these connectivity changes are driven purely by the morphology of the spike-wave complex (and its effect on the calculation of connectivity) or by the pathological network activity underlying the IED's generation.

The goal of this study was to understand the effects of IEDs on FCNs from both methodological and physiological perspectives. Methodologically, we tested whether the presence of focal, high amplitude spike-wave complexes could cause spurious functional connectivity measurements. This was done by adding simulated focal IEDs at varying rates and amplitudes to the sleep EEG of control subjects and measuring the associated changes in the FCN. Once we understood the methodological effects of the IED waveform, we compared these results to the physiological changes in the FCNs derived from the sleep EEG of IS subjects exhibiting focal IEDs. IS subjects were chosen for this study due to the high epileptiform discharge amplitudes associated with this disease (Frost Jr et al. 2011). Based on prior EEG-based FCN studies, we hypothesized that the occurrence of focal IEDs would be associated with a local increase in functional connectivity strength (Wilke et al. 2011; Clemens et al. 2016) and the activation of a unique IED FCN (Ponten et al. 2009; Horstmann et al. 2010).

3.2 Methods

3.2.1 Subject information

Approval for this study was obtained from the Institutional Review Board of the Children's Hospital of Orange County (CHOC), with the requirement for informed consent waived. We retrospectively identified eight infants (7F, 1M, aged 10.3±6.4 months) who were diagnosed with new-onset epileptic spasms and underwent scalp EEG recording prior to treatment. We also retrospectively identified eight control subjects (5F, 3M, aged 10.5±6.8 months) who (1) had no known neurological disorders, (2) underwent routine EEG for clinical

evaluation, and (3) had EEGs that were interpreted as normal by a board-certified pediatric epileptologist (DS). All subjects had EEG recordings performed at CHOC.

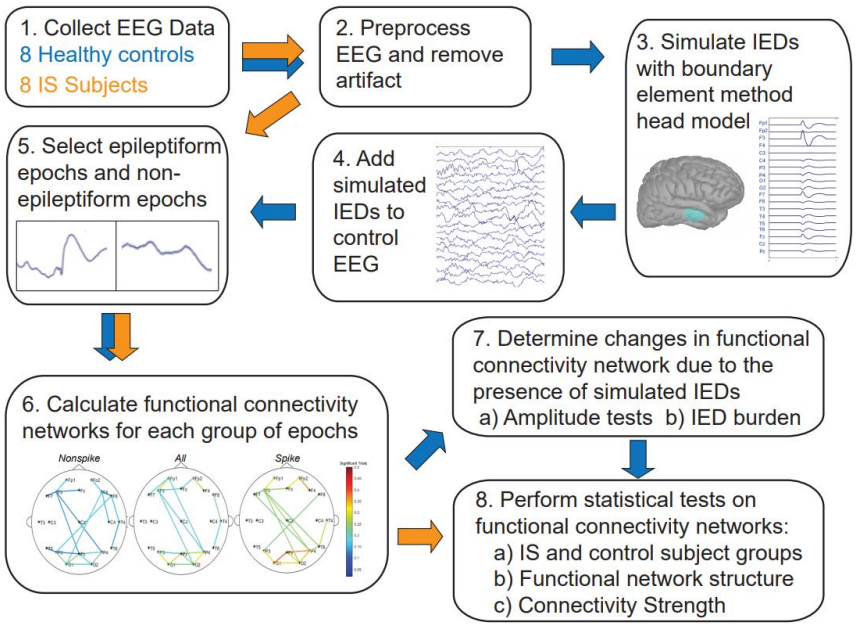

Figure 3.1. Summary of the functional connectivity analysis. Blue arrows indicate the data analysis procedure for the control subject EEG, while orange arrows indicate the procedure for analysis of EEG data from subjects with epilepsy.

3.2.2 EEG acquisition and preprocessing

All EEG data was recorded by the Nihon Kohden EEG acquisition system, with nineteen scalp electrodes placed according to the international 10-20 system, at a sampling rate of 200 Hz. For each subject, one interictal segment of non-REM sleep EEG lasting at least fifteen minutes was selected for analysis. Artifacts caused by muscle activity, movement, and poor electrode contact were marked by a board-certified epileptologist (DS). All electronic data were deidentified and analyzed using custom MATLAB (Mathworks) scripts. All EEG data were filtered with a third-order Butterworth filter with zero-phase shift digital filtering from 0.5-55 Hz and re-referenced to the common average. The data were then windowed into one-second epochs for connectivity analysis. Any epoch containing a marked artifact was discarded for all EEG channels after filtering. This data analysis procedure, including the subsequent calculation

of functional connectivity, is summarized in Figure 3.1.

3.2.3 EEG data segmentation for IS subjects

For each IS subject, the EEG data was segmented into three different groups: (1) all one-second epochs (ALL), (2) one-second epileptiform epochs (EE) containing an IED, and (3) one-second non-epileptiform epochs (NEE) containing no IEDs (Figure 3.2A). Focal IEDs were manually marked by a board-certified epileptologist (DS) based on the waveform morphology and the local field in adjacent electrodes. For each subject, the EEG channel containing the largest number of IEDs was selected for analysis. One epileptiform epoch was created for each IED within that channel, defined as the EEG data from all electrodes in a window of [-500, 500] milliseconds, centered on the spike. Each epoch was visually inspected to ensure that it contained only a single spike. The spike amplitude was defined as the EEG range within a [-50, 50] millisecond window centered around the spike, while background amplitudes were defined as the mean range of four 100-millisecond windows prior to the spike in each EE ([-500, -400], [-400, -300], [-300, -200], and [-200, -100] milliseconds). Non-epileptiform epochs were visually marked as one-second of EEG containing no epileptiform discharges in any channel.

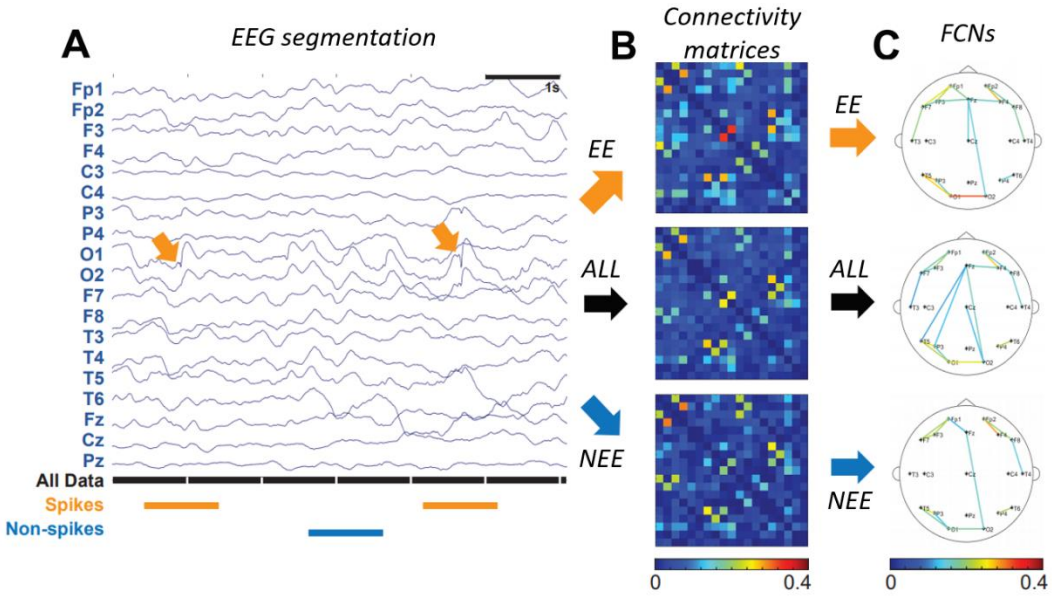

Figure 3.2. (A) Sample of EEG data segmentation. Orange segments are 1s epochs containing an IED (termed EE), black segments are all 1s epochs (ALL), and blue segments are 1s epochs with non-spike activity (NEE). (B) Connectivity matrices for spikes (orange arrow), all data (black arrow), and nonspikes (blue arrow), represented as a percentage of significant connections. (C) FCNs for EE (orange arrow), ALL (black arrow), and NEE (blue arrow). For clarity, only the strongest 10% of all connections are shown.

3.2.4 Simulation of IEDs in control subject EEGs

To assess the effect of IED waveforms on the FCN calculation, we simulated IEDs and added them to control sleep EEG recordings. Simulated IEDs were generated within a realistic head model using the Brainstorm software (Tadel et al. 2011). The realistic head model was based on the magnetic resonance imaging template brain volume in the ICBM 152 atlas (Fonov et al. 2011). The atlas was used with boundary element methods (BEM) to generate a three-layered geometric head model, consisting of the scalp, inner skull, and outer skull with a conductivity ratio of 1:0.0125:1, respectively.

IED simulations were based on the equivalent current dipole method, where it is assumed that the spike potential is generated from a primary dipole source (Koles 1998; Grova et al. 2006). Here, we chose a single patch of activated cortex located underneath the F3 electrode, with the corresponding dipole oriented normal to the selected region. The region of activated cortex was 7-10 cm^2, concordant with the typical surface area of cortex necessary to produce epileptiform discharges that are detectable on scalp EEG (Grova et al. 2006; Tao et al. 2007). We then modelled the time course of the spike-wave complex as a combination of three half-period sine waves within a one-second window. The simulated spike was represented by a positive half-period sine wave 60 milliseconds long, followed by a slow wave consisting of sequential negative and positive half-period sine waves lasting 120 milliseconds and 200 milliseconds, respectively (Figure 3.3). The amplitude ratio for each half-wave was 5:4:2, which was chosen to approximate the average characteristics of IEDs marked in IS subjects. The IED field across all nineteen electrodes was computed using forward modelling with the OpenMEEG

software, incorporating the generated simulated spike waveform and geometric head model.(Kybic et al. 2005; Gramfort et al. 2010). To simulate the sporadic occurrence of IEDs, the IED waveform was added to a randomly selected subset of nonoverlapping one-second EEG epochs, with the peak of the spike aligned to the center of each epoch.

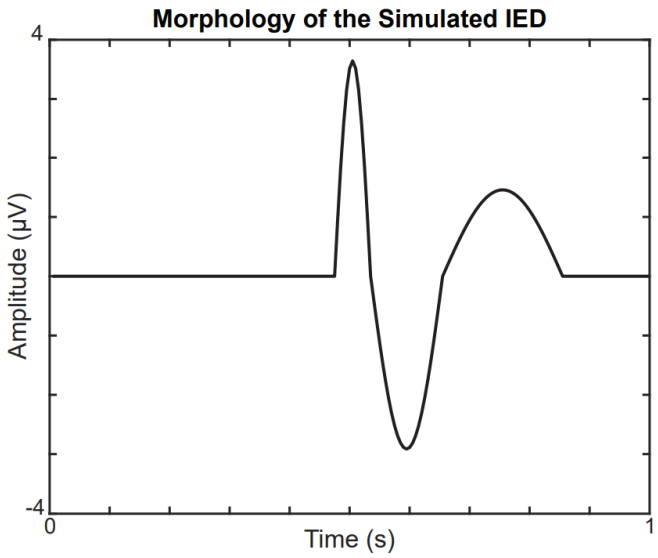

Figure 3.3. Morphology of the simulated IED at the focal electrode F3. The amplitude of the IED is scaled to match the spike:background ratio of IS subjects

3.2.5 Calculation of the functional connectivity network

For each subject, FCNs were calculated using linear cross-correlation, as previously described in (Kramer et al. 2009; Chu-Shore et al. 2012; Shrey et al. 2018a). This technique has been shown to provide accurate measurements for both real and simulated electrophysiological data (Jiruška et al. 2005) and generate stable FCNs when using at least 100 seconds of data (Chu-Shore et al. 2012). Prior to FCN analysis, the data in each one-second epoch was normalized in each channel to have zero mean and unit variance. To calculate the coupling strength between each electrode pair, we first calculated the maximal absolute value of the cross-correlation with a maximum lead/lag time of 200 milliseconds. This maximum lead/lag was chosen based on typical times for neurophysiological processes and cross-cortical conduction

times (Chu-Shore et al. 2012). Connectivity values were normalized based on the autocorrelation of the signal at the chosen lead/lag time. We then applied a Fisher z-score transformation, resulting in an adjacency matrix containing the z-score between each electrode pair for each one-second epoch.

The significance of the coupling for each one-second epoch was determined by comparing each electrode pair's z-score value to a null distribution generated using permutation resampling. In each iteration of resampling, we computed the maximal absolute value of the cross-correlation (with a max lead/lag of 200 milliseconds) between random one-second epochs for each channel, after excluding epochs containing artifacts. This was repeated 1000 times to create a normal distribution of z-scores for each electrode pair under the null hypothesis that there was no temporal relationship between the two channels. The cross-correlation in each one-second epoch was considered statistically significant if the computed z-score value was higher than the 95^{th} percentile of the null distribution.

To prevent spurious connections due to volume conduction, any z-score with a maximal cross-correlation at a zero-time lag was considered non-significant (Chu-Shore et al. 2012). The results for each one-second epoch were stored in a binary adjacency matrix, where a value of one represented a significant, non-volume conducted connection. We then averaged the binary adjacency matrices to produce a connectivity matrix where each element represented the percentage of significant connections between the electrode pairs over the duration of the recording (Figure 3.2B). For visualization, we created topographical network maps by applying a threshold to the connectivity matrix (Figure 3.2C).

For each IS subject, three different FCNs were constructed using the ALL, EE, and NEE epochs segmented from the EEG. In control subjects, we generated one FCN from the control EEG before adding simulated IEDs (CONTROL) and three FCNs from control EEG with simulated IEDs using different subsets of epochs: (1) All epochs after adding simulated IEDs (ALL), (2) only epochs containing simulated focal IEDs (EE), and (3) only epochs not containing

simulated IEDs (NEE). The same null distribution was used for calculating the FCNs of the ALL, EE, and NEE groups. To measure the variance of our results, we performed 250 iterations of FCN generation for each control subject, with each iteration containing simulated IEDs in randomly selected epochs.

3.2.6 Statistical tests for network structure

To quantify the differences in network structure between two FCN's, we used two different metrics: the relative graph edit distance (rGED) and 2D correlation. The rGED is a novel method based on the principles of the graph edit distance that measures the similarity between two binary graphs with the same number of vertices and edges (E) (Sanfeliu and Fu 1983). The rGED is calculated based on the minimum number of insertions (I) and deletions (D) required to transform one of the graphs into the other one: $rGED = 1 - \frac{I+D}{2E}$. An rGED of zero indicates that there are no connections in common, while an rGED of one indicates that both networks have all connections in common. To calculate the rGED between two FCNs, we binarize each connectivity matrix by assigning the strongest ten percent of connections a "1" and all other connections a "0".

The 2D correlation measures the similarities across the entire FCN rather than focusing on the strongest connections, as is done with the rGED. Using 2D correlation also obviates the need for thresholding, which can potentially bias the measurement. Both the rGED and 2D correlation tests were used to compare the ALL to EE, ALL to NEE, and EE to NEE networks in IS and control subjects. The 2D correlation was also used to compare the differences in network structure between IS and control FCNs. Specifically, we compared the ALL FCN of each IS subject to the ALL FCNs of all other IS subjects (n=28 comparisons), the CONTROL FCN of each control subject to the CONTROL FCNs of all other control subjects (n=28), and the ALL FCN of each IS subject to the CONTROL FCNs of all control subjects (n=64). Comparisons

between these distributions show the uniformity of FCNs within each group, compared to comparisons across different groups.

3.2.7 Statistical tests for connectivity strength

To quantify the changes in connectivity strength during physiological IEDs in IS subjects, we performed statistical tests to compare an individual's ALL, EE, and NEE FCNs. Based on previous studies reporting an increase in functional connectivity during IEDs (Siniatchkin et al. 2007; Wilke et al. 2011; de Curtis et al. 2012; Clemens et al. 2016), we expected the EE FCNs to have the highest connectivity strength, followed by the ALL FCNs, followed by the NEE FCNs. We tested these comparisons for each IS subject using three one-tailed Wilcoxon sign-rank tests, where each test compared different FCN pairs: 1) EE > ALL, 2) ALL>NEE, and 3) EE>NEE. In each test, we compared the paired distributions of all connections to the null hypothesis that the median strengths were not statistically different.

3.3. Results

3.3.1 Amplitude and burden of the simulated IEDs

We defined the simulated IED waveform's amplitude and burden based on the spike to background amplitude ratio and the frequency of IEDs in IS subjects (see Chapter 2.2.3). Across all patients, our analysis included 1,340 visually marked IEDs and 5,360 measurements of background amplitude. The mean spike to background amplitude ratio across all eight IS subjects was 2.62 to 1, with a standard deviation of 0.38. To match the spike to background ratios seen in IS subjects, we scaled the simulated spike amplitude based on the average background amplitude across all controls (26.8±6.3 μV). In our simulations, we conservatively accounted for variance in the control subjects by using three standard deviations above the average of the control background amplitude (45.8 uV), multiplied by the spike:background ratio of 2.62, to generate 120 uV discharges. The spike burden for each subject was defined as the

number of marked focal IEDs divided by the total EEG recording time (Table 3.1). The highest burden across all eight IS subjects was approximately 25%, so we conservatively used this maximum spike burden for all simulations, unless otherwise specified.

Table 3.1 *Patient demographics and clinical data*

Diagnosis	*Subject*	*Sex*	*Age (mo.)*	*IED location (simulated)*	*No. of epileptiform epochs (simulated)*	*No. of non-epileptiform epochs (simulated)*	*EEG recording duration in sec.*
IS	1	F	12	O1	144	117	1206
	2	F	5.5	O1	118	166	1274
	3	F	4.5	F4	115	119	1346
	4	F	4.5	O1	219	126	1308
	5	F	7.9	O2	166	254	1273
	6	F	6.3	T5	246	249	1752
	7	M	21.1	O1	100	120	1335
	8	F	20.3	O2	231	196	1887
Controls	1	M	19	(F3)	(245)	(735)	980
	2	F	7	(F3)	(215)	(646)	861
	3	F	9	(F3)	(304)	(913)	1217
	4	F	5	(F3)	(285)	(858)	1143
	5	F	12	(F3)	(167)	(504)	671
	6	F	7	(F3)	(224)	(673)	897
	7	F	3	(F3)	(232)	(697)	929
	8	M	22	(F3)	(238)	(715)	953

3.3.2 Excessive spike amplitudes change FCN structure and increase connectivity strength

To determine the effect of the simulated IED's amplitude on a subject's FCN, we added simulated IEDs with varying spike:background amplitude ratios to control subject EEG and compared the EE and ALL FCNs to the CONTROL FCN. The addition of simulated spikes had a small but significant effect on both the network structure and mean connectivity strength in the ALL FCN (Figures 3.4A, 3.5A, 3.5B) (Wilcoxon rank sum test, $p<0.05$ pre-specified threshold FDR, corrected for multiple comparisons using the Bonferroni correction; pFDR = 0.00714). In contrast, we saw large changes in both the network structure and mean connectivity strength in the EE FCN (Figures 3.4B, 3.5C, 3.5D) (Wilcoxon rank sum test, $p<0.05$ pre-specified threshold

FDR, corrected for multiple comparisons using the Bonferroni correction; pFDR = 0.00714). Across all control subjects, we found a dramatic decrease in 2D correlation (indicating a change in network structure) and an increase in mean connection strength at spike:background ratios greater than 7, which is more than 2.5 times greater than the average spike:background ratio for IS subjects.

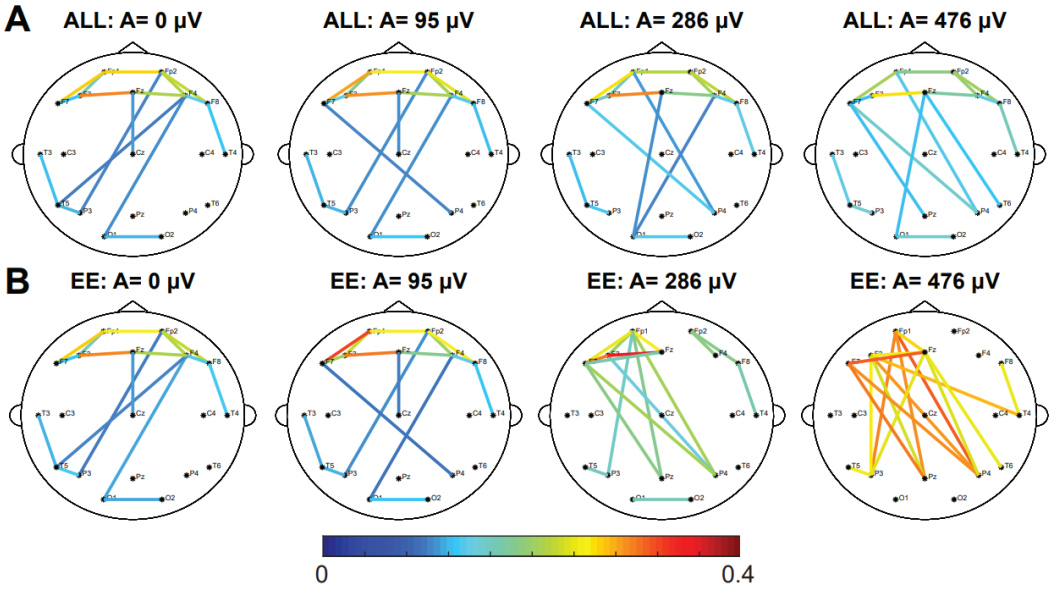

Figure 3.4. Increasing the amplitude of the IED has a small effect on the strength and structure of the ALL network and a large effect on the EE network. Representative example showing the effect of adding simulated focal IEDs at F3 with varying amplitudes on the (A) ALL FCN and the (B) EE FCN of control subject 6. The strongest 10% of connections are shown.

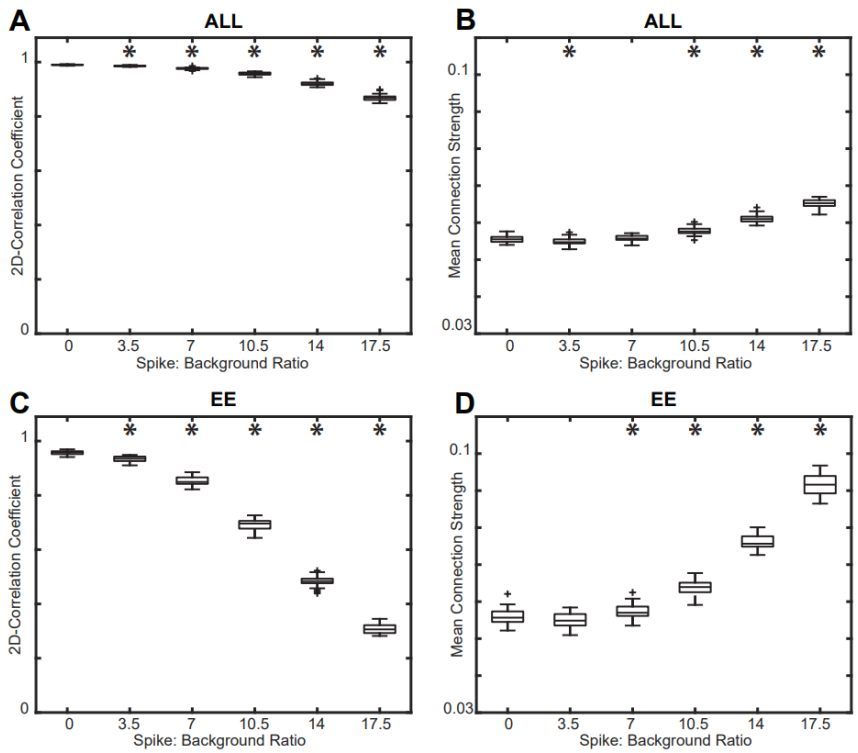

Figure 3.5. Effect of varying spike amplitude on the (A) 2D correlation and (B) mean connection strength of the ALL FCN compared to the CONTROL FCN. Effect of varying spike amplitude on the (C) 2D correlation and (D) mean connection strength of the EE FCN compared to the CONTROL FCN. The mean spike:background ratio for IS subjects was 2.62, and changes in network strength and structure occur well above this value. A representative example from control subject 6 is shown. Significance tests compared each result to the base CONTROL FCN (spike burden = 0%).

3.3.3 Increasing the spike burden has little effect on connectivity strength

Next, we investigated changes in the FCN as a function of spike burden. We inserted varying numbers of IEDs into the control subject EEG; specifically, we added them to 0%, 20%, 40%, 60%, 80%, and 100% of all one-second epochs and then calculated the FCN (Figure 3.6). We found that increasing the number of IEDs slightly decreased the ALL FCN's correlation to the CONTROL network from 0.990 to 0.949 (Figure 3.7A) and increased the mean connectivity strength from 0.0555 to 0.0575 (Figure 3.7B) (Wilcoxon rank sum, $p<0.05$ pre-specified threshold FDR, corrected for multiple comparisons using the Bonferroni correction; pFDR = 0.01). Although these differences in strength and structure were small, they were statistically

significant due to the low variance across simulations (Figure 3.7). These results were consistent across all control subjects.

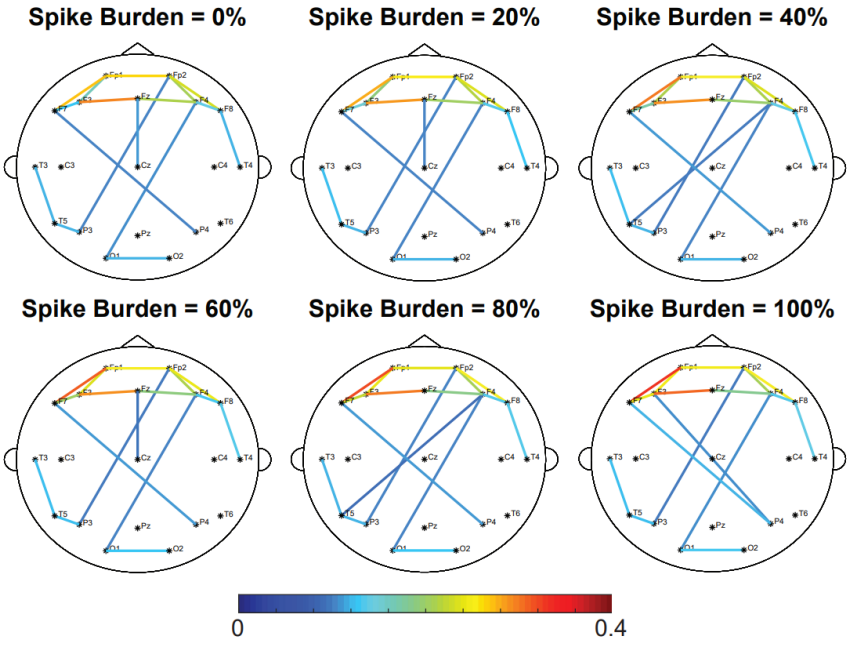

Figure 3.6. Increasing the spike burden does not affect the network strength and structure of the ALL network. Representative example of the effect of spike burden on the ALL FCN of control subject 6. Simulated focal IEDs are added at electrode F3. The strongest 10% of connections are shown.

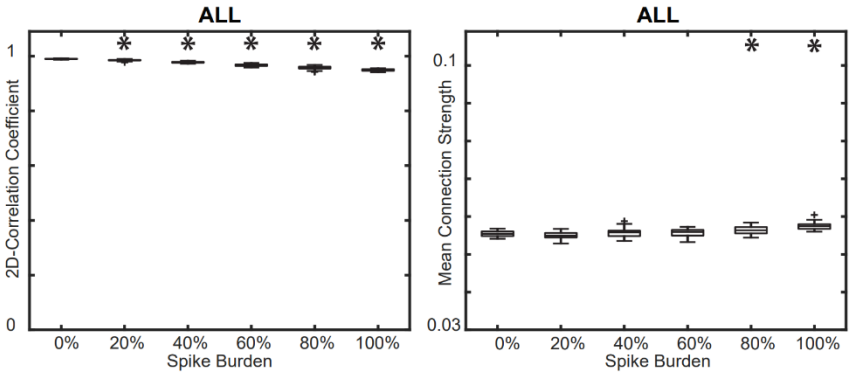

Figure 3.7. (A) Effect of spike burden on the 2D correlation between the ALL FCN and CONTROL FCN. (B) Effect of spike burden on the mean connection strength in the ALL FCN. Results for all control subjects were similar; a representative example from control subject 6 is shown. Significance tests compared each result to the base CONTROL FCN (spike burden = 0%).

3.3.4 FCN structure for IS subjects is subject-specific

We then quantified the differences in the network structure of individual IS and control subjects. This was done by calculating the 2D correlation of the connectivity matrices between all pairs of subjects in the following within-group or across-group comparisons: (1) control-control, (2) IS-control, and (3) IS-IS. Figure 3.8 shows the correlation coefficients and statistical comparisons for these three categories (Wilcoxon rank sum, $p<0.05$ pre-specified threshold FDR, corrected for multiple comparisons using the Bonferroni correction; pFDR = 0.0167). Control-control correlation coefficients were significantly higher than those for the IS-control ($p = 1.163e-7$) and IS-IS comparisons ($p = 1.064e-4$). We found no significant differences in correlation between IS-IS and IS-control ($p = 0.6196$). These results suggest that the FCNs of control subjects are more stereotyped and exhibit less variability than the FCNs of IS subjects. Our findings also demonstrate that the FCNs of individual IS subjects are no more similar to other IS subjects than they are to control subjects.

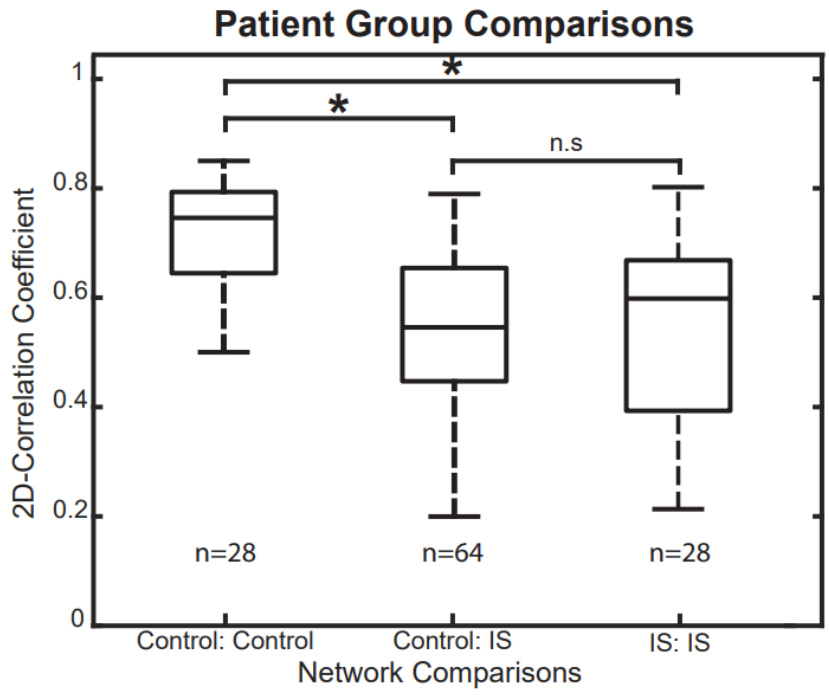

Figure 3.8. Rank-sum tests for 2D correlation coefficients across different subject groups. The correlation coefficients in control-control comparisons were significantly higher than in control-IS

and IS-IS comparisons, indicating that control subjects have more consistent, stereotyped FCNs.

3.3.5 FCN structure does not change during interictal spikes

In both IS and control subjects, changes in network structure associated with the presence of IEDs were assessed using the rGED and 2D correlation, two complementary techniques that yielded similar results. We compared all three pairs of FCNs within an individual subject: (1) ALL compared to NEE, (2) ALL compared to EE, and (3) EE compared to NEE. To gain perspective on the degree of similarity between these networks, we compared these values to a null model consisting of network comparisons across different subjects within the same cohort. For example, to test the ALL vs. NEE FCNs of Subject 1, we calculated the rGED and 2D correlation of Subject 1's ALL to Subject 1's NEE FCN. These values were then compared to a null model consisting of rGED and 2D correlation values of Subject 1's ALL vs. Subject 2's NEE, Subject 1 ALL vs. Subject 3 NEE etc. plus the analogous correlations between Subject 1's NEE to the ALL from all other subjects. If the intra-subject FCN correlations were higher than the inter-subject FCN correlations, this indicated that the presence of IEDs did not significantly alter the subject's FCN.

For all eight IS subjects, the intra-subject rGED values for the ALL vs. NEE and ALL vs. EE network comparison tests were significantly higher than the inter-subject values (Figure 3.9A) (one sample Wilcoxon signed rank test, $p<0.05$ pre-specified threshold FDR, corrected for multiple comparisons using the Bonferroni correction; pFDR = .00625). In the EE vs. NEE network test, seven out of eight epilepsy subjects had significant rGED values. This demonstrates that the ALL, EE, and NEE FCNs are subject-specific and that the strongest connections are not significantly affected by the presence of IEDs. In control subjects with simulated IEDs, we found significantly higher intra-subject rGEDs compared to inter-subject rGEDs across the control subjects in all network comparisons across 200 different iterations of

simulated IEDs, (Wilcoxon rank sum, n= 8, p<0.05 pre-specified threshold FDR, corrected for multiple comparisons using the Bonferroni correction; pFDR = 0.00625) (Figure 3.9B).

The analogous calculation using 2D correlation yielded similar results (Figure 3.10). These results were significant for all three network comparisons across all eight IS subjects (one sample Wilcoxon signed rank test, p<0.05 pre-specified threshold FDR, corrected for multiple comparisons using the Bonferroni correction; pFDR = .00625) and all eight control subjects (Wilcoxon rank sum, n= 8, p<0.05 pre-specified threshold FDR, corrected for multiple comparisons using the Bonferroni correction; pFDR = 0.00625). This test complements the rGED analysis, as the 2D correlation calculation utilizes all connection pairs and does not require thresholding to create a binary network.

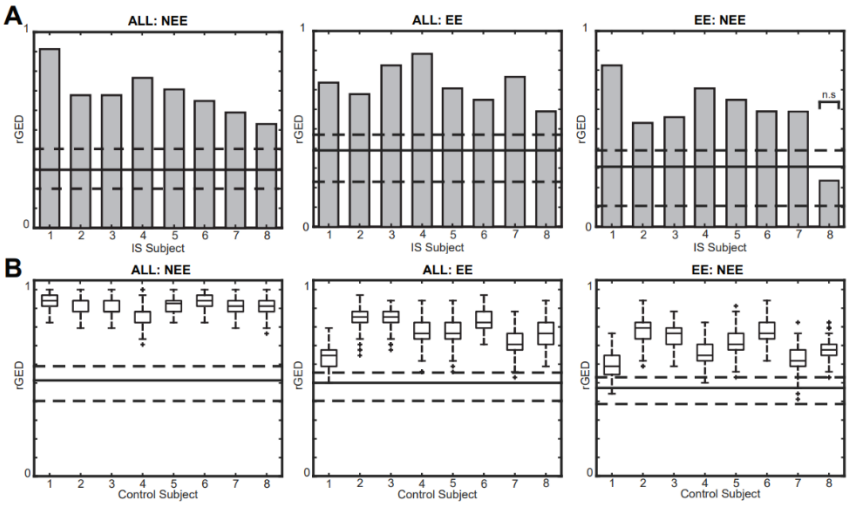

Figure 3.9. Relative graph edit distance (rGED) values for intra-subject network comparisons are significantly higher than inter-subject comparisons in (A) IS subjects and (B) control subjects with simulated IEDs. Gray bars represent intra-subject comparisons for IS subjects, and box plots represent intra-subject values from 200 simulations in controls. The solid lines represent the median of the intersubject rGED values and the dashed lines represent the 25th and 75th percentiles. All tests are significant except EE:NEE in IS subject 8.

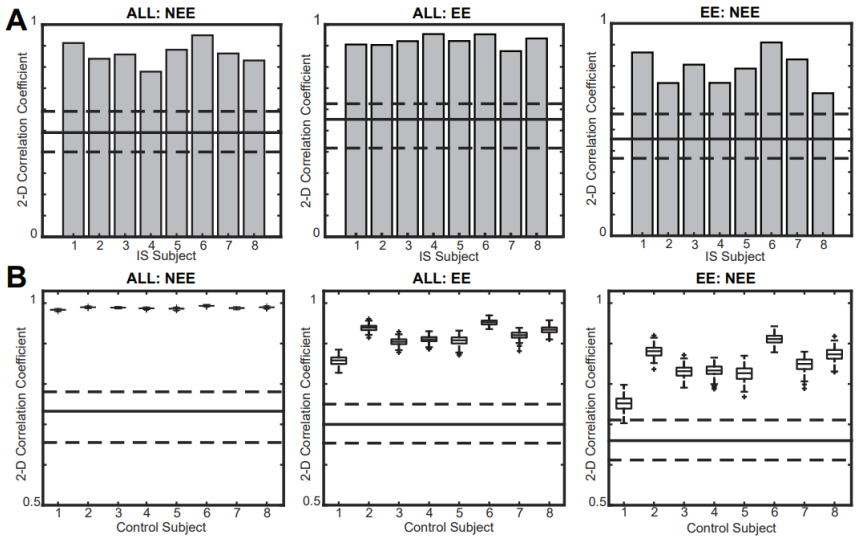

Figure 3.10. 2D correlation coefficients for all intra-subject network comparisons are significantly higher than inter-subject comparisons in (A) IS subjects and (B) controls. Gray bars represent intra-subject comparisons for IS subjects, and box plots represent intra-subject values from 200 simulations in controls. The solid line represents the median of the inter-subject correlation values and the dashed lines represent the 25th and 75th percentiles.

3.3.6 Connectivity strength increases during IEDs in epilepsy subjects

Changes in connectivity strength in the presence and absence of an IED for each subject was done using three one-tailed Wilcoxon sign-rank tests. We tested the paired distributions of all 171 connectivity strengths for the following FCN comparisons within each subject: (1) EE > ALL, (2) ALL > NEE, and (3) EE>NEE. These comparisons were based on the simulated data in Figures 3.4, 3.5B, and 3.5D, which suggested that the EE network would have the highest connectivity strength, followed by the ALL network and then the NEE network. For all three network comparisons, this hypothesis held true for seven out of eight IS subjects (Table 3.2). In contrast, the sign-rank test yielded no significant differences in connectivity strength for any of the three network comparisons for the control subjects. The p-values for control subjects were equivalent across simulations with randomly placed IEDs, indicating that the specific timing of the IEDs did not affect the results.

Table 3.2 *P-values for statistical comparisons of connectivity strength between FCNs in individual subjects. The p-values from control subjects come from 200 simulations with spikes inserted at random times in the EEG record.*

		FCN comparison		
Cohort	*Subject*	*EE>ALL*	*ALL>NEE*	*EE>NEE*
IS	1	**0**	0.221	**0**
	2	**0**	**0.001**	**0**
	3	0.853	**0.037**	1
	4	**0**	**0.004**	**0**
	5	**0**	**0.001**	**0.017**
	6	**0**	**0**	**0.020**
	7	**0**	**0.021**	**0.006**
	8	**0**	**0**	**0**
Controls	1	0.9590 ±0	0.9317 ±0	0.9951 ±0
	2	0.6156 ±0	0.0255 ±0	0.2771 ±0
	3	0.8938 ±0	0.9696 ±0	0.9782 ±0
	4	0.6366 ±0	0.3542 ±0	0.6889 ±0
	5	0.3525 ±0	0.9989 ±0	0.8491 ±0
	6	0.4402 ±0	0.2009 ±0	0.3651 ±0
	7	0.3827 ±0	0.6515 ±0	0.6954 ±0
	8	0.4520 ±0	0.2043 ±0	0.3104 ±0

3.4. Discussion

In this study, we investigated how the presence of IEDs impacts EEG-based FCNs. IS subjects have unique, patient-specific FCNs, while control subjects have more stereotyped network structures. In IS subjects, physiological IEDs do not significantly alter FCN structure, consistent with simulated IEDs in control subjects, which only alter FCN structure when the amplitude or spike burden are outside of normal physiological ranges. On the other hand, functional connectivity strength significantly increases during the occurrence of physiological IEDs in IS subjects, whereas the addition of simulated IEDs to normal EEG does not increase the connectivity strength. We conclude that these changes in connectivity strength in IS subjects are not spurious increases caused by the presence of the interictal spike waveform in the EEG. Overall, these findings suggest that an individual's FCN structure remains stable during an IED, and that the changes in connectivity strength noted in epileptic subjects are likely due to the underlying pathophysiological networks of the disease, rather than simply the presence of the IED waveform itself. Furthermore, our analysis suggests that there is no need to mark and

remove IEDs prior to calculating an FCN, as the functional connectivity measurements derived from EEG epochs containing IEDs do not differ significantly from those of interictal EEG epochs.

In control subjects with simulated IEDs, the amplitude of the IED affected FCN structure more than the spike burden did. Introducing simulated IEDs with high spike:background amplitude ratios caused major alterations to the FCN structure, indicated by a decrease in 2D correlation from 1.0 to nearly zero (Figure 3.5C). In comparison, high spike burdens of 100% led to a decrease in 2D correlation from 1.0 to 0.8, indicating that the increase in burden caused little change in the network structure (Figure 3.8).

Introducing simulated IEDs with physiological spike amplitudes and burdens derived from the EEG of IS subjects did not cause a substantial change in FCN structure. Across all focal IEDs detected in IS subjects, the average spike:background ratio was 2.62, while changes in the control subjects' EE network structure emerged at a simulated spike:background ratio greater than 7. The consistency of network structure in IS subjects is shown in Figures 3.9 and 3.10, where the rGED and 2D correlations of intra-subject FCN comparisons are significantly higher than inter-subject comparisons. Increasing the spike burden also had minimal effect, resulting in a change of less than 5% in both 2D correlation and mean connectivity strength (Figure 3.7). Simulated IEDs with excessive amplitudes and burdens were included in our analysis to test the potential of the simulated IED to alter the FCNs. IEDs exceeding 300 uV have been reported (Janati et al. 2018), although this did not frequently occur in our dataset.

In addition to assessing the impact of IED amplitude and burden on FCNs, we investigated the effect of simulated IED location on the FCN of control subjects. Varying the location of focal IEDs produced similar effects as placing the focal spikes at F3, with minimal change noted in the FCN structure at low amplitudes. Increasing the simulated IED amplitudes past the physiological range resulted in increased connectivity strength and an altered FCN structure with long-range connections involving the IED focus, similar to Figure 3.4B. Overall,

this result confirmed that IED location was not a crucial factor in our tests of IED amplitude and burden.

The shape of the IED waveform could also impact our results. Our simulated IED was modeled after the typical spike-wave complex associated with many types of epilepsy. However, there are many types of IED waveforms to consider, including isolated spikes (without a slow wave component), polyspikes with and without slow wave components, and paroxysmal fast activity (de Curtis et al. 2012). Here, we chose an IED waveform containing both a spike and a slow wave, as this had the greatest potential to affect the connectivity calculation. We also chose to include the slow wave in our simulation because the slow wave can drive changes in broadband EEG connectivity, and it has also been linked to hypsarrhythmia in IS subjects (Hrachovy and Frost 2003; Frost and Hrachovy 2005).

Prior to subject-specific FCN tests, we compared the FCN differences between the IS and control cohorts. Across all groupwise comparisons, we found that the median 2D correlation of control-control FCNs was approximately 0.75, while the median 2D correlation of control-IS and IS-IS comparisons was approximately 0.5 and 0.6, respectively (Figure 3.8). The significantly lower values for the control-IS comparison are in accordance with prior studies using EEG-based FCN, with reported differences in the global network characteristics of temporal lobe epilepsy and focal epilepsies compared to the healthy brain (Horstmann et al. 2010; Kramer and Cash 2012; Quraan et al. 2013). The low 2D correlation in IS-IS comparisons was likely due to the multifocal nature and the wide range of etiologies in IS, resulting in a unique network structure for each subject. Similar results were reported for EEG-based FCNs associated with absence seizures, where across patient correlations were lower than within patient comparisons (Taylor et al. 2013). We report a median 2D correlation between control subject FCNs of 0.75, higher than a previous study reporting cross-correlation values between healthy adult controls of approximately 0.5 (Chu-Shore et al. 2012). These differences in correlation could reflect a difference between the infant brain, as studied here, and the adult

brain. Moreover, the correlation coefficient of 0.75 for control-control comparisons does not suggest an identical FCN structure across patients, but rather indicates that control subjects are more likely to exhibit stereotyped connectivity patterns than IS subjects.

Differences in the sleep structure of healthy controls and IS subjects may be a factor in the comparison of their FCNs (Figure 3.8). To mitigate the effects of sleep stage on FCNs, non-REM sleep was analyzed in all subjects. In a related study, we found no significant differences in functional connectivity for different non-REM sleep stages in the long-term EEG of both controls and IS subjects (unpublished data). However, disruption of the sleep architecture in IS subjects may have contributed to the wider network variance in that group.

Generally, the occurrence of IEDs in IS subjects was associated with a global increase in connection strength without changes in network structure. This change in connectivity could reflect activation of a pathological network associated with seizures, or it could be related to the disruption of cognition caused by the occurrence of frequent spikes (Ebus et al. 2012; Ung H et al. 2017). FCNs of epochs containing interictal spikes had the highest connectivity strength, followed by FCNs generated using all epochs, followed by FCNs lacking interictal spikes. These relationships are in agreement with previous studies, where the presence of interictal spikes resulted in increased connectivity strength in the medial temporal pole, hippocampus, amygdala, parahippocampal gyrus, olfactory gyrus, and gyrus rectus regions compared to baseline periods without spikes (Wilke et al. 2011; Coito et al. 2015). Of the eight IS subjects, seven had ALL, EE, and NEE FCN structures that were more similar to each other than they were to other subjects. For IS subject 8, the ALL and EE FCNs consisted of long-range connections emanating from the location of the IEDs, with higher connectivity strengths than all other epilepsy subjects. This is similar to the EE FCNs of controls with very high amplitude IEDs (Figure 3.4B). The rGED of the EE:NEE comparison for IS subject 8 was 0.24, compared to the other IS subjects who have rGED values of approximately 0.6 (Figure 3.9A). This low rGED value suggests a significant change in network structure during IEDs. Although IS subject 8 did

not have a significantly larger spike:background amplitude ratio than the other IS subjects, they did have spike-wave discharges with significantly larger slow wave amplitudes than other IS subjects, which may explain this discordant finding. This could explain the similarity between this IS subject and the control subject simulations at high amplitudes, suggesting that the slow wave's waveform is causing the changes in the measurement of FCN structure.

There are limitations to the methods presented here. We analyzed standard clinical EEG recordings with nineteen scalp electrodes to promote broad applicability to any clinical epilepsy center, as opposed to other studies that utilized high-density research EEG recordings (Coito et al. 2015, 2016; Mahmoudzadeh et al. 2016). Although our results were consistent with those from prior studies, the use of high-density electrode arrays would allow the use of additional graph theory metrics, whose accuracy depends on having a network with many nodes. In addition, our study is limited by a small sample size of sixteen subjects. Future studies can increase the cohort size for healthy controls, IS subjects, and non-IS epilepsy subjects to further test the validity and robustness of our findings. Other limitations of our study lie in the assumptions inherent to simulating IEDs. We used boundary element methods modelled on a template brain volume from the ICBM 152 atlas, which is based on young adults rather than infants. The properties of the simulated IED waveform were chosen to match that of a spike-wave complex, which does not reflect all IED types. Additionally, the model only simulated IEDs at a single location, which is simpler than the multifocal nature of IEDs in IS.

While our methods address the effects of volume conduction, the use of a bivariate connectivity measure may introduce spurious connections into the FCNs. These spurious connections can be attributed to one source that drives activity in multiple channels, resulting in significant connectivity from the source to the secondary channels, as well as false connectivity between all secondary channels (Blinowska and Kaminski 2013). The results in the present study should be minimally impacted by such spurious connections because most were based on comparative measures between FCNs, but the specific effect will vary based on the type of

comparison. In within-subject comparisons (Figures 3.4-3.7), where we compared FCNs for a single subject as spike parameters were varied, the spurious connections caused by a common source should be the same across all comparisons and will therefore have very little impact on the results. In within-group comparisons (Figures 3.9 and 3.10; Figure 3.8, boxplots for Control:Control and IS:IS), comparisons between FCNs within the control group and comparisons between FCNs within the IS group may be affected by differing spurious connections in individual subjects. However, our results suggest that this effect will be insignificant because the FCNs in each group are biased similarly. This is shown in Figure 3.8, where the FCNs of control subjects are highly correlated with one another. In the cross-group comparison (Figure 3.8, Control:IS), the presence of spurious connections could have a significant impact due to the variance across subjects from different groups. Future studies that focus on FCN comparisons can minimize this problem by utilizing multivariate connectivity measures. Multivariate measures can also accurately quantify directional relationships between brain regions (Blinowska 2011).

In future work, we plan to validate our findings by increasing the cohort size to include more subjects, including adults and older children, with both generalized and focal epilepsies. Due to the heterogeneous IEDs contained in IS subjects, we also plan to study different aspects of the spike-wave complex such as the effects of slow wave amplitude rather than the spike amplitude alone. Lastly, we plan to analyze the impact of different IED waveforms and the presence of multi-focal IEDs on functional networks. This work will elucidate the dynamic changes in functional connectivity and the robustness of FCNs in the presence of transient waveforms occurring over long spans of time.

CHAPTER IV

Interrater Reliability of Interictal EEG Waveforms in Lennox-Gastaut Syndrome

4.1 Introduction

Lennox-Gastaut Syndrome (LGS) is a severe, childhood-onset epileptic encephalopathy that often evolves from earlier epilepsies such as infantile epileptic spasms syndrome (IESS). LGS is characterized by: (1) the presence of multiple seizure types, (2) cognitive impairment, and (3) the presence of interictal epileptiform activity in the electroencephalogram (EEG), such as slow spike-wave (<2.5 Hz) and generalized paroxysmal fast activity (GPFA), a unique waveform that is primarily seen in LGS during NREM sleep (Mastrangelo 2017a). In addition to their importance for diagnosis, these waveforms can also be biomarkers of treatment response in LGS. For example, the decrease in GPFA burden has been associated with similar reductions in diary-recorded seizures (Dalic et al. 2022b), and continuous spike and wave pattern during slow wave sleep has been associated with neurodevelopmental disabilities (Baumer et al. 2021). Identifying interictal epileptiform activity can also help classify the type of epilepsy and help clinicians manage anticonvulsants (Smith 2005).

The prompt diagnosis of LGS is critical for seizure control and maximizing long-term neurocognitive outcomes (Camfield et al. 2011; Piña-Garza et al. 2017; Berg, Anne; Levy and Testa 2018). However, because the onset of LGS is often insidious, it can be difficult to define a single timepoint at which LGS begins. Experts may disagree as to whether EEG abnormalities are sufficiently severe to substantiate a diagnosis of LGS, which may delay diagnosis and effective treatment. Interpretation of individual EEG waveforms is inherent to this decision and low interrater reliability could be a significant contributing factor. The reliability of identifying interictal epileptiform discharges has been shown to be limited, as individual experts apply

different thresholds in their decisions to mark events (Jing et al. 2020). A consensus has also not yet been reached on the defining characteristics of GPFA, as studies using visually marked events report different values of GPFA amplitude, duration, and frequency across subjects (Mohammadi et al. 2015; Bansal et al. 2019). One group developed an automated detector that defined GPFA as a low frequency (0.3-3 Hz) component plus a high frequency (8-20 Hz) component; in comparison to manually marked GPFA, the detector was found to return a high number of false positive detections (Omidvarnia et al. 2021). This further highlights a lack of characterization of the specific waveform features used in the visual analysis of LGS EEG, which is a barrier to developing objective biomarkers of LGS. Given these uncertainties, the goal of this study was to evaluate the rater accuracy and interrater reliability (IRR) of EEG events in both healthy controls and patients with LGS.

4.2 Methods

4.2.1 Subject information

Approval for this retrospective study was obtained from the Institutional Review Boards at Children's Hospital of Orange County (CHOC) and the University of California Los Angeles (UCLA), with the requirement for informed consent waived. Twenty subjects diagnosed with LGS (7 females, median age 7.4 years, age range 1.0-18.8 years) were retrospectively identified using ICD 9 and 10 diagnostic codes from the clinical record at CHOC, with visits and EEG studies performed between January 2012 and June 2020. Their electroclinical diagnosis of LGS was confirmed by a board-certified pediatric epileptologist Twenty healthy control subjects (8 females, median age 8.2 years, age range 1.0-17.7 years) were selected from a cohort of fifty subjects collected in a prior study. The twenty healthy subjects were selected such that they were approximately age-matched to the LGS group. The cohort of fifty control subjects was retrospectively identified from the clinical record at UCLA with visits between February 2014 and July 2018 (Smith et al. 2021b). Controls were included if they had (1) no known neurological

disorders, (2) routine EEG studies that were interpreted as normal by a board-certified pediatric epileptologist, and (3) no use of neuroactive medications. There were no significant differences in age between control and LGS subjects ($p = 0.672$, Student's t-test); the breakdown by sex was approximately the same between both groups.

4.2.2 EEG acquisition and preprocessing

All EEG data were recorded using the Nihon Kohden EEG acquisition system, with nineteen scalp electrodes (Fp1, Fp2, F3, F4, C3, C4, P3, P4, O1, O2, F7, F8, T3, T4, T5, T6, Fz, Cz, Pz) placed according to the international 10-20 system at a sampling rate of 200 Hz. For each EEG recording, epochs of non-REM sleep lasting approximately 20-30 minutes containing minimal arousals and artifacts were selected by a pediatric epileptologist. Time points containing high-amplitude artifacts were identified using an automated detector as in prior studies (Smith et al. 2021b; Hu et al. 2022). For each subject, one 10-minute segment of clean, continuous, NREM sleep EEG with no automated or clinically detected artifacts was selected for analysis. All EEG data were re-referenced to the common average and filtered with a zero-phase shift digital filter from 0.5-55 Hz. All electronic data were deidentified and analyzed offline using custom MATLAB (Mathworks) scripts.

4.2.3 Identifying EEG events

The EEG data were first pre-whitened in the time-domain using first-order backward differencing to counteract the expected 1/f decrease in power (Usui and Amidror 1982; Gardner et al. 2007a; Roehri et al. 2016). The time-varying power spectrum of the EEG for frequencies from 1 to 50 Hz was subsequently obtained using the Stockwell transform (Stockwell et al. 1996), in increments of 1 Hz.

We then identified regions of high power in the time-varying power spectrum that exceeded a threshold of $250\frac{\mu V^2}{Hz}$, which corresponded to a z-score of 1.69 for the EEG power and resulted in selection of 4.6% of all time-frequency values. This relatively low value for the threshold was chosen to ensure that all events of interest, particularly epileptiform activity, would be captured. This fixed threshold was used across all frequency bands and subjects, as the pre-whitening step served to normalize the power across frequency bands and between LGS and control subjects.

For each subject, we defined an "event" to be a region of high power in the time-varying power spectrum that is continuous in time (Figure 4.1). Specifically, a single event consisted of consecutive time points in which the power for at least one frequency exceeded the threshold, with a minimum duration of 100 milliseconds. This minimum length was chosen to fully capture the duration of an epileptic spike, the shortest abnormal event we expected to see. Note that such sharp waveforms often appear smeared (with longer duration) in the time-varying power spectrum, particularly at low frequencies. Events were identified in the EEG data from the Fz electrode, as the fronto-central location should be minimally impacted by eye movements and muscle artifact and maximally sensitive to events such as sleep spindles and GPFAs (Bansal et al. 2019).

4.2.4 Time-frequency image features for each event

For each event, we calculated six features using the time-varying power spectrum. We first defined the time-varying power spectrum as $X_{t,f,e}$ where t is time, f is frequency, and e is the electrode at which the EEG was measured (Figure 4.1B). We then defined the time-frequency image (TFI) of a single event to be the set of ordered doublets whose power in an electrode e exceeded the threshold T:

$$TFI_e = \{(t,f) \mid X_{t,f,e} > T\} \qquad (4.1)$$

Two examples of events and their associated TFIs are shown in Figure 4.1C. Given these definitions, the six features were as follows:

1. **Height** (Figure 4.2A): The height was defined by the highest frequency minus the lowest frequency in the TFI for electrode Fz:

$$Height = max_f(\{TFI_{Fz}\}) - min_f(\{TFI_{Fz}\}) + 1 \qquad (4.2)$$

   The height ranged from 1 to 50 Hz, as the frequencies ranged from 1 Hz to 50 Hz.

2. **Duration** (Figure 4.2B): The duration corresponded to the event length in seconds in electrode Fz and was defined by:

$$Duration = max_t(\{TFI_{Fz}\}) - min_t(\{TFI_{Fz}\}) \qquad (4.3)$$

3. **Spread** (Figure 4.2C,D): The spread measured how many other electrodes had events that overlapped the Fz TFI in time and frequency. A spread of 1/19 = 0.05 indicated that no other scalp electrodes exhibited high EEG power (exceeding the threshold) at the same time and frequency as the Fz electrode, and a spread of 1 indicated that all other electrodes exhibited high EEG power at the same time-frequency points as the Fz electrode. The spread was defined by:

$$Spread = \frac{\sum_{e=1}^{nElec} |\{TFI_{Fz} \cap TFI_e\}|}{nElec * |\{TFI_{Fz}\}|} \qquad (4.4)$$

   Where $|\{TFI_{Fz} \cap TFI_e\}|$ is the cardinality of the intersection between TFI sets for Fz and electrode e, $nElec$ is the total number of EEG electrodes, and $|\{TFI_{Fz}\}|$ is the cardinality of the TFI in Fz.

4. **Density** (Figure 4.2E): The density was the area of the event in time-frequency space, normalized by the event duration and the maximum possible height (here 50 Hz). A density of 1/50 = 0.02 indicated that the event had high power at a single frequency at each time point, and a density of 1 indicated that all possible frequencies exceeded the power threshold at all time points. The density was defined by:

$$Density = \frac{|\{TFI_{Fz}\}|}{nFreq * Duration * fs} \qquad (4.5)$$

Where $nFreq$ is the number of frequencies analyzed and fs is the sampling rate.

5. **Mean Power** (MP, Figure 4.2F): The mean power was calculated across all time-frequency points in the Fz electrode event that exceeded the threshold:

$$MP = \frac{\sum_{(t,f)\in TFI_{Fz}} X_{t,f,Fz}}{|\{TFI_{Fz}\}|} \qquad (4.6)$$

Where (t, f) consists of all ordered doublets within TFI_{Fz}.

6. **Frequency of Peak Power** (FPP, Figure 4.2G): The FPP was the frequency at which the event had the maximum power:

$$FPP = argmax_f(X_{t,f,Fz}) \qquad (4.7)$$

The FPP ranged from 1 to 50 Hz, based on the frequency range included in the time-varying power spectrum.

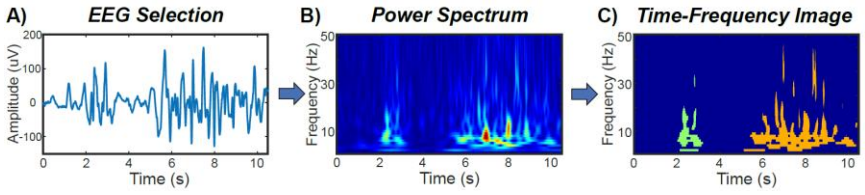

Figure 4.1 A representative example of event identification. Ten minutes of artifact-free EEG were selected from each subject; a sample of ten seconds is shown here. (A) After selection, the EEG for each channel was pre-whitened. (B) The time-varying power spectrum was calculated for the entire EEG clip. (C) Events were identified as consecutive time points in which the EEG power exceeded a threshold. For a single event, the set of points in the time-frequency space that exceeded the threshold was defined as the time frequency image (TFI). Here, two different TFIs are shown, one in green and one in orange.

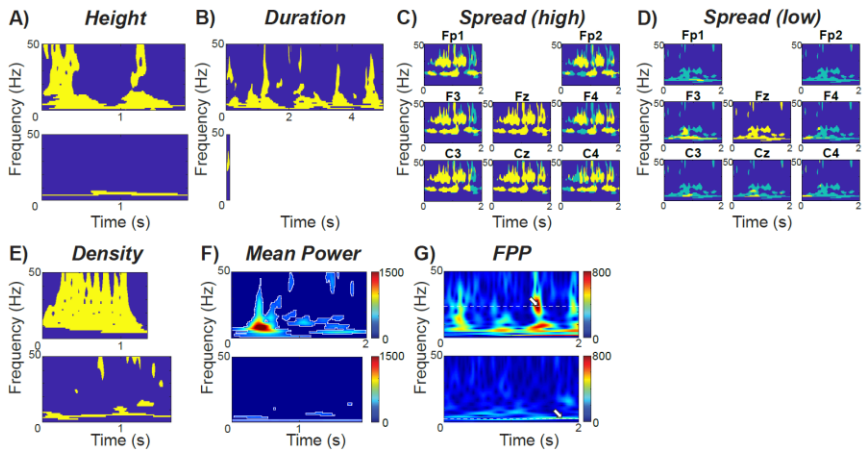

Figure 4.2 Examples of TFIs and time-varying power spectrum features: (A) height, (B) duration, (C) high spread, (D) low spread, (E) density, (F) mean power, and (G) frequency of peak power. For all features except spread, an example of a high value is shown at the top of the subfigure, and an example of a low value is shown at the bottom. The spread is visually represented using electrodes adjacent to Fz, with high and low spread shown in separate subfigures. Yellow regions indicate where the Fz TFI overlaps with the TFIs in adjacent electrodes, while light blue regions indicate where the Fz TFI does not overlap with the TFIs in adjacent electrodes.

4.2.5 Clustering analysis

Prior to clustering, each feature was normalized by converting the values to a z-score based on the mean and standard deviation of each feature across all control and LGS events. Control and LGS events were collectively partitioned into twelve different clusters using K-means (Lloyd 1982). Each event was treated as a single observation; each observation consisted of six variables, which were the z-scores of the features: height, duration, spread, density, MP, and FPP. A large number of clusters was used to ensure that all combinations of TFI features were represented, thus resulting in a broad distribution of events for visual analysis. For organizational purposes, the clusters were named in descending order based the sum of the six TFI feature z-scores, such that cluster one had the highest sum of the six TFI feature z-scores, and cluster twelve had the lowest sum.

4.2.6 Visual analysis of events

To ensure the selection of a representative distribution of events for visual classification, 120 events were randomly selected from each cluster (60 from LGS patients and 60 from control subjects). If a cluster contained fewer than sixty control or LGS events, the remaining events were selected from the other cohort. Cluster one consisted of only 30 events, and all events were included for this cluster. In total, 1,350 out of 11,708 events were selected for visual analysis. Three board-certified pediatric epileptologists (DA, DS, SH) from two different institutions (CHOC and UCLA) each classified 900 of the 1,350 events, so each event was independently classified by two different raters. The order of events was randomized. For each event, raters were given a fifteen-second clip of EEG, starting two seconds prior to the event and ending thirteen seconds after the event began, with a red line indicating when the event started and ended (Figure 4.3). Raters were blinded to the subject type, subject number, and the time at which the EEG clip was recorded. For each event, raters were asked to determine (1) the subject type, which could be either a control or LGS subject, and (2) the event type, which could be spike and slow wave (SSW), GPFA, seizure, sleep spindle, vertex sharp, muscle, artifact, other event, or no event. Events were viewed and classified using a custom GUI that was designed using MATLAB in consultation with the clinical team.

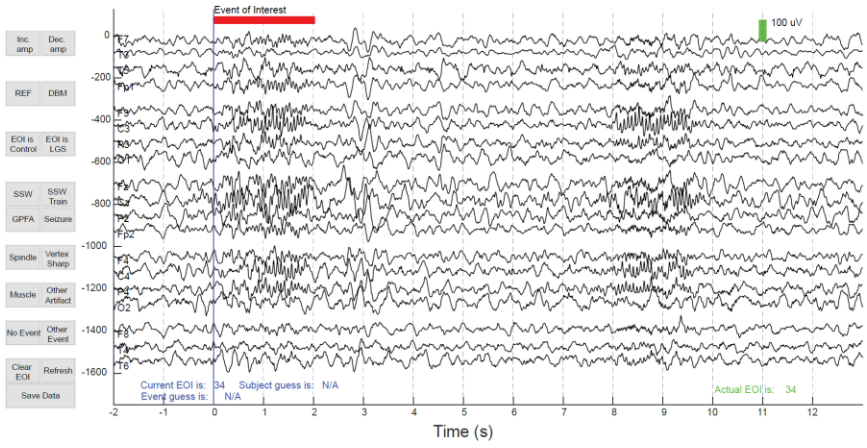

Figure 4.3 An example of the blinded visual analysis of an EEG event. The event is indicated by the horizontal red line. For each event, the rater selected a subject type and an event type. The user interface also included the option to change the EEG amplitude and referencing montage.

4.2.7 Statistical analysis

The IRR reflects the proportion of consistent ratings between clinicians that are not accounted for by chance. IRR was calculated for both subject and event classification and was assessed using the Cohen's Kappa (McHugh 2012) and intraclass correlation coefficient (ICC) (McGraw and Wong 1996). Cohen's Kappa ranges from negative one to one, with -1.00-0.00 = 'no agreement'; 0.01-0.20 = 'slight'; 0.21-0.40 = 'fair'; 0.41-0.60 = 'moderate'; 0.61-0.80 = 'substantial'; and 0.81-1.00 = 'almost perfect or perfect' IRR (Hallgren 2012). The ICC was calculated using a 2-way mixed-effects model, where an ICC greater than 0.7 is generally considered adequate and an ICC greater than 0.9 is considered excellent. The consistency in subject labels and event labels between raters was measured using the event agreement rate (EAR) (Nariai et al. 2018):

$$EAR = \frac{|\{A \cap B\}|}{|\{A \cup B\}|} \qquad (4.8)$$

Where A represents the set of events labeled with a specific subject or event type by reviewer A, and B represents the set of events of the same subject or event type labeled by reviewer B.

For the subject type, we also determined the accuracy of the visual classification relative to the ground truth of whether the subject had been diagnosed with LGS or not. The accuracy of the subject type labels was calculated as a percentage based on the subject type from which each EEG event originated.

4.3. Results

4.3.1 Automated event detection identified a broad range of events from all subjects

A total of 11,708 events were detected using the process described in Section 2.3, with 6,744 events coming from the twenty control subjects ($n_{controls}$ = 365.0 [259.0-443.0] events per subject; reported as the median [Q1-Q3] for all results) and 4,964 events coming from the twenty LGS subjects (n_{LGS} = 232.5 [156.0-324.5]). The minimum number of events for a single

subject was 49 and the maximum number of events was 560. There were no clusters composed of events from a single subject; on average, each subject contributed events to 8.5 different clusters (Figure 4.5). Each cluster was characterized by a different combination of the six features (Figure 4.6). For example, the events in cluster one had a long duration and high spread, while events in cluster two had high density and high mean power. Some clusters had low values of all features; this was expected, as events were identified using a relatively low power threshold to maximize the sensitivity of initial detection. The broad distribution of events across subjects and clusters and the unique characterization of each cluster based on the six features suggests that our algorithm was successful in identifying a broad range of events that were well-represented in both LGS and control subjects. Clustering events using a power threshold of 200 (7.7% of the data) and 300 (3.0% of the data) produced qualitatively similar clusters (Figure 4.4).

Figure 4.4. Event detection thresholds of (A) 200, (B) 250, and (C) 300 yielded similar cluster centroids with similar ratios of control to LGS events. For each cluster, the mean and standard deviation of the z-score for each feature is shown above, while the percentages of control and LGS events are shown below. The opacity of the green cells indicates the value of the z-score features, with low values appearing white; similarly, the opacity of the blue cells indicates the relative number of control and LGS events. Clusters using a threshold of 250 are sorted in descending order based on the sum of the z-scores; clusters using a threshold of 200 and 300 are sorted to best match the clusters with a threshold of 250.

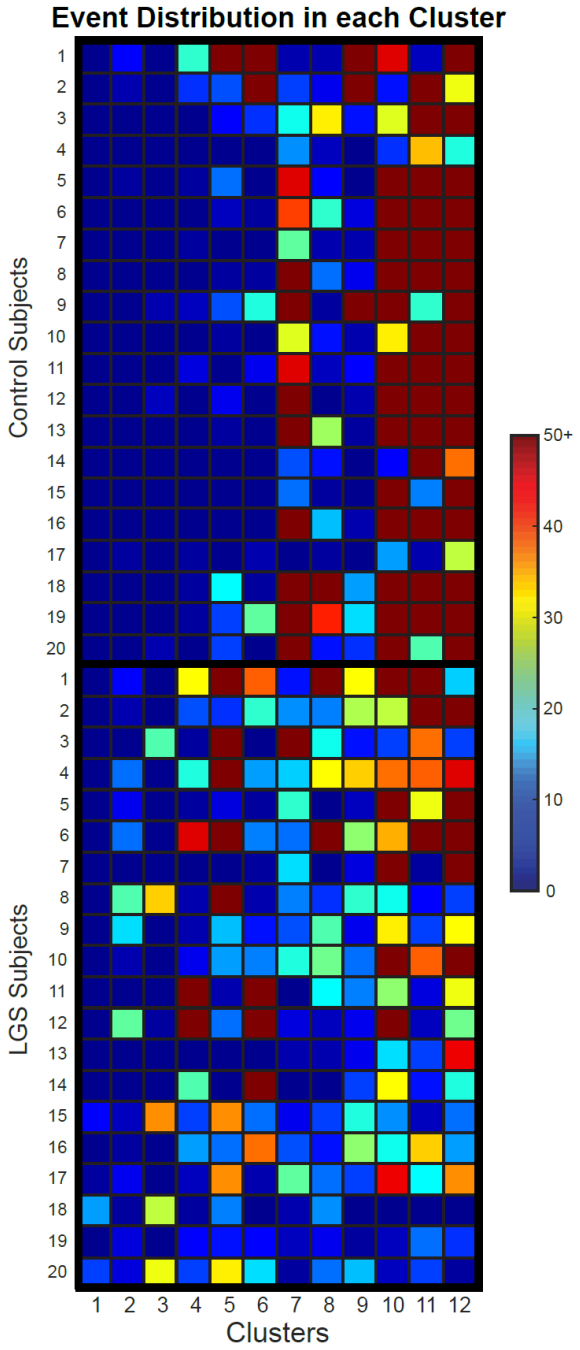

Figure 4.5. Heatmap showing the number of events in each cluster for controls and LGS subjects, where a warmer color indicates more events in a cluster. LGS subjects more frequently had events in clusters 1-5, which generally had higher values of the six features. Control subjects had a majority of events in clusters 10-12, which generally had low values of the six features. The maximum color limit was set to 50 for visualization; note that some data points exceeded this value.

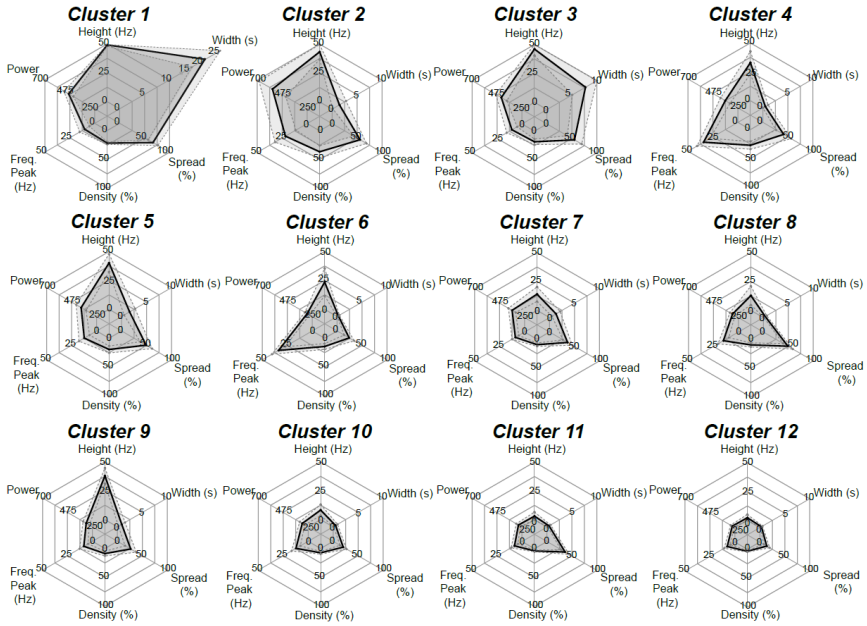

Figure 4.6. Radar plots showing the mean (black line) and standard deviation (grey dashed line) of the feature values for each of the twelve cluster centroids. Each cluster is characterized by a different combination of the six features.

4.3.2 Classification of subject type was accurate and consistent between raters

The IRR for the determination of subject type (i.e. LGS vs. control) associated with each event was favorable, with $\kappa = 0.790$ and ICC = 0.790 (95% confidence interval [CI] 0.769 to 0.809) across the 1350 events selected for visual analysis (Table 4.1). Both control and LGS subject labels had similar agreement between raters, with an EAR of 0.806 and 0.813, respectively (Table 4.2). The mean accuracies for subject classification were 84.4%, 84.7%, and 86.0% for the three reviewers, with significantly lower accuracies for events from LGS subjects compared to events from control subjects for all three raters (Table 4.3; $p<0.05$, Mann-Whitney U-test). All subject classification metrics were consistent between different raters with no significant differences in the subject labels between the three raters ($p>0.05$, Mann-Whitney U-test; 3 of 3 comparisons).

Table 4.1. Interrater reliability for classification of subject type and event type for EEG events. The three visual reviewers are listed as raters A, B, and C.

Label Type	Rater	Count	Agreement	Kappa	ICC	95% CI
Subject	A-B	450	0.907	0.813	0.814	0.780-0.843
	A-C	450	0.916	0.831	0.831	0.798-0.859
	B-C	450	0.862	0.725	0.725	0.678-0.767
	All	1350	0.895	0.790	0.790	0.769-0.809
Event	A-B	450	0.671	0.560	0.627	0.567-0.681
	A-C	450	0.682	0.572	0.685	0.633-0.731
	B-C	450	0.671	0.538	0.697	0.646-0.741
	All	1350	0.675	0.558	0.669	0.638-0.698

Table 4.2. Event agreement rate for subject type and event type. The three visual reviewers are indicated by A, B, and C. The number in parentheses represents the number of events given that subject or event label by either reviewer.

Category		Event Agreement Rate (n)			
		A-B	**A-C**	**B-C**	**All**
Subject type	**Control**	0.831 (248)	0.834 (229)	0.757 (255)	0.806 (732)
	LGS	0.828 (244)	0.853 (259)	0.759 (257)	0.813 (760)
Event type	**SSW**	0.720 (168)	0.727 (154)	0.682 (154)	0.710 (476)
	GPFA	0.400 (25)	0.378 (45)	0.151 (53)	0.285 (123)
	Seizure	0.000 (1)	0.000 (3)	0.000 (0)	0.000 (4)
	Spindle	0.500 (82)	0.480 (100)	0.492 (59)	0.490 (241)
	Vertex	0.100 (40)	0.053 (19)	0.194 (31)	0.122 (90)
	Muscle	0.360 (25)	0.000 (15)	0.000 (18)	0.155 (58)
	Artifact	0.111 (9)	0.167 (12)	0.000 (11)	0.094 (32)
	Nothing	0.561 (205)	0.577 (215)	0.631 (241)	0.592 (661)
	Other	0.023 (43)	0.100 (30)	0.065 (31)	0.058 (104)

Table 4.3. Accuracy for subject type for visual reviewers A, B, and C.

Rater	Number of Events			Rater Accuracy		
	Control	**LGS**	**All**	**Control**	**LGS**	**All**
A	337	563	900	0.956	0.778	0.844
B	338	562	900	0.979	0.767	0.847
C	337	563	900	0.926	0.821	0.860

4.3.3 Interrater reliability for event type was inadequate, with very low agreement rates for some types of waveforms

The IRR for event type had κ values ranging from 0.538 to 0.572, with a mean value of 0.558 (Table 4.1). The ICC between raters was also below adequate, with an ICC of 0.669 (CI 0.638 to 0.698). Across the 1,350 visually classified events, the event types with the highest number of consistent ratings between reviewers were those labelled as SSWs (n = 338, EAR =

0.710), nothing (n = 391, EAR = 0.592), and sleep spindles (n=118, EAR = 0.490), although the EAR values for nothing and sleep spindles did not indicate high levels of agreement. The high number of events labeled “nothing” further confirms the highly sensitive nature of the automated algorithm for identification of events. The EAR values for other waveforms, such as GPFAs (n=35 with matching labels, EAR = 0.285) and vertex waves (n=11, EAR = 0.122), were low, indicating significant disagreement in identifying LGS waveforms and sleep architecture, respectively (Table 4.2).

The mismatches in event labelling mostly occurred when one rater labelled the event as nothing (Figure 4.7). Of the 439 events with a disagreement in event labels between the two reviewers, 270 events (61.5%) were labeled as nothing by one reviewer. This happened most frequently for non-epileptiform events; for example, mismatched labels of spindle/nothing occurred 83 times, and labels of vertex/nothing occurred 54 times, accounting for a total of 31.2% of all events with mismatched labels. Of the event types typically associated with epilepsy, SSWs had the highest EAR, but 37.0% of all SSWs with mismatched labels occurred when one rater marked nothing. For GPFAs, the mismatches occurred when the second rater chose SSW (38.6%), muscle artifact (21.6%), nothing (18.0%), and sleep spindles (12.5%).

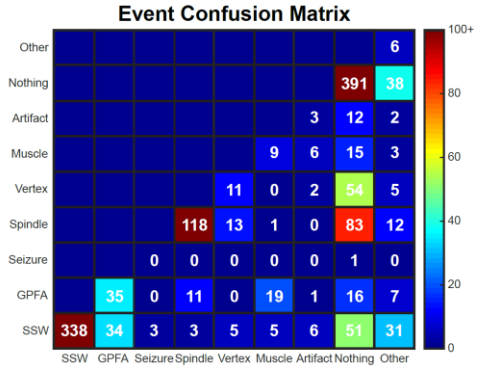

Figure 4.7. Confusion matrix for event classification. Most disagreements were due to one rater labelling the event as nothing while the second rater labeled the event as something else.

4.4. Discussion

The present study evaluated the rater accuracy and IRR of EEG events in both healthy controls and patients with LGS. Events were selected for analysis in an automated, objective manner using the EEG time-varying power spectrum. The visual classification of 1,350 events by three pediatric epileptologists demonstrated favorable interrater agreement in identifying control vs. LGS EEG, using a 15-second clip of deidentified EEG. The IRR and EAR for event type were low, particularly in crucial EEG waveforms such as GPFA and spindles. Mismatched labels for events most frequently occurred when one of the raters labelled the event as nothing, suggesting that reviewers had different tolerances for variation in individual events relative to a stereotypical appearance. These results highlight EEG features that can be robustly identified, as well as those with high levels of disagreement between experts. This can guide future work on objectively defining such waveforms and evaluating their utility as biomarkers of diagnosis and treatment response, which will ultimately improve the long-term outcomes of patients with LGS.

Our results are in line with prior IRR studies on EEG event classification. For example, raters had κ =0.43 in marking epileptiform events vs. benign paroxysmal activity (Halford et al. 2013). Another study had clinical experts score 13,262 candidate interictal epileptiform discharges in epilepsy and control subjects that were clustered into groups with similar morphologies (Jing et al. 2020). This study reported an IRR of κ =0.487 for the interictal epileptiform activity score, and the authors suggested that the requirement to make binary decisions, rather than assigning probabilities, contributed to the level of disagreement. These findings are consistent with our result that most mismatched labels occurred when one rater classified an event as a meaningful EEG waveform while another rater other classified the event as nothing.

4.4.1 Automated event detection in subjects

The automated process for EEG analysis identified time-frequency events with high power in all subjects. Of the 794 events with rater agreement, epileptiform waveforms such as SSWs and GPFAs came from fifteen LGS (two control) and eight LGS (zero control) subjects, respectively. In contrast, normal sleep EEG waveforms such as spindles and vertex waves were only seen in three LGS (eighteen controls) and zero LGS (nine controls), respectively. This is consistent with a prior LGS sleep study, which reported that sleep spindles were absent in most LGS subjects (Markand 1977). Sleep spindles and vertex waves may also be difficult to recognize in LGS subjects due to the presence of frequent epileptiform discharges during NREM sleep (Markand 1977; Horita et al. 1987; Wheless and Constantinou 1997).

4.4.2 Rater accuracy for subject identification

The accuracy for classifying subject type was generally good across all three raters, with an average accuracy of 85% across all events. The rater accuracy was similar between controls and LGS subjects in clusters one through six, where raters had a mean classification accuracy of 96.5% for control events and an accuracy of 91.3% for LGS events. The rater accuracy was significantly greater in controls compared to LGS subjects in clusters seven through twelve, where raters had a mean classification accuracy of 95.3% for control events and an accuracy of 64.3% for LGS events. This was expected, as control subject EEG should only contain normal physiological events, which are unlikely to be mistaken for epileptiform activity. In contrast, LGS subjects have both epileptiform events and normal physiological events, of which the latter are likely to result in mismarking of an event as coming from a control subject. Because LGS events more frequently occurred in clusters 1 through 6, rater accuracy for events from LGS subjects decreased as the cluster number increased, with cluster 12 having the lowest accuracy by far (Table 4.4).

Table 4.4. Rater accuracies for subject labels in each cluster and subject group. Clusters are sorted in descending order based on the sum of the z-scores for the six TFI features. Rater accuracy for LGS subjects decreases as the cluster number increases.

	Rater A				Rater B				Rater C		
Cluster	**All**	**Control**	**LGS**		**All**	**Control**	**LGS**		**All**	**Control**	**LGS**
C1	1.00	N/A	1.00		1.00	N/A	1.00		1.00	N/A	1.00
C2	0.94	0.88	0.94		0.94	1.00	0.93		0.98	1.00	0.97
C3	0.99	1.00	0.99		0.98	1.00	0.97		0.96	1.00	0.96
C4	0.91	1.00	0.87		0.88	0.96	0.83		0.93	0.96	0.91
C5	0.89	0.86	0.91		0.93	0.95	0.90		0.95	0.95	0.95
C6	0.86	0.98	0.75		0.85	0.98	0.73		0.89	0.95	0.83
C7	0.69	0.94	0.52		0.73	1.00	0.56		0.71	0.94	0.54
C8	0.91	0.92	0.90		0.90	0.97	0.83		0.89	0.90	0.88
C9	0.86	0.95	0.78		0.89	0.98	0.80		0.88	0.92	0.83
C10	0.74	1.00	0.53		0.71	0.95	0.51		0.80	0.89	0.71
C11	0.89	1.00	0.78		0.88	1.00	0.76		0.81	0.83	0.80
C12	0.58	0.97	0.25		0.61	1.00	0.26		0.64	1.00	0.34

4.4.3 Interrater reliability in event classification

The combined, blinded rating of both LGS and control subject events in the same study provides an important benchmark for IRR of EEG waveforms. If all events had come from LGS subjects, the raters would have been biased toward choosing labels associated with pathological events; therefore, using an approximately equal mix of physiological and pathological events let us accurately measure how frequently an event might be interpreted as benign or even “nothing.” However, this broad mix of events coupled with the use of nine different labels for visual analysis likely contributed to the low values of IRR and EAR for event classification. To verify that this was not the case, we recalculated the metrics using three broader categories consisting of: (1) pathological (SSW, GPFA, seizure), (2) physiological (spindle, vertex), and (3) others (muscle, artifact, none, other). The use of fewer labels did not substantially improve IRR (κ =0.558 to κ =0.628) or the EAR (pathological = 0.724, physiological = 0.447, others = 0.623) (Figure 4.8). The similarities in rater agreement when using broad

categories suggests that the disagreement between clinicians is not due to subtle differences between event types.

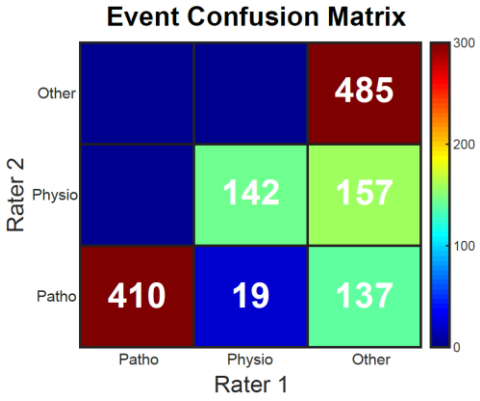

Figure 4.8. Confusion matrix for events grouped as pathological (GPFA, SSW, seizures), physiological (spindles and vertex), and other (muscle, artifact, nothing, and other). The interrater reliability of events using broad terms remains inadequate.

4.4.4 Limitations

There are several limitations to our study related to the event detection and subject data. First, the event detection was accomplished using the Fz channel, which captures the frontocentral activity typical of spindles and GPFA or generalized activity such as slow spike and wave but is insensitive to localized events occurring elsewhere on the head. Second, the EEG epochs were not selected from a specific stage of sleep, and thus they were not entirely representative of a subject's brain activity over longer periods of time, as paroxysmal events such as GPFAs and SSWs may appear infrequently or not at all within the 10-minute time windows. However, both limitations would only affect the number of different types of events in the data set and not the raters' ability to classify them.

Rater accuracies may have also been affected by the difficulty of classifying individual events compared to conventional EEG visual analysis. The graphical user interface was designed to mimic standard clinical viewing software, but event labelling was done using fifteen seconds of isolated EEG, without having the full EEG study for context. We compensated for

this by allowing raters to use the entire clip as context, but this may have influenced some labels by introducing other salient EEG features within the clip. For example, an event with short duration (~100 ms) may not initially look significant, but if an epileptiform discharge occurs later in the 15-second clip, the rater may be more likely to choose a label associated with a pathological event. While the use of a deidentified short clip of EEG instead of the entire study can reduce bias, future studies may want to evaluate clinically marked events in tandem with automated event detections to compare the differences between these two methods. More generally, to the extent that IRR was imperfect for subject type, agreement is likely to be higher in paradigms in which raters assign subject type based on review of full-length clinical EEG, rather than 15-second samples. Conversely, we have shown that raters tend to have high levels of agreement when classifying an EEG sample as having been derived from a patient with LGS or a normal control. In paradigms with diverse patient composition (e.g. a cohort including normal controls, patients with LGS, and patients with other forms of epilepsy), the identification of patients with LGS may be much more challenging and IRR is likely to be far lower.

4.4.5 Conclusions and future work

The present study measured the IRR using events with high EEG power that occurred during NREM sleep in LGS subjects and healthy controls. Our automated, objective algorithm for analysis of the EEG time-frequency decomposition was able to identify known waveforms that were both pathological and physiological. Subject classification had favorable IRR and rater accuracy, suggesting that fifteen seconds of EEG containing at least one event with high power is often sufficient for a reviewer to identify abnormal visual features. The IRR for event classification was lower, with inadequate ICC, in part due to variation in raters' thresholds for labeling specific EEG waveforms.

Future studies can utilize multiple channels in the time-frequency analysis, rather than focusing on only channel Fz, and select EEG epochs longer than 10 minutes to increase the

likelihood of capturing waveforms such as GPFA and SSW in each subject. This work could also be expanded to larger patient populations and different types of epilepsy. This could aid in providing precise, quantitative definitions of pathological EEG events. In turn, this may lessen the ambiguity inherent to visual EEG analysis and thus improve IRR. In the long term, this could facilitate the use of these quantitatively defined waveforms as objective biomarkers, ultimately improving the diagnosis and treatment of patients with LGS.

CHAPTER V

Discovering EEG Biomarkers of Lennox-Gastaut Syndrome through Unsupervised Time-Frequency Image Analysis

5.1 Introduction

The initial diagnosis of epilepsy hinges on identifying early biomarkers of the disease in the electroencephalogram (EEG). These transient electrophysiological abnormalities are typically discovered during the visual review of EEG, where they are manifested as unique/unusual waveforms. The initial descriptions of EEG biomarkers are based on repeated visual observations and are later studied to demonstrate the potential clinical utility of the waveform (Lai et al. 2023). For example, sleep spindles are a physiological EEG waveform that were first identified as waxing-and-waning 10-16 Hz oscillations lasting 0.5-2s during sleep (Andrillon et al. 2011). Future studies later associated sleep spindles with memory consolidation, markers of intelligence, and having altered properties in patients with epilepsy (Latka et al. 2005; Fernandez and Lüthi 2020). Novel biomarkers of epilepsy such as high frequency oscillations (HFOs) were first reported as oscillatory phenomenon in rat hippocampus (Buzsáki et al. 1992) and were verified in humans through the visual review of intercranial EEG, with studies associating their presence with epileptogenesis (Bragin et al. 1999). The visual review and validation of these waveforms can continue for many years; this is the case for HFOs, where there is still no precise definition of the waveform. The difficulty in identifying these waveforms can lead to time-consuming EEG review with low interrater reliability (Jing et al. 2020).

To improve the visual review process, automated algorithms are developed to detect EEG waveforms that are known biomarkers of epilepsy. This type of computational analysis can objectively identify events for large datasets quickly while applying detection criteria consistently

across patients and centers. Some of these algorithms analyze the time-domain version of the EEG signal and aim to match the visual appearance of the event as closely as possible. For example, IED detectors can compare various features of the timeseries such as the Teager energy and slope of the signal (Gaspard et al. 2014). Detectors can also compare the EEG to templates of averaged IEDs (Karoly et al. 2016) or use amplitude thresholds based on features such as the root-mean-square (Charupanit et al. 2020) or peak amplitude to detect HFOs (Charupanit and Lopour 2017). Time-frequency analysis offers a complementary approach, as it can isolate activity in individual frequency bands and offers the opportunity to reject common artifacts or other causes of false positive detections (Jiang et al. 2019). This method has been successfully applied in the automated detection of HFOs in epilepsy (Burnos et al. 2014; Donos et al. 2020; Migliorelli et al. 2020; Krikid et al. 2022) and the characterization and identification of interictal spikes in refractory epilepsies (Jacobs et al. 2011; Jabran et al. 2020).

However, this process of developing detection algorithms has some critical limitations. The detection criteria often rely on empirical definitions derived from descriptions of the visual appearance of the waveform, rather than having a theoretical basis. In this case, detected events may be compared to manual marking of events as the “ground truth”, even though they rely on imprecise definitions and have been shown to vary between reviewers. The development of IED detectors have followed this path. For example, the Persyst (Persyst Development Corporation, USA) IED detector has the highest reported sensitivity and has utility as a screening tool for epilepsy (Reus et al. 2022), but performed slightly worse than human review, had low interrater agreement with clinical markings, and still must be checked and verified by experts (Reus et al. 2022). Furthermore, the performance of detection algorithms is limited by the gold standard, which is commonly defined in studies to be expert review.

These challenges with biomarker discovery and validation are exemplified by a type of epilepsy called Lennox Gastaut Syndrome (LGS). LGS is a severe childhood-onset epilepsy associated with seizures that cause cognitive impairments that worsen over time (Kim et al.

2015). Prompt diagnosis and administration of treatment is paramount for seizure control and long-term neurocognitive outcome (Mastrangelo 2017b). However, this can be delayed due to the progressive and complex nature of the disease. The disease onset of LGS is difficult to define as the seizures and EEG characteristics evolve slowly over time. Patients may also exhibit most, but not all, of the criteria required for diagnosis, or all the criteria, but not all at the same time. Thus, there is a critical need for biomarkers associated with this disease.

One promising candidate biomarker is generalized paroxysmal fast activity (GPFA), a unique waveform that is primarily seen in LGS during NREM sleep (Mastrangelo 2017b). Despite the visual descriptions of GPFA (Kane et al. 2017; Mastrangelo 2017b) and its presence being associated with intractable epilepsies (Cerulli Irelli et al. 2022) and an increase in seizure counts in seizure diaries (Dalic et al. 2022a), the interrater reliability for GPFA remains low (Hu 2023). While automated algorithms can potentially improve the reliability, there is currently no basis for this. An automatic GPFA detector identified events with similar time-frequency properties to manually marked GPFAs in LGS subjects, but required individualized patient settings and only had a 40-80% rater agreement with manual markings (Omidvarnia et al. 2021).

Therefore, we developed an automatic, unsupervised approach to the analysis of time-frequency EEG that does not rely on visual review of the data or preestablished clinical definitions. This is a data-driven approach that aims to identify relevant EEG events that are primarily associated with either LGS subjects or controls, while applying minimal restrictions to event morphology. This process not only identified known biomarkers of LGS, such as slow spike-wave and GPFA, but also led to the discovery of EEG waveforms that are novel candidate biomarkers of LGS.

5.2. Methods

5.2.1 Subject information

Approval for this retrospective observational study was obtained from the Institutional Review Board of the Children's Hospital of Orange County (CHOC) and the University of California, Los Angeles (UCLA), with the requirement for informed consent waived. Twenty subjects diagnosed with LGS (7 females, median age 7.4 years, IQR 8.9 years) were retrospectively identified from the clinical record at CHOC, with visits between January 2012 and June 2020. A group of fifty controls was identified in a separate study, where patients were retrospectively identified from the clinical record at UCLA, with visits between February 2014 and July 2018 (Smith et al. 2021b). Controls were included if they had (1) no known neurological disorders, (2) routine EEG studies that were interpreted as normal by a board-certified pediatric epileptologist, and (3) no use of neuroactive medications. A subset of twenty controls (8 females, median age 8.2 years, IQR 8.8 years) was selected from the cohort of 50 to be approximately age-matched to the LGS cohort. There was no significant difference in age between control and LGS subjects ($p = 0.672$, Student's t-test); the breakdown by sex was approximately the same between both groups.

5.2.2 EEG acquisition and preprocessing

Control and LGS EEG data were both recorded using a Nihon Kohden EEG acquisition system, with nineteen scalp electrodes placed according to the international 10-20 system (Fp1, Fp2, F3, F4, C3, C4, P3, P4, O1, O2, F7, F8, T3, T4, T5, T6, Fz, Cz, Pz). All EEG data were recorded at a sampling frequency of 200 Hz or downsampled to 200 Hz. EEG data for LGS subjects were collected overnight and manually clipped by a registered polysomnographic technologist to contain NREM sleep with no arousals or movement artifacts. Control EEG data were collected overnight and clipped by an EEG reviewer to contain sleep EEG based on the presence of sleep architecture, posterior dominant rhythm, and slow roving eye movements (Smith et al. 2021c). After clipping the EEG, segments of broadband data containing high-amplitude artifacts were identified in each subject using an automated detector as in prior

studies (Smith et al. 2021b; Hu et al. 2022). For each subject, one ten-minute segment of clean, continuous, NREM sleep EEG with no automated or clinically detected artifacts was selected for data analysis. All EEG data were re-referenced to the common average and filtered with a zero-phase shift digital filter from 0.5-55 Hz. All electronic data were deidentified and analyzed offline using custom MATLAB (Mathworks) scripts.

5.2.3 Time-frequency decomposition

For each subject, we used the following procedure to obtain the EEG time-frequency decomposition prior to identifying events of interest. The EEG data were first pre-whitened in the time-domain using first-order backward differencing to remove the $\frac{1}{f^{\propto}}$ trend in the power spectrum of the EEG (Usui and Amidror 1983; Gardner et al. 2007b; Roehri et al. 2016). The discrete whitened signal $\tilde{x}[n]$ was obtained by taking the difference between subsequent elements of the EEG $x[n]$:

$$\tilde{x}[n] = x[n] - x[n-1] \qquad (5.1)$$

The time-frequency decomposition of the EEG was calculated using the Stockwell transform (S-transform). The S-transform is an alternative to the short-time Fourier transform and continuous wavelet transform that has frequency-dependent resolutions that can facilitate the detection of high frequency bursts (Stockwell 1996; Krikid et al. 2022). The S-transform wavelet changes for each frequency band and is defined by the following equation:

$$w(t,f) = \frac{|f|}{\sqrt{2\pi}} e^{\frac{-t^2 f^2}{2}} e^{-i2\pi ft} \qquad (5.2)$$

The S-transform was calculated for each channel in each EEG segment for frequencies from 1 to 50 Hz, with a step size of 1 Hz (Figure 5.1).

5.2.4 Identifying events of interest

To identify events of interest for analysis, we first define the time-frequency decomposition as $X_{t,f,e}$ where X is the power, t is time, f is frequency, and e is the electrode at which the EEG was measured. For each EEG channel, we identify the set of all ordered doublets TF whose power exceeds the threshold P in the time-frequency decomposition:

$$TF_e = \{(t,f) \mid X_{t,f,e} > P\} \qquad (5.3)$$

A threshold of $P = 250\,\frac{\mu V^2}{Hz}$ was used for all subjects, resulting in the selection of 4.6% of all time-frequency values across all subjects, corresponding to a z-score of 1.69. This threshold was fixed across all frequency bands, as the data were pre-whitened, and was used for all LGS and control subjects. This relatively low threshold was chosen to prioritize high sensitivity in the detection of events.

For each subject, we divided the set TF_{Fz} into i discrete events of interest (EOI), with each one denoted as $EOI_{i,Fz}$ (Figure 5.1D). EOIs were selected using EEG from the Fz electrode for two reasons: (1) the fronto-central location should be minimally impacted by eye movements and muscle artifact, and (2) Fz is maximally sensitive to known EEG waveforms such as sleep spindles and GPFAs(Bansal et al. 2019). Each EOI fulfilled the following conditions:

1. $EOI_{i,Fz}$ is a compact set of ordered doublets (t,f) where the time points in the event are consecutive.
2. $(max_t(\{EOI_{i,Fz}\}) - min_t(\{EOI_{i,Fz}\})) \geq \tau$

Where τ is the minimum duration of an EOI. We chose $\tau = 100$ milliseconds to fully capture the duration of an epileptic spike, the shortest event we expected to see. Note that such sharp waveforms are typically 40-60 milliseconds and often appear smeared (with longer duration) in the time-frequency decomposition, particularly at low frequencies.

5.2.5 Event features

For each $EOI_{i,Fz}$, we calculated eleven features based on its temporal, spectral, and spatial properties (Figure 5.2):

7. Height (Figure 5.2A): For each EOI, the height is defined by the highest frequency minus the lowest frequency:

$$Height_i = max_f(\{EOI_{i,Fz}\}) - min_f(\{EOI_{i,Fz}\}) + 1 \qquad (5.4)$$

   The height ranges from 1 to 50 Hz, as the frequencies range from 1 Hz to 50 Hz.

8. Length (Figure 5.2B): The length corresponds to the duration of the event in seconds and is defined by:

$$Length_i = max_t(\{EOI_{i,Fz}\}) - min_t(\{EOI_{i,Fz}\}) \qquad (5.5)$$

9. Spread (Figure 5.2C): The spread is a measure of how many other electrodes have events that overlap the Fz EOI in time and frequency:

$$Spread_i = \frac{\sum_{e=1}^{nElec} \left|\{EOI_{i,Fz} \cap EOI_{i,e}\}\right|}{nElec * \left|\{EOI_{i,Fz}\}\right|} \qquad (5.6)$$

   Where $\left|\{EOI_{i,Fz} \cap EOI_{i,e}\}\right|$ is the cardinality of the intersection between an EOI in Fz and an EOI in electrode e, $nElec$ is the total number of EEG electrodes, and $\left|\{EOI_{i,Fz}\}\right|$ is the cardinality of the EOI in Fz. The spread ranges from 1/19 to 1, where a spread of 1/19 indicates that no other electrodes exhibit high EEG power (exceeding the threshold P) at the same time and frequency as the Fz electrode; a spread of 1 indicates that all other electrodes exhibit high EEG power at the same time-frequency points as the Fz electrode.

10. Density (Figure 5.2D): The density is the area of the event in time-frequency space, normalized by the event length and the maximum possible height:

$$Density_i = \frac{\left|\{EOI_{i,Fz}\}\right|}{nFreq * Length_i * fs} \qquad (5.7)$$

Where $nFreq$ is the number of frequencies analyzed (50 for this study) and fs is the sampling rate. A density of 1/50 indicates that the event has high power at a single frequency at

each time point, and a density of 1 indicates that all possible frequencies and time points exceed the power threshold.

11. Frequency of Peak Power (FPP, Figure 5.2E): The FPP is the frequency at which the EOI had maximum power. Here, the FPP ranges from 1 to 50 Hz, based on the frequency range included in the time-frequency spectrogram. The FPP is defined by:

$$FPP_i = argmax_f(EOI_{i,Fz}) \qquad (5.8)$$

12. Band Power (BP, Figure 5.2F): The BP is the mean band power across all time points in the EOI within a frequency band. The BP is defined by:

$$BP_{i,Band} = \frac{\sum_{f=F_1}^{F_2} \sum_{t=argmin_t(EOI_{i,Fz}\})}^{argmax_t(\{EOI_{i,Fz}\})} X_{t,f,Fz}}{(F_2 - F_1 + 1) * Length_i} \qquad (5.9)$$

Where F_1 and F_2 correspond to the minimum and maximum frequencies within the chosen frequency band, respectively. The BP was calculated for the following six frequency bands: Delta (2-4 Hz), Theta (4-7 Hz), Alpha (8-12 Hz), Sigma (12-15 Hz), Beta (15-30 Hz), and Gamma (30-50 Hz).

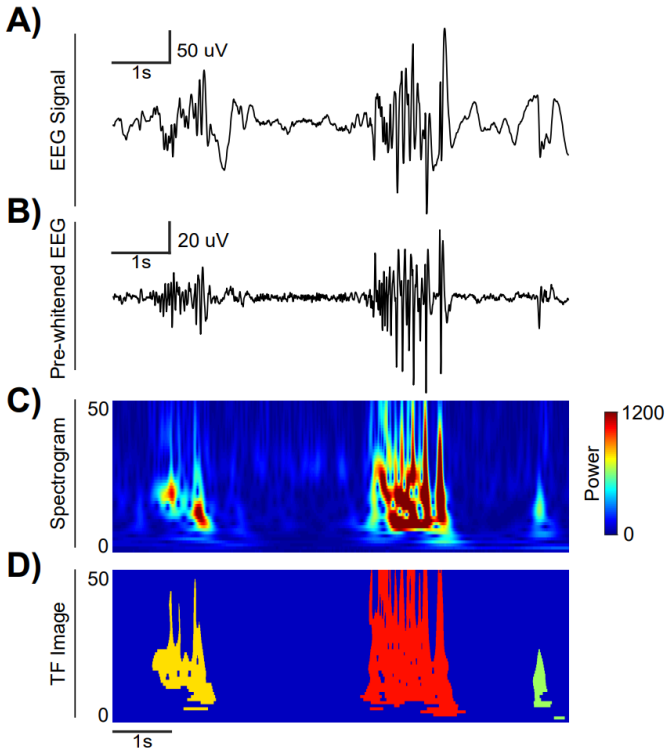

Figure 5.1. An example of EOI identification, using an eight second EEG sample in the Fz channel. (A) The analysis begins with the broadband EEG signal. (B) The EEG for each channel was first prewhitened. (C) The time-frequency decomposition was calculated using the S-transform for the entire EEG clip. (D) Events of interest (EOIs) were defined as consecutive time points in which the EEG power exceeded a threshold for a minimum duration. Three different EOIs are shown in this EEG clip, one in yellow, one in red, and one in green.

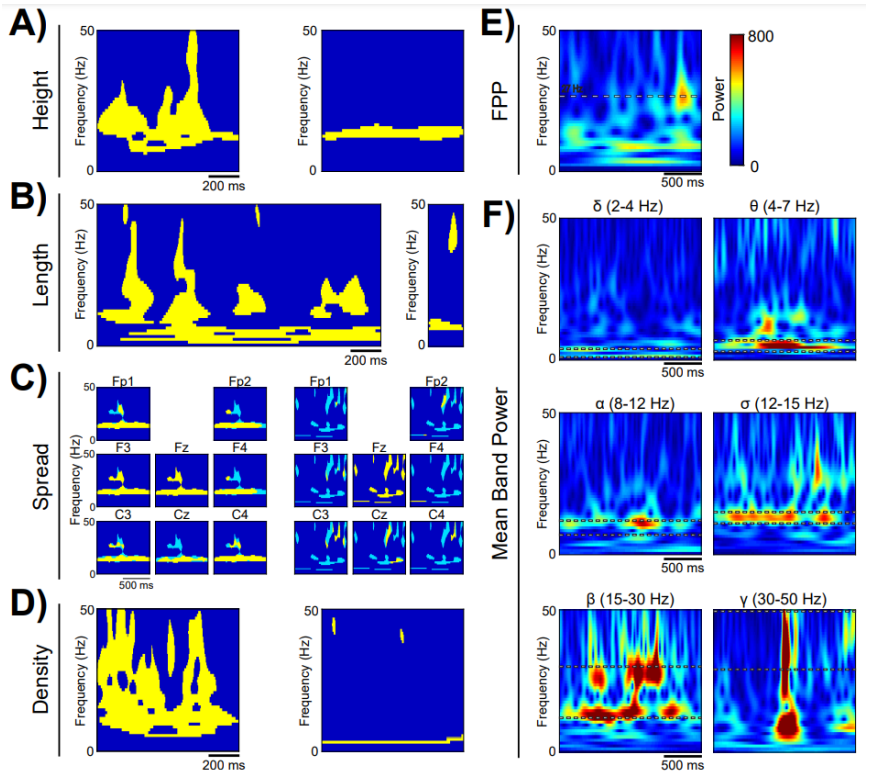

Figure 5.2. Examples of EOIs with high (left subfigure) and low (right subfigure) feature values for (A) height, (B) length, (C) spread, and (D) density. The figures on the right consist of EOIs with high (E) frequency of peak power and high (F) mean band power in each characteristic frequency band. In (C), the spread is visually represented using electrodes adjacent to Fz, where yellow regions indicate overlap of the EOI in electrode Fz with the TF for adjacent electrodes and cyan indicates regions where the TF for adjacent electrodes does not overlap with the EOI for Fz.

5.2.6 Clustering analysis

Prior to clustering, each feature was normalized by converting the values to a z-score based on the mean and standard deviation of each feature across all control and LGS events. EOIs from control and LGS subjects were collectively partitioned into twelve different clusters using k-means based on their event features (Lloyd 1982). Each EOI was treated as a single observation, where each observation consisted of the eleven z-scores of the event features. For visualization of the results, clusters were sorted in descending order based on the sum of the eleven feature z-scores, such that cluster 1 has the highest and cluster 12 has the lowest sum.

5.2.7 Feature categorization

One limitation of clustering is that the clusters may change when the method is applied to a different dataset or new subjects are added, thus reducing the repeatability of the results. Therefore, as a complement to clustering, we implemented a second method that categorized each event based on whether its features had high or low values. The median values for height, length, spread, and density were calculated across all events, and each feature was categorized as weak (lower than the median) or strong (higher than the median). In addition, we identified the frequency band for the event that had the highest BP. Then, to denote the category for each event using these features, we used a five-character string starting with the frequency of highest BP (δ, θ, α, σ, β, γ), followed by characters indicating weak/strong height (h/H), length (l/L), spread (s/S), and density (d/D). In total, there were 96 different feature categories. For example, an event with the highest power in the alpha band with a height and spread above the median was in the category "αHlSd."

5.2.8 Visual classification and event labelling

To provide an interpretation of the type of EEG events in each cluster, we paired the computational analysis with visual classification of the events. Of the 11,708 EEG events, we selected 1,350 for visual analysis by three board-certified pediatric epileptologists from two different institutions (CHOC and UCLA). Details of the selection and visual analysis process can be found in Hu et al. 2023; we briefly summarize them here. The selection procedure aimed to include a representative distribution of the broad range of events, prioritizing selection of an approximately equal number of LGS and control events. Each rater classified 900 events, which were selected across all twelve clusters; each event was independently marked by two different raters. For each event, raters were shown a fifteen-second clip of EEG, with a red line indicating when the event started and ended. Raters were blinded to the subject type, subject number, and the time at which the EEG clip was recorded. Raters were asked to classify each event as one

of the following: (1) IED, (2) interictal epileptiform discharge train (IEDT), (3) GPFA, (4) seizure, (5) sleep spindle, (6) vertex sharp, (7) muscle, (8) artifact, (9) other event, or (10) no event. Events were viewed and marked using a custom GUI that was designed using MATLAB based on clinician feedback.

To validate the events labelled as sleep spindles in our analysis, we also ran an automated sleep spindle detector (Mensen et al. 2018) on the same dataset across all subjects. Potential sleep spindles were detected if there was a power value exceeding four times the median absolute deviation of the EEG in the 10-16 Hz range. A secondary threshold was also applied so that the start and end times of the spindle also had to exceed two times the median absolute deviation. Lastly, sleep spindles were valid if the event lasted between 300ms to 3s. For each subject's EEG, the spindle detector recorded the total number of sleep spindles and their corresponding length, global spread, and peak frequency.

5.3. Results

5.3.1 EEG events in LGS subjects have higher power, height, spread, frequency of peak power, and density compared to controls

A total of 11,708 events were detected automatically across all forty subjects, with 6,744 events coming from the twenty control subjects ($n_{controls}$ = 365.0 [259.0-443.0] events; reported as the median [Q1-Q3] for all results) and 4,964 events coming from the twenty LGS subjects (n_{LGS} = 232.5 [156.0-324.5]). The minimum number of events reported in a single subject was 49 and the maximum number of events was 560.

The height, spread, FPP, density, sigma BP, beta BP, and gamma BP of LGS events were significantly greater than control events (Figure 5.3; $p<0.05$, Mann-Whitney U-Test, Bonferroni corrected for n=11). The differences between the LGS and control event features were typically caused by the heavier right-sided tails in the distributions for LGS events. Identifying events with different thresholds ranging from $P = 200$ (7.7% of the data) to $P = 300$

(3.0% of the data) yielded qualitatively similar results with similar histogram distributions (Figure 5.4).

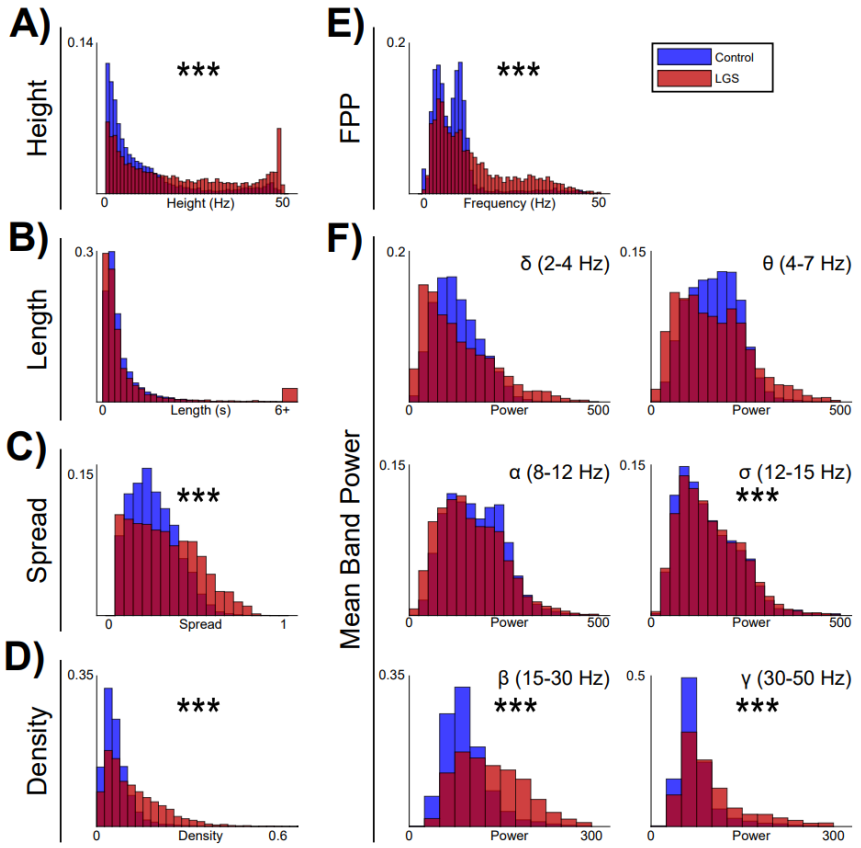

Figure 5.3. Normalized histograms of the eleven features: (A) height, (B) length, (C) spread, (D) density, (E) frequency of peak power, (F) delta BP, (G) theta BP, (H) alpha BP, (I) sigma BP, (J) beta BP, and (K) gamma BP for control (blue) and LGS (red) events. LGS events more frequently had high values of height, frequency of peak power, spread, density, sigma BP, beta BP, and gamma BP compared to controls. Significance levels are *p<0.05, **p<0.01, and ***p<0.001, with p-values modified using the Bonferroni method.

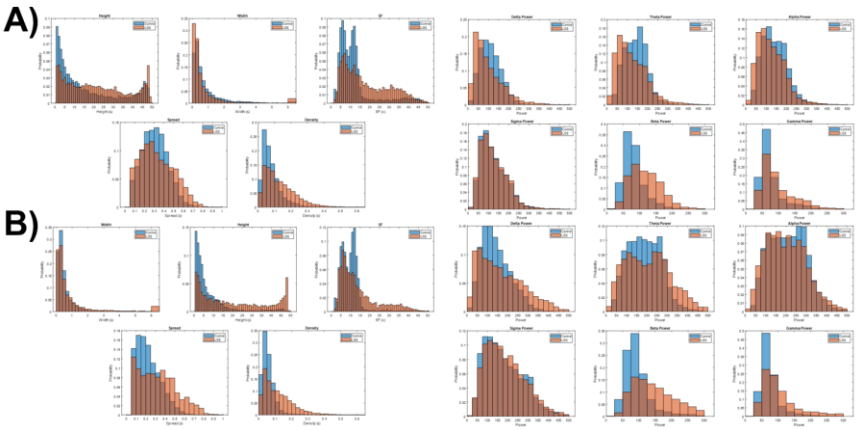

Figure 5.4. Normalized histograms of the eleven features using (A) P = 200 and (B) P = 300. Using different thresholds for event detection yielded similar histogram distributions for all features for both control and LGS events.

5.3.2 Clustering isolates events unique to LGS subjects

When k-means clustering was applied to the combined group of LGS and control events, there were no clusters composed of events from a single subject. On average, each subject contributed events to 8.2 different clusters (Figure 5.5A). Each cluster's centroid was characterized by a different combination of the eleven features (Figure 5.6). For example, the events in Cluster 1 typically lasted one to two seconds with high values for height, electrode spread, density, and high alpha/sigma band power. Events in Cluster 2 lasted an average of eighteen seconds and had high height, electrode spread, and high delta/theta band power. The cluster centroids remained quantitatively similar after clustering with different thresholds of $P = 200$ and $P = 300$ (Figure 5.7).

Several clusters contained events primarily from subjects with LGS. Specifically, clusters 1, 2, 3, 4, 5, and 9 had significantly more LGS events than control events, consisting of 100%, 100%, 90.7%, 80.0%, 91.8%, and 77.9% LGS events, respectively (Figure 5.5B; $p<0.05$, permutation test, Bonferroni corrected for n=12). These clusters tended to have high values of band power and other features. In contrast, clusters 10, 11, and 12 consisted of 24.7%, 33.1%, and 27.9% LGS events, respectively, and they had low values of the eleven features.

Representative control and LGS events with features most similar to each cluster centroid are shown in Figure 5.9. Re-clustering the events with 6, 9, 15, and 18 clusters resulted in clusters with similar mean centroids that had significantly more LGS than control events (Figure 5.8).

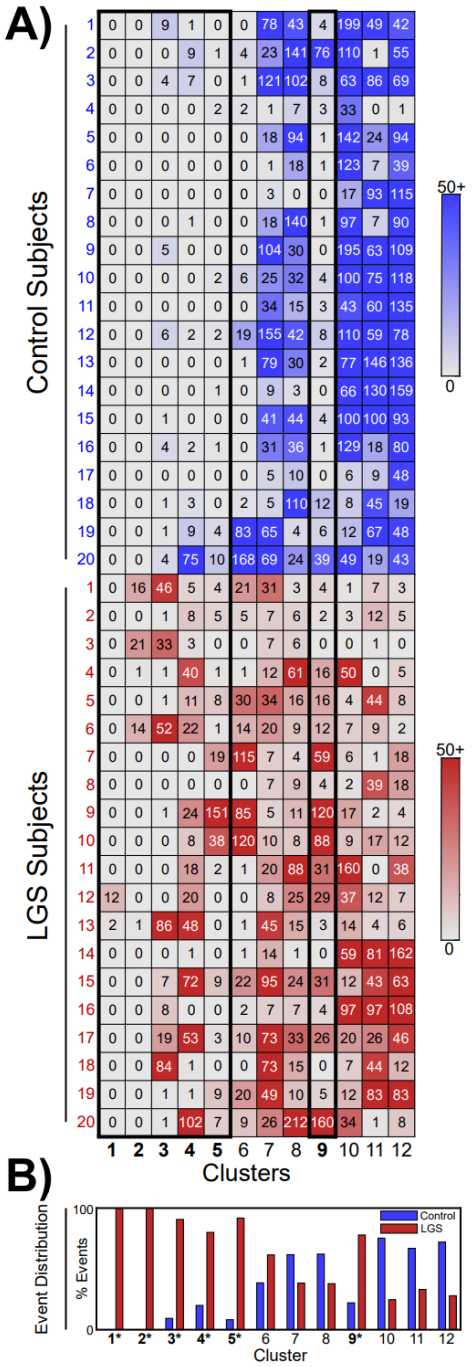

Figure 5.5. Six clusters were comprised of events primarily originating from LGS subjects. (A) Heatmap of the number of events in each cluster for all control (top) and LGS (bottom) subjects. (B) The percentage of control and LGS events in each cluster. Clusters 1, 2, 3, 4, 5, and 9 had a significantly greater number of events from LGS subjects compared to controls and are bolded.

Cluster	Height (Hz)	Length (s)	Spread (%)	Density (%)	FPP (Hz)	Delta	Theta	Alpha	Sigma	Beta	Gamma
1	45.7 (1.3)	1.5 (0.5)	51.9 (8.9)	49.6 (7.5)	12.4 (2.3)	141.6 (46.9)	253.8 (77.6)	953.1 (219.6)	913.1 (202.9)	635.8 (112.8)	252.3 (72.8)
2	48.5 (0.5)	17.7 (6.4)	64.8 (10.9)	22.0 (3.4)	10.4 (4.7)	386.2 (51.7)	420.5 (84.8)	303.5 (47.2)	231.1 (36.8)	159.0 (21.4)	102.8 (28.6)
3	42.4 (8.5)	4.0 (2.6)	51.8 (13.0)	17.2 (4.7)	9.3 (5.3)	310.1 (72.6)	342.7 (80.2)	258.5 (73.1)	202.9 (59.6)	135.4 (32.5)	90.2 (22.4)
4	40.3 (7.7)	1.2 (1.0)	49.1 (13.7)	25.1 (6.9)	18.1 (8.1)	147.7 (69.1)	193.9 (73.0)	269.6 (94.1)	313.6 (109.9)	223.0 (57.0)	137.5 (41.7)
5	31.0 (8.0)	0.4 (0.4)	38.6 (14.9)	31.7 (6.7)	34.9 (5.8)	82.1 (44.0)	94.4 (46.7)	106.7 (52.4)	128.8 (64.4)	217.9 (74.9)	284.3 (70.7)
6	26.4 (12.7)	0.3 (0.3)	27.0 (12.7)	15.1 (5.2)	36.6 (5.5)	102.4 (58.3)	115.3 (60.7)	102.2 (54.2)	101.8 (53.0)	130.1 (37.9)	183.1 (40.8)
7	26.2 (12.6)	1.2 (0.8)	35.2 (13.3)	9.7 (3.2)	9.5 (4.7)	178.7 (60.1)	229.5 (58.1)	200.1 (64.8)	162.6 (49.4)	105.2 (25.4)	81.6 (23.2)
8	9.4 (7.6)	0.4 (0.3)	36.4 (12.1)	8.2 (3.0)	13.1 (2.1)	84.2 (41.6)	110.4 (45.9)	208.6 (72.4)	259.2 (53.2)	116.4 (30.6)	74.2 (20.3)
9	13.5 (8.4)	0.2 (0.1)	25.9 (14.5)	11.6 (4.2)	22.2 (4.4)	69.3 (42.6)	87.1 (44.0)	102.5 (50.1)	139.4 (63.9)	195.5 (33.3)	103.2 (30.5)
10	4.6 (4.2)	0.3 (0.3)	18.4 (8.5)	5.4 (2.0)	10.8 (1.7)	92.2 (44.0)	120.0 (46.1)	228.7 (45.2)	165.0 (52.1)	80.4 (23.5)	64.2 (18.9)
11	5.2 (6.9)	0.7 (0.5)	25.2 (13.5)	3.6 (1.7)	5.1 (2.3)	209.1 (39.7)	172.1 (50.0)	113.5 (39.0)	92.9 (33.8)	70.5 (18.9)	62.8 (16.8)
12	2.9 (3.9)	0.4 (0.3)	22.6 (12.8)	3.6 (1.6)	6.5 (1.6)	104.9 (35.6)	219.1 (40.2)	121.3 (40.9)	91.5 (35.5)	69.6 (20.9)	61.5 (17.9)

Figure 5.6. Mean cluster centroid values for each feature. The opacity of the cells indicates the value of the feature compared to all other clusters, with low values appearing white. Clusters with a significantly greater number of LGS events to controls are bolded.

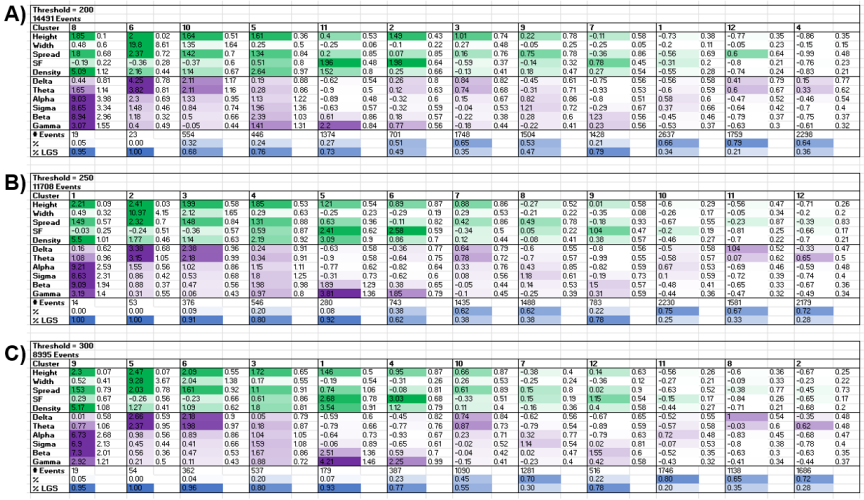

Figure 5.7. Varying the threshold for event detection produces clusters with similar feature centroids. Event detection thresholds of (A) P=200, (B) P=250, and (C) P=300 yielded similar feature centroids with similar ratios of control to LGS events. Features with greater values are indicated by a stronger color. The opacity of the green cells indicates the value of the feature compared to all other clusters, with low values appearing white; similarly, the opacity of the purple cells corresponds to frequency BP, and the opacity of the blue cells indicates the relative number of control and LGS events. Clusters using a threshold of 250 are sorted in descending

order based on the sum of the z-scores; clusters using a threshold of 200 and 300 are sorted to best match the clusters with a threshold of 250.

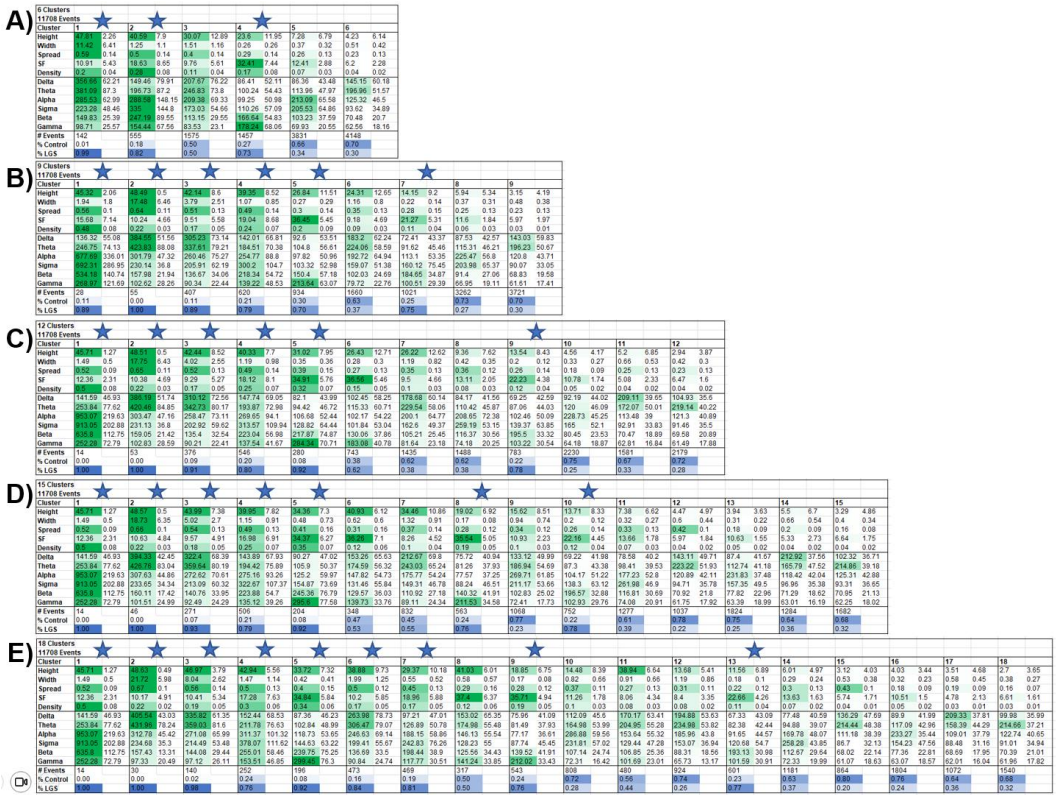

Figure 5.8. The same LGS-associated clusters are produced for varying numbers of clusters. The 11,708 detected events were clustered into (A) 6, (B) 9, (C) 12, (D) 15, and (E) 18 distinct clusters. Clusters with significantly more LGS events compared to control events are indicated with a star. Consistent cluster centroids, with significantly more LGS events compared to control events, result from a wide range of cluster numbers.

5.3.3 Automated time-frequency analysis identified known and novel candidate biomarkers of LGS

Clusters 1, 2, 3, 4, 5, and 9 contained significantly more events from LGS subjects than control subjects, and thus these events represent potential biomarkers for LGS. Based on the event features and visual analysis of each cluster, several clusters represent known waveforms associated with LGS, such as GPFA and trains of IEDs, while others are novel candidate biomarkers not previously reported in the literature.

5.3.3.1 Events in cluster 1 were exclusively from LGS subjects and were identified as GPFAs

Cluster 1 consisted of 14 events originating from two LGS subjects. These events lasted approximately 1.5 seconds and had notably high height of 45.7 Hz, electrode spread of 52%, and density of 49.6%. The events also had high alpha, sigma, beta, and gamma BP, which were 9,2, 8.6, 9.1, and 3.2 standard deviations greater than the mean event, respectively. Thirteen of the fourteen events were classified by clinicians, of which 100% of events were labelled as GPFA by at least one rater and 61.5% were labelled as GPFA by both raters (Figure 5.9A).

5.3.3.2 Events in clusters 2 and 3 were identified as IEDTs

Events in cluster 2 were exclusively from LGS subjects, consisting of 53 events from four LGS subjects (Figure 5.9B). Similarly, events in cluster 3 originated primarily from LGS subjects, with 341 events from fourteen LGS subjects and 35 control events from nine healthy controls (Figure 5.9C). Clusters 2 and 3 were characterized by high height, length, and spread, with the 17.7-second length of cluster 2 being particularly notable (Figure 5.6). The events in cluster 2 and cluster 3 also had high delta and theta BP, with FPPs of 10.4 Hz and 9.3 Hz, respectively.

In cluster 2, all 48 classified events were labelled as an IEDT by at least one rater; 91.7% of these events were labelled as IEDTs by both raters (Figure 5.9B). LGS events in cluster 3 had similar findings, where 96.2% of events were labelled as IEDT by at least one rater, of which 102 of 128 of these IEDT events had rater agreement (Figure 5.9C). In contrast to LGS events, the control events in cluster 3 only had 40% rater agreement, which consisted of 4 sleep spindles, 1 muscle movement, and 3 events labelled as nothing (Figure 5.9C, right).

5.3.3.3 Cluster 4 revealed alterations to sleep spindles in LGS subjects compared to controls

80.0% of events (437 out of 546) in cluster 4 were LGS events and came from 17 LGS subjects. The notable features of cluster 4 were the height of 40.3 Hz, electrode spread of 49.1%, and FPP of 18.1 Hz (Figure 5.6). Control events were mostly labelled as sleep spindles; 96.2% of events were labelled as sleep spindles by at least one rater, of which 42 of these 50 spindles had rater agreement (Figure 5.9D). In contrast, only 4.8% of LGS events were labelled as sleep spindles by at least one rater, of which only a single event had rater agreement. Overall, 41.0% of LGS events in cluster 4 had rater agreement and labels were predominantly split between various EEG waveforms such as GPFA (n=20), IEDT (n=15), and IED (n=6) (Figure 5.9D).

The drastically reduced detection of sleep spindles in LGS subjects warranted further investigation. In cluster 4, there was only one event in LGS subjects that the raters agreed was a sleep spindle, compared to 42 in controls; across all clusters, there were only five LGS sleep spindles compared to 113 healthy spindles (based on labels with rater agreement). Across all labelled events, LGS sleep spindles had a shorter length, lower height, lower electrode spread, and a lower FPP compared to spindles in healthy controls. An automated sleep spindle detector (Mensen et al. 2018) found that sleep spindles were detected more frequently in healthy controls (n = 96.5 [64.5-123.0]) than LGS subjects (n=25.5 [18.5-44.0]) (Figure 5.10). Moreover, the mean LGS spindle was significantly lower in length, global spread, and peak frequency compared to that of healthy controls ($p<0.05$, Mann-Whitney U-Test , Bonferroni corrected (n=4)) (Figure 5.10). These results mirror those obtained from the time-frequency analysis; both methods suggest sleep spindle occurrence and characteristics as candidate biomarkers of LGS.

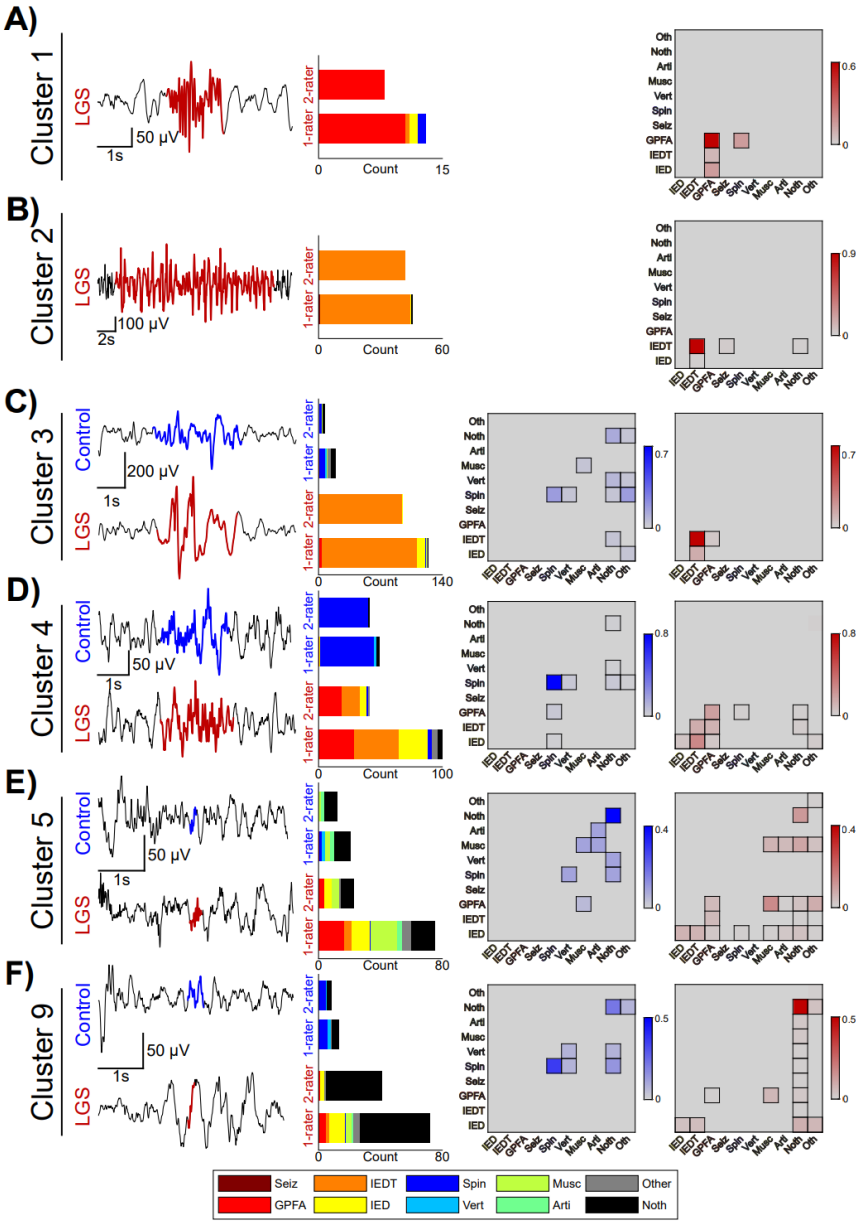

Figure 5.9. Breakdown of reviewer classifications in clusters with significantly more LGS events than control events: (A) Cluster 1, (B) Cluster 2, (C) Cluster 3, (D) Cluster 4, (E) Cluster 5, and (F) Cluster 9. For each cluster, the left column shows a representative example of EEG with features most similar to the cluster centroid for controls (blue) and LGS subjects (red). The bar graph in the middle column shows the occurrence of each label for control and LGS events marked by a single rater or two raters, with the latter indicating rater agreement on the event label. The right column shows the confusion matrices for labels applied to control and LGS events in each cluster.

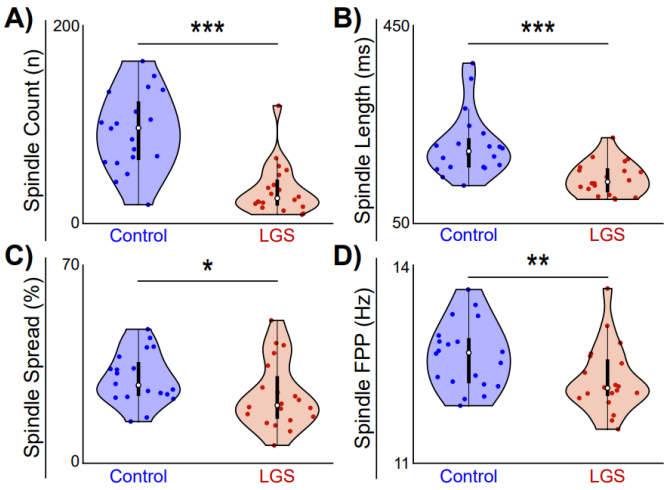

Figure 5.10. Mean features of automatically detected sleep spindles across all control and LGS subjects. Sleep spindles in healthy controls had a significantly greater (A) spindle count, (B) spindle length, (C) spindle spread, and (D) peak frequency compared to spindles in LGS subjects. Significance levels are *p<0.05, **p<0.01, and ***p<0.001, with p-values modified using the Bonferroni method.

5.3.3.4 Beta and gamma frequency events in Clusters 5 and 9 are novel candidate biomarkers of LGS

In total, 91.8% of events in cluster 5 (257 out of 280) were LGS events, originating from 13 subjects; similarly, 77.9% of events in cluster 9 (610 out of 783) were LGS events, originating from 17 subjects. EEG events in clusters 5 and 9 generally had short length, high FPP, and high BP in the beta and gamma bands (Figure 5.6). Between clusters 5 and 9, 81.0% and 77.9% of the viewed events were either labelled as “nothing” or were given mismatched labels by the two raters, respectively (Figure 5.9E, 5.9F). This contrasts the results seen in other clusters with a significantly high ratio of LGS to control events, where LGS events were typically IED, IEDT, or GPFA.

The event labels in cluster 5 were widely varied, with 16.5% of LGS events having rater agreement, consisting of 5 IED, 4 GPFA, 5 muscle, 9 nothing, and 1 other. Control events in cluster 5 had 59.1% rater agreement, consisting of 2 muscle, 2 artifact, and 9 events labelled as nothing (Figure 5.9E). In cluster 9, 56.7% of LGS events had rater agreement, of which 38 of

the 43 events with agreement were labelled as nothing. Only nine control events had rater agreement in cluster 9, consisting of five sleep spindles, one vertex sharp, and 3 events labelled as nothing. Taken together, the fact that these events occur more frequently in LGS subjects than controls, combined with a lack of recognition by clinicians as a known EEG waveform, suggests that these events may be novel candidate biomarkers of LGS.

5.3.4 Analysis of EEG events using feature categorization

As a complement to the clustering analysis, we also placed each event into one of 96 categories by identifying the frequency band with the greatest BP and classifying each event feature as either “low” or “high” relative to the median feature value across all events. The median feature values were a height of 7 Hz, length of 360 milliseconds, spread of 26.3%, and density of 6.4%. A total of 83 of the 96 categories had at least one event, with a mean of 40 events per category ([5.5-162.0] events).

5.3.4.1 Consistent with the clustering analysis, events with high beta and gamma band power are potential biomarkers of LGS

Twenty-two categories had significantly more events from LGS subjects than controls (Table 5.1A; $p<0.05$, permutation test, Bonferroni corrected (n=96). Of these categories, only one had peak band power in the delta band (δHWSD), two in the theta band (θHwSD, θHWsD), two in the alpha band (αHwSd, αHwSD), and two in the sigma band (σHwsD, σHwSD). They were all characterized by events with high height and density; most also had high spread, and all except delta included events with low length. In contrast, there were nine categories with peak BP in the beta band and six categories with peak BP in the gamma band. The beta band categories included a broad representation of events, including high and low values of all features. The gamma band categories all had high density, but included events with high and low height, length, and spread.

This generally suggested that events with peak BP in the beta and gamma bands were indicative of LGS, and the data supported this hypothesis. 84.1% of all events with peak BP in the beta band originated from LGS subjects; this percentage was 78.2% for the gamma band. However, it is interesting to note that, of the sixteen feature categories in the beta band, eight of the categories had no events or only a single event. Seven of the remaining eight categories had significantly more LGS events compared to controls, except for "βhlsd", which had 32 total events and consisted of 65.6% LGS events. The gamma band had similar results, where eleven feature categories had no events or a single event; the other five feature categories contained significantly more LGS events compared to controls (Table 5.1A).

This analysis served as a validation of the clustering results from Section 3.6, as several of the beta and gamma band categories in Table 5.1A overlap with the characteristics of the events in Clusters 5 and 9. A total of 74.3% of events in Cluster 5 had high BP in the gamma band; 100%, 30%, 77%, and 100% of events had heights, lengths, spreads, and densities greater than the median, respectively. Therefore, a majority of Cluster 5 events would be in the γHlSD and γHLSD in categories, which consisted of 337 events with 84.3% LGS events (Table 5.1A, bolded). Similarly, 72.2% of events in Cluster 9 had the highest BP in the beta band, with 78%, 8%, 42%, and 90% of events with heights, lengths, spreads, and densities greater than the median, respectively. These events would be categorized as βHlSD and βHlsD, which consisted of 466 events with 83.3% LGS events (Table 5.1A, italicized). Therefore, both approaches identified the same subset of high frequency EEG waveforms as potential novel biomarkers of LGS.

5.3.4.2 Feature categorization identified EEG events strongly associated with the control group

In addition to feature categories with significantly more LGS events, there were 23 different feature categories with significantly more control events than LGS events. 14 of these

categories and 52.0% of these events had peak BP in the alpha or sigma band (Table 5.1B). Categories associated with control subjects were typically characterized by feature values lower than the median, as 82.8%, 60.7%, 70.3%, and 78.0% of events in the control feature categories had height, length, spread, and density lower than the median, respectively. In contrast to categories associated with LGS, only three feature categories in the beta and gamma band had significantly more control events compared to controls, and each one contained a single event.

Table 5.1. (A) Feature categories with significantly more LGS events compared to control events. Bolded feature categories were representative of events in Cluster 5 and italicized feature categories were representative of events in Cluster 9. (B) Feature categories with significantly more control events compared to LGS events.

A) LGS Feature Categories				**B) Control Feature Categories**		
# Events	**# LGS Event (%)**	**Feature category**		**# Events**	**# LGS Event (%)**	**Feature category**
394	292 (74.1%)	δHLSD		181	48 (26.5%)	δhLSd
57	38 (66.7%)	θHlSD		839	248 (29.6%)	θhlsd
711	463 (65.1%)	θHLSD		371	86 (23.2%)	θhlSd
20	17 (85.0%)	αHlSd		420	71 (16.9%)	θhLSd
109	80 (73.4%)	αHlSD		256	82 (32.0%)	θHLsD
148	83 (56.1%)	σHlsD		144	33 (22.9%)	θHLSd
214	168 (78.5%)	σHlSD		862	217 (25.2%)	αhlsd
77	61 (79.2%)	βhlsD		144	34 (23.6%)	αhlsD
7	7 (100%)	βhlSd		255	79 (31.0%)	αhlSd
39	35 (89.7%)	βhlSD		107	10 (9.4%)	αhLsD
245	*194 (79.2%)*	*βHlsD*		74	13 (17.6%)	αhLSd
1	1 (100%)	βHlSd		82	7 (8.5%)	αhLSD
221	*194 (87.8%)*	*βHlSD*		62	14 (22.6%)	αHLsd
1	1 (100%)	βHLsd		254	53 (20.9%)	αHLsD
17	17 (100%)	βHLsD		327	94 (28.8%)	σhlsd

68	65 (95.6%)	βHLSD		30	5 (16.7%)	σhLsd
6	6 (100%)	γhlsD		27	1 (3.7%)	σhLsD
1	1 (100%)	γhlSD		35	2 (5.7%)	σhLSd
259	180 (69.5%)	γHlsD		65	5 (7.7%)	σhLSD
281	**231 (82.2%)**	**γHlSD**		78	16 (20.5%)	σHLsD
13	12 (92.3%)	γHLsD		1	0 (0%)	βhLsD
56	**53 (94.6%)**	**γHLSD**		1	0 (0%)	γHlsd
				1	0 (0%)	γHlSd

5.4. Discussion

The present study developed a novel application of time-frequency analysis for the discovery of EEG biomarkers in LGS as a test case. Clusters with significantly more LGS to control events were revealed to exclusively contain pathological events such as IEDTs and GPFAs based on the clinical review, serving as an internal validation for this method. Other clusters that contained events predominantly from LGS subjects, but were labelled “nothing” by clinicians, may also have potential as a new biomarker representative of LGS EEG. Our work aims to provide a novel method of EEG review that can discover both preexisting and new biomarkers by using time-frequency characteristics to impartially identify events of interests. This method can be applied outside of LGS cases and help in the diagnosis of any neurological disease relying on the visual review of EEG.

5.4.1 Time-frequency image features

Prior implementations of time-frequency analysis have used various features for EEG event detection. Similar works have implemented time-frequency image analysis on high frequency oscillations, where studies used image features in a support vector machine classifier (Krikid et al. 2022), detected events using different features such as area, entropy, and time/frequency widths (Migliorelli et al. 2020), and also identified events within and outside the

epileptogenic zone (Burnos et al. 2014). Time-frequency analysis has also been used to detect interictal epileptiform discharges in children with focal epilepsies, with increases in power spectrum depending on the region (Jabran et al. 2020), as well as high-frequency changes in intercranial interictal spikes (Jacobs et al. 2011). Our work improves on these prior studies in several ways. First, our method utilizes the joint analysis of patients and controls, while prior studies only analyze patients. This analysis can have clinical relevance as the methods can be applied on subjects that may or may not have a neurological disease. Prior studies also implement fixed event lengths for analysis, whereas our method can detect events of variable length and utilize this as a feature. Our work was also able to identify various EEG waveforms without relying on empirical definitions, preset parameters, or previously marked EEG data. Lastly, this work can identify the characteristics of events that were representative of LGS activity that clinicians often overlook in visual review.

5.4.2 Time-frequency characteristics of GPFAs

Across all clusters, there were 35 events labelled as GPFAs by both raters, and these events came from eight out of the twenty LGS subjects. Previously, generalized paroxysmal fast rhythms in genetic generalized epilepsy patients were reported in 66% of patients using a 24h EEG recording (Seneviratne et al. 2017). Another study using a 24-h EEG recordings reported a median time of 6.5 hours to see the first generalized polyspike activity (Conrad et al. 2022). Therefore, the relative rarity of GFPAs in our dataset was not unexpected, especially given that we analyzed only 10 minutes of sleep EEG and not all detected events were visually labelled.

Events labelled as GPFA were found in six different clusters, with most events coming from clusters 1 and 4. All GPFAs with rater agreement came from a single LGS subject in cluster 1, and six different subjects in cluster 4. GPFAs in cluster 1 had a lower FPP of 12.3 Hz compared to the FPP of 18.7 Hz in cluster 4, and, correspondingly, the alpha and sigma band power of events in cluster 1 were larger than those in cluster 4. This variability in GPFAs is in

line with prior findings, as one study reported GPFAs in video scalp EEG as having a mean amplitude of 293 uV, length of 1.6s, and frequency of 11.1 Hz (Mohammadi et al. 2015), while another study reported mean amplitudes of 88.3 uV, length of 1-4s, and frequencies of 11-20 Hz (Bansal et al. 2019). Another study using automated detection defined GPFAs as a high frequency burst which typically ranged from 8.8-12.6 Hz, but went as low as 3 Hz in some subjects and up to 16-18 Hz in others (Omidvarnia et al. 2021). There are also EEG waveforms such as generalized polyspike trains, that have similar features to GPFA and last less than a second, that are also biomarkers of drug resistance (Cerulli Irelli et al. 2022; Conrad et al. 2022). Future studies may wish to use objective computational methods on EEG spectrograms between and within subjects to help determine the definition of a GPFA.

5.4.3 Physiological and pathological sleep spindles

A total of 118 events were labelled as sleep spindles by both raters; 113 of these spindles came from 18 controls, while five of these came from three LGS subjects. The results using the automated sleep spindle detector demonstrated a similar decrease in spindles in LGS subjects (mean of 93.1 spindles per control subject and 34.3 spindles per LGS subject). Several things may have contributed to this difference. A reduction in spindles has been previously associated with epilepsy, as the rate of global spindles during N2 sleep was lower in focal epilepsy patients compared to controls (Schiller et al. 2022). LGS subjects also have significantly less stage 2 sleep compared to age-matched controls (Eisensehr et al. 2001), which may have biased the number of spindles that occurred during the 10-minute clip of NREM sleep we analyzed. Sleep spindles in LGS may also occur simultaneously with pathological waveforms, which can have a masking effect. Moreover, these types of combined events were probably classified as epileptiform activity, rather than spindles, by the raters.

The results using visual marking and automated detection of sleep spindles both suggested that spindles in control and LGS subjects had different features. The differences in

height, spread, and FPP may be explained by the presence of both fast and slow spindles in the data (Shinomiya et al. 1999a). The FPP of 14.7 Hz for spindles in controls matches the reported frequency of fast spindles (13-15 Hz) (Shinomiya et al. 1999a; Nader and Smith 2015). Control spindles also had a higher electrode spread than LGS spindles. Computational, this would make sense since the spread is calculated relative to the Fz electrode and fast spindles occur in the centroparietal region. Sleep spindles in this frequency range have been attributed to memory and processing speed in healthy individuals (Nader and Smith 2015; Schiller et al. 2022). In contrast, LGS spindles had a FPP of 11.4 Hz and a lower spread, which could represent slow spindles (11-13 Hz) that are typically localized to the frontal region.

5.4.4 Future biomarkers in LGS identification

In addition to finding known EEG waveforms such as GPFAs, IEDs, and sleep spindles in the data, our methods also found potential candidate EEG biomarkers of LGS. Events in clusters 5 and 9 consisted of short EEG segments with high spread, low amplitude, and high relative beta and gamma power. The number of LGS events were significantly greater compared to controls, yet they were unable to be identified as a specific EEG waveform. A total of 100 out of 191 events were labelled as “nothing” by at least one rater.

The feature categorization analysis also found similar results, where events with high relative beta and gamma BP were more likely to be LGS events. The events in clusters 5 and 9 share characteristics with paroxysmal EEG events that were shown to be a biomarker of epileptogenesis in children, which had peak frequencies in the beta and gamma bands and lasted 200 ms or more (Wu et al. 2008). However, we analyzed all events greater than 100 ms, and our results suggested that duration was not a critical feature in distinguishing LGS subjects from controls. The reported events in clusters 5 and 9 were also not muscle artifact, as gamma rhythms during ictal activity have a different morphology compared to muscle (Kobayashi et al. 2009). Overall, we found that feature categorization had complementary results to k-means

clustering while also providing parameters that will not change depending on the cohort. Future studies using time-frequency features can also benefit from feature categorization by comparing the detected event features to our reported median values, which would allow other works to classify their own EEG events in a similar way.

5.4.5 Limitations and future direction

There are several limitations to our study. We detected EEG events only in the Fz channel; our time-frequency method could be adapted to detect events across all channels, although special care would need to be taken to avoid double-counting events that span two or more channels. Additionally, the ten minutes of EEG analyzed for each subject may not have been a representative sample, as prior studies have used recordings up to 24 hours long (Seneviratne et al. 2017; Conrad et al. 2022). The EEG visual analysis provided in the study was also unconventional compared to typical EEG review. While the GUI used for event labelling was designed to mimic standard clinical viewing software, clinicians were only provided the event of interest and an isolated fifteen second clip of EEG surrounding the event. The clinicians were also asked to mark events as short as 100 ms, which may influence some labels since the event is too short to evaluate on its own and the surrounding EEG can influence their decision. Future studies may want to evaluate clinically reviewed EEG in tandem with automated events of interest to compare the two.

We used k-means clustering to differentiate EEG events based on time-frequency features, which provided a broad separation of events with different features but was less effective at differentiating EEG waveforms with overlapping properties, such as sleep spindles and GPFA. Other clustering methods may be able to address this limitation. For example, hierarchical clustering can organize a set of events into subsets that can be arranged at different ordered levels, while k-means requires a pre-determined amount of discrete clusters to separate the events (Köhn and Hubert 2015). Hierarchical clustering can potentially differentiate

a subset of events with multiple EEG waveforms that have similar features, such as GPFA and sleep spindles. While k-means found clusters that contained exclusively GPFAs and IEDTs, future work on differentiating EEG waveforms with similar features may want to use alternate machine learning methods.

5.4.6 Conclusion

Altogether, this study provides a computational approach to EEG biomarker discovery based on the time-frequency features of the signal. By analyzing scalp EEG data obtained from either a healthy or LGS subject, we can automatically detect a set of events without clinical review and compare these events to the event feature within our cohort to identify clinically relevant waveforms. Furthermore, we propose to apply these methods in other neurological diseases, where this work can help evaluate the disease by differentiating healthy and diseased EEG based event categorization, identifying known EEG waveforms, and discovering new EEG biomarkers within the disease.

REFERENCES

Adebimpe A, Aarabi A, Bourel-Ponchel E, Mahmoudzadeh M, Wallois F. EEG resting state analysis of cortical sources in patients with benign epilepsy with centrotemporal spikes. NeuroImage Clin. 2015;9:275–82.

Ahmed B, Redissi A, Tafreshi R. An automatic sleep spindle detector based on wavelets and the teager energy operator. In: 2009 Annual International Conference of the IEEE Engineering in Medicine and Biology Society. 2009. p. 2596–9.

Andrillon T, Nir Y, Staba RJ, Ferrarelli F, Cirelli C, Tononi G, et al. Sleep spindles in humans: Insights from intracranial EEG and unit recordings. J Neurosci. 2011;31(49):17821–34.

Antoniou IE, Tsompa ET. Statistical analysis of weighted networks. Discret Dyn Nat Soc. 2008;2008:375452.

Arzimanoglou A, French J, Blume WT, Cross JH, Ernst JP, Feucht M, et al. Lennox-Gastaut syndrome: a consensus approach on diagnosis, assessment, management, and trial methodology. Lancet Neurol. 2009;8(1):82–93.

Bansal L, Vargas Collado L, Pawar K, Nagesh D, Ilyas M, Hall A, et al. Electroclinical Features of Generalized Paroxysmal Fast Activity in Typical Absence Seizures. J Clin Neurophysiol. 2019;36(1):36–44.

Bastos AM, Schoffelen JM. A tutorial review of functional connectivity analysis methods and their interpretational pitfalls. Front Syst Neurosci. 2016;9(JAN2016):1–23.

Bathelt J, O'Reilly H, Clayden JD, Cross JH, De Haan M. Functional brain network organisation of children between 2 and 5years derived from reconstructed activity of cortical sources of high-density EEG recordings. Neuroimage. 2013;82:595–604.

Baumer FM, McNamara NA, Fine AL, Pestana-Knight E, Shellhaas RA, He Z, et al. Treatment Practices and Outcomes in Continuous Spike and Wave during Slow Wave Sleep: A Multicenter Collaboration. J Pediatr. 2021;232:220–8.

Bellantuono L, Marzano L, La Rocca M, Duncan D, Lombardi A, Maggipinto T, et al. Predicting brain age with complex networks: From adolescence to adulthood. Neuroimage. 2021;225(October 2020):117458.

Berchicci M, Tamburro G, Comani S. The intrahemispheric functional properties of the developing sensorimotor cortex are influenced by maturation. Front Hum Neurosci. 2015;9(FEB).

Berg, Anne; Levy S, Testa F. Evolution and course of early life developmental encephalopathic epilepsies: Focus on Lennox-Gastaut Syndrome. Epilepsia. 2018;59(11):2096–105.

Berg AT, Berkovic SF, Brodie MJ, Buchhalter J, Cross JH, Van Emde Boas W, et al. Revised terminology and concepts for organization of seizures and epilepsies: Report of the ILAE Commission on Classification and Terminology, 2005-2009. Epilepsia. 2010;51(4):676–85.

Blinowska KJ. Review of the methods of determination of directed connectivity from multichannel data. Med Biol Eng Comput. 2011;49(5):521–9.

Blinowska KJ, Kaminski M. Functional brain networks: random, "small world" or deterministic? PLoS One. 2013;8(10).

Boersma M, Smit DJA, De Bie HMA, Van Baal GCM, Boomsma DI, De Geus EJC, et al. Network analysis of resting state EEG in the developing young brain: Structure comes with maturation. Hum Brain Mapp. 2011;32(3):413–25.

Bower BD, Jeavons PM. Infantile Spasms and Hypsarrhythmia. Lancet. 1959 Mar;273(7073):605–9.

Bragin A, Engel J, Wilson CL, Fried I, Buzsáki G. High-frequency oscillations in human brain. Hippocampus. 1999;9(2):137–42.

Britton JW, Frey LC, Hopp JL, Korb P, Koubeissi MZ, Lievens WE, et al. Electroencephalography (EEG): An Introductory Text and Atlas of Normal and Abnormal

Findings in Adults, Children, and Infants. St. Louis EK, Frey LC, editors. Chicago; 2016.
Burnos S, Hilfiker P, Sürücü O, Scholkmann F, Krayenbühl N, Grunwald T, et al. Human intracranial high frequency oscillations (HFOs) detected by automatic time-frequency analysis. PLoS One. 2014;9(4).
Buzsáki G, Horváth Z, Urioste R, Hetke J, Wise K. High-frequency network oscillation in the hippocampus. Science. 1992 May;256(5059):1025–7.
Buzsáki G, Watson BO. Brain rhythms and neural syntax: Implications for efficient coding of cognitive content and neuropsychiatric disease. Dialogues Clin Neurosci. 2012;14(4):345–67.
Camfield PR, Gibson PA, Douglass LM. Strategies for transitioning to adult care for youth with Lennox-Gastaut syndrome and related disorders. Epilepsia. 2011;52:21–7.
Carpels SMA, Yamamoto Y, Mizuno-Matsumoto Y. Graph Theoretical Analysis of Interictal EEG Data in Epilepsy Patients during Epileptiform Discharge and Non-discharge. Int J Affect Eng. 2021;20(3):131–42.
Cerulli Irelli E, Barone FA, Mari L, Morano A, Orlando B, Salamone EM, et al. Generalized Fast Discharges Along the Genetic Generalized Epilepsy Spectrum: Clinical and Prognostic Significance. Front Neurol. 2022;13(March):1–10.
Charupanit K, Lopour BA. A Simple Statistical Method for the Automatic Detection of Ripples in Human Intracranial EEG. Brain Topogr. 2017 Nov;30(6):724–38.
Charupanit K, Sen-Gupta I, Lin JJ, Lopour BA. Detection of anomalous high-frequency events in human intracranial EEG. Epilepsia Open. 2020;5(2):263–73.
Choi HS, Chung YG, Choi SA, Ahn S, Kim H, Yoon S, et al. Electroencephalographic resting-state functional connectivity of benign epilepsy with centrotemporal spikes. J Clin Neurol. 2019;15(2):211–20.
Chu-Shore CJ, Kramer MA, Pathmanathan J, Bianchi MT, Westover MB, Wizon L, et al. Emergence of stable functional networks in long-term human EEG. NIH Public Access. 2012;32(8):2703–13.
Chu CJ, Leahy J, Pathmanathan J, Kramer MA, Cash SS. The maturation of cortical sleep rhythms and networks over early development. Clin Neurophysiol. 2014;125(7):1360–70.
Clemens B, Puskás S, Spisák T, Lajtos I, Opposits G, Besenyei M, et al. Increased resting-state EEG functional connectivity in benign childhood epilepsy with centro-temporal spikes. Seizure. 2016;35:50–5.
Coito A, Genetti M, Pittau F, Iannotti GR, Thomschewski A, Höller Y, et al. Altered directed functional connectivity in temporal lobe epilepsy in the absence of interictal spikes: A high density EEG study. Epilepsia. 2016;57(3):402–11.
Coito A, Plomp G, Genetti M, Abela E, Wiest R, Seeck M, et al. Dynamic directed interictal connectivity in left and right temporal lobe epilepsy. Epilepsia. 2015;56(2):207–17.
Conrad EC, Chugh N, Ganguly TM, Gugger JJ, Tizazu EF, Shinohara RT, et al. Using Generalized Polyspike Train to Predict Drug-Resistant Idiopathic Generalized Epilepsy. J Clin Neurophysiol. 2022;39(6):459–65.
Cross JH, Auvin S, Falip M, Striano P, Arzimanoglou A. Expert opinion on the management of Lennox-Gastaut syndrome: Treatment algorithms and practical considerations. Front Neurol. 2017;8(SEP).
de Curtis M, Jefferys J, Avoli M. Interictal Epileptiform Discharges in Partial Epilepsy. 4th ed. Noebels J, Avoli M, MA R, editors. Bethesda (MD): National Center for Biotechnology Information (US); 2012.
Dalic LJ, Warren AEL, Spiegel C, Thevathasan W, Roten A, Bulluss KJ, et al. Paroxysmal fast activity is a biomarker of treatment response in DBS for Lennox-Gastaut syndrome . Epilepsia. 2022;(September):1–14.
Van Diessen E, Diederen SJH, Braun KPJ, Jansen FE, Stam CJ. Functional and structural brain networks in epilepsy: What have we learned? Epilepsia. 2013;54(11):1855–65.

van Diessen E, Otte WM, Stam CJ, Braun KPJ, Jansen FE. Electroencephalography based functional networks in newly diagnosed childhood epilepsies. Clin Neurophysiol. 2016;127(6):2325–32.
Donos C, Mîndruţă I, Barborica A. Unsupervised Detection of High-Frequency Oscillations Using Time-Frequency Maps and Computer Vision. Front Neurosci. 2020;14:183.
Durka PJ, Klekowicz H, Blinowska KJ, Szelenberger W, Niemcewicz S. A simple system for detection of EEG artifacts in polysomnographic recordings. IEEE Trans Biomed Eng. 2003;50(4):526–8.
Ebus S, Arends J, Hendriksen J, van der Horst E, de la Parra N, Hendriksen R, et al. Cognitive effects of interictal epileptiform discharges in children. Eur J Paediatr Neurol. 2012 Nov 1;16(6):697–706.
Eisensehr I, Parrino L, Noachtar S, Smerieri A, Terzano MG. Sleep in Lennox-Gastaut syndrome: The role oft the cyclic alternating pattern (CAP) in the gate control of clinical seizures and generalized polyspikes. Epilepsy Res. 2001;46(3):241–50.
Fan Y, Shi F, Smith JK, Lin W, Gilmore JH, Shen D. Brain Anatomical Networks in Early Human Brain Development. Neuroimage. 2011;23(1):1–7.
Fernandez LMJ, Lüthi A. Sleep spindles: Mechanisms and functions. Physiol Rev. 2020;100(2):805–68.
Fiest KM, Sauro KM, Wiebe S, Patten SB, Kwon C-S, Dykeman J, et al. Prevalence and incidence of epilepsy: A systematic review and meta-analysis of international studies. Neurology. 2017 Jan;88(3):296–303.
Fisher RS, Acevedo C, Arzimanoglou A, Bogacz A, Cross JH, Elger CE, et al. ILAE Official Report: A practical clinical definition of epilepsy. Epilepsia. 2014;55(4):475–82.
Fonov V, Evans AC, Botteron K, Almli CR, McKinstry RC, Collins DL. Unbiased average age-appropriate atlases for pediatric studies. Neuroimage. 2011;54(1):313–27.
Fries P. A mechanism for cognitive dynamics: neuronal communication through neuronal coherence. Trends Cogn Sci. 2005 Oct;9(10):474–80.
Fries P. Communication Through Coherence (CTC 2.0). Neuron. 2015;88(1):220–35.
Frost Jr JD, Lee CL, Hrachovy RA, Swann JW. High frequency EEG activity associated with ictal events in an animal model of infantile spasms. Epilepsia. 2011/01/04. 2011 Jan;52(1):53–62.
Frost JD, Hrachovy RA. Pathogenesis of infantile spasms: A model based on developmental desynchronization. J Clin Neurophysiol. 2005;22(1):25–36.
Fusco L, Pachatz C, Di Capua M, Vigevano F. Video/EEG aspects of early-infantile epileptic encephalopathy with suppression-bursts (Ohtahara syndrome). Brain Dev. 2001 Nov;23(7):708–14.
Gallop K, Wild D, Nixon A, Verdian L, Cramer JA. Impact of Lennox-Gastaut Syndrome (LGS) on health-related quality of life (HRQL) of patients and caregivers: Literature review. Seizure. 2009;18(8):554–8.
Gao W, Gilmore JH, Giovanello KS, Smith JK, Shen D, Zhu H, et al. Temporal and spatial evolution of brain network topology during the first two years of life. PLoS One. 2011;6(9).
Gardner AB, Worrell GA, Marsh E, Dlugos D, Litt B. Human and Automated Detection of High-Frequency Oscillations. Clin Neurophysiol. 2007a;118(5):1134–43.
Gardner AB, Worrell GA, Marsh E, Dlugos D, Litt B. Human and Automated Detection of High-Frequency Oscillations. Clin Neurophysiol. 2007b;118(118):1134–43.
Garrison KA, Scheinost D, Finn ES, Shen X, Constable RT. The (in)stability of functional brain network measures across thresholds. Neuroimage. 2015;118:651–61.
Gaspard N, Alkawadri R, Farooque P, Goncharova II, Zaveri HP. Automatic detection of prominent interictal spikes in intracranial EEG: validation of an algorithm and relationsip to the seizure onset zone. Clin Neurophysiol Off J Int Fed Clin Neurophysiol. 2014 Jun;125(6):1095–103.

Go CY, MacKay MT, Weiss SK, Stephens D, Adams-Webber T, Ashwal S, et al. Evidence-based guideline update: Medical treatment of infantile spasms: Report of the guideline development subcommittee of the American academy of neurology and the practice committee of the child neurology society. Neurology. 2012;78(24):1974–80.
Goetz P, Hu D, To P, Garner C, Yuen T, Skora C, et al. Scalp EEG markers of normal infant development using visual and computational approaches. In: IEEE Engineering in Medicine and Biology Society. 2021.
Gramfort A, Papadopoulo T, Olivi E, Clerc M. OpenMEEG: opensource software for quasistatic bioelectromagnetics. Biomed Eng Online. 2010;9(1):45.
Grova C, Daunizeau J, Lina JM, Bénar CG, Benali H, Gotman J. Evaluation of EEG localization methods using realistic simulations of interictal spikes. Neuroimage. 2006;29(3):734–53.
Gruber R, Wise MS. Sleep Spindle Characteristics in Children with Neurodevelopmental Disorders and Their Relation to Cognition. Neural Plast. 2016;2016.
Haartsen R, van der Velde B, Jones EJH, Johnson MH, Kemner C. Using multiple short epochs optimises the stability of infant EEG connectivity parameters. Sci Rep. 2020;10(1):12703.
Halford JJ, Schalkoff RJ, Zhou J, Benbadis SR, Tatum WO, Turner RP, et al. Standardized database development for EEG epileptiform transient detection: EEGnet scoring system and machine learning analysis. J Neurosci Methods. 2013;212(2):308–16.
Hallgren KA. Computing Inter-Rater Reliability for Observational Data: An Overview and Tutorial. Tutor Quant Methods Psychol. 2012;8(1):23–34.
Hallquist MN, Hillary FG. Graph theory approaches to functional network organization in brain disorders: A critique for a brave new small-world. Netw Neurosci. 2018;3(1):1–26.
Hayashi Y, Yoshinaga H, Akiyama T, Endoh F, Ohtsuka Y, Kobayashi K. Predictive factors for relapse of epileptic spasms after adrenocorticotropic hormone therapy in West syndrome. Brain Dev. 2016;38(1):32–9.
He B, Astolfi L, Valdes-Sosa PA, Marinazzo D, Palva SO, Benar CG, et al. Electrophysiological Brain Connectivity: Theory and Implementation. IEEE Trans Biomed Eng. 2019;66(7):2115–37.
Hermoye L, Saint-Martin C, Cosnard G, Lee SK, Kim J, Nassogne MC, et al. Pediatric diffusion tensor imaging: Normal database and observation of the white matter maturation in early childhood. Neuroimage. 2006;29(2):493–504.
van den Heuvel MP, de Lange SC, Zalesky A, Seguin C, Yeo BTT, Schmidt R. Proportional thresholding in resting-state fMRI functional connectivity networks and consequences for patient-control connectome studies: Issues and recommendations. Neuroimage. 2017;152(December 2016):437–49.
Van Den Heuvel MP, Pol HEH. Exploring the brain network: A review on resting-state fMRI functional connectivity. Eur Neuropsychopharmacol. 2010;20(8):519–34.
Horita H, Kumagai K, Maekawa K. Overnight polygraphic study of Lennox-Gastaut syndrome. Brain Dev. 1987;9(6):627–35.
Horstmann MT, Bialonski S, Noennig N, Mai H, Prusseit J, Wellmer J, et al. State dependent properties of epileptic brain networks: Comparative graph-theoretical analyses of simultaneously recorded EEG and MEG. Clin Neurophysiol. 2010;121(2):172–85.
Hrachovy RA, Frost JD. Infantile Epileptic Encephalopathy with Hypsarrhythmia (Infantile Spasms/West Syndrome). J Clin Neurophysiol. 2003;20(6):408–25.
Hu DK, Goetz PW, To PD, Garner C, Magers AL, Skora C, et al. Evolution of Cortical Functional Networks in Healthy Infants. Front Netw Physiol. 2022;2(June):1–12.
Hu DK, Mower A, Shrey DW, Lopour BA. Effect of interictal epileptiform discharges on EEG-based functional connectivity networks. Clin Neurophysiol. 2020a;131(5):1087–98.
Humphries MD, Gurney K. Network “small-world-ness”: A quantitative method for determining canonical network equivalence. PLoS One. 2008;3(4).
Hussain SA, Kwong G, Millichap JJ, Mytinger JR, Ryan N, Matsumoto JH, et al. Hypsarrhythmia

assessment exhibits poor interrater reliability: a threat to clinical trial validity. Epilepsia. 2015 Jan;56(1):77–81.
Jabran Y, Mahmoudzadeh M, Martinez N, Heberlé C, Wallois F, Bourel-Ponchel E. Temporal and Spatial Dynamics of Different Interictal Epileptic Discharges: A Time-Frequency EEG Approach in Pediatric Focal Refractory Epilepsy. Front Neurol. 2020;11(September):1–13.
Jacobs J, Kobayashi K, Gotman J. High-frequency changes during interictal spikes detected by time-frequency analysis. Clin Neurophysiol. 2011;122(1):32–42.
Jacobs J, Zijlmans M. HFO to Measure Seizure Propensity and Improve Prognostication in Patients With Epilepsy. Epilepsy Curr. 2020;20(6):338–47.
Janati AB, ALGhasab NS, Aldaife MY, Khan R, Khan I, Abdullah A, et al. Atypical Interictal Epileptiform Discharges in Electroencephalography. J Epilepsy Res. 2018;8(2):55–60.
Jiang X, Bian G Bin, Tian Z. Removal of artifacts from EEG signals: A review. Sensors (Switzerland). 2019;19(5):1–18.
Jing J, Herlopian A, Karakis I, Ng M, Halford JJ, Lam A, et al. Interrater Reliability of Experts in Identifying Interictal Epileptiform Discharges in Electroencephalograms. JAMA Neurol. 2020;77(1):49–57.
Jiruška P, Prokš J, Drbal O, Sovka P, Marusi PČ, Mareš P. Comparison of Different Methods of Time Shift Measurement in EEG. 2005;459–65.
Kane N, Acharya J, Benickzy S, Caboclo L, Finnigan S, Kaplan PW, et al. A revised glossary of terms most commonly used by clinical electroencephalographers and updated proposal for the report format of the EEG findings. Revision 2017. Clin Neurophysiol Pract. 2017;2:170–85.
Karoly PJ, Freestone DR, Boston R, Grayden DB, Himes D, Leyde K, et al. Interictal spikes and epileptic seizures: Their relationship and underlying rhythmicity. Brain. 2016;139(4):1066–78.
Keezer MR, Sisodiya SM, Sander JW. Comorbidities of epilepsy: Current concepts and future perspectives. Lancet Neurol. 2016;15(1):106–15.
Khan S, Al Baradie R. Epileptic Encephalopathies: An Overview. Epilepsy Res Treat. 2012;2012:1–8.
Kim HJ, Kim HD, Lee JS, Heo K, Kim DS, Kang HC. Long-term prognosis of patients with Lennox-Gastaut syndrome in recent decades. Epilepsy Res. 2015;110:10–9.
Kivity S, Lerman P, Ariel R, Danziger Y, Mimouni M, Shinnar S. Long-term Cognitive Outcomes of a Cohort of Children with Cryptogenic Infantile Spasms Treated with High-dose Adrenocorticotropic Hormone. Epilepsia. 2004;45(3):255–62.
Knupp KG, Coryell J, Nickels KC, Ryan N, Leister E, Loddenkemper T, et al. Response to Treatment in a Prospective National Infantile Spasms Cohort. Ann Neurol. 2016;79(3):475–84.
Kobayashi K, Inoue T, Watanabe Y, Oka M, Endoh F, Yoshinaga H, et al. Spectral analysis of EEG gamma rhythms associated with tonic seizures in Lennox-Gastaut syndrome. Epilepsy Res. 2009;86(1):15–22.
Köhn H, Hubert LJ. Hierarchical Cluster Analysis. Wiley StatsRef Stat Ref Online. 2015;1–13.
Koles ZJ. Trends in EEG source localization. Electroencephalogr Clin Neurophysiol. 1998;106(2):127–37.
Kramer MA, Cash SS. Epilepsy as a disorder of cortical network organization. Neuroscientist. 2012;18(4):360–72.
Kramer MA, Eden UT, Cash SS, Kolaczyk ED. Network inference with confidence from multivariate time series. Phys Rev E - Stat Nonlinear, Soft Matter Phys. 2009;79(6):1–12.
Krikid F, Karfoul A, Chaibi S, Kachenoura A, Nica A, Kachouri A, et al. Classification of High Frequency Oscillations in intracranial EEG signals based on coupled time-frequency and image-related features. Biomed Signal Process Control. 2022;73(November 2021).
Kybic J, Clerc M, Abboud T, Faugeras O, Keriven R, Papadopoulo T. A Common Formalism for

the Integral Formulations of the Forward EEG Problem. IEEE Trans Med Imaging. 2005;24;1;12-28.
Lai N, Li Z, Xu C, Wang Y, Chen Z. Diverse nature of interictal oscillations: EEG-based biomarkers in epilepsy. Neurobiol Dis. 2023;177(December 2022):105999.
Latka M, Kozik A, Jernajczyk J, West BJ, Jernajczyk W. Wavelet mapping of sleep spindles in young patients with epilepsy. J Physiol Pharmacol an Off J Polish Physiol Soc. 2005 Sep;56 Suppl 4:15–20.
Lloyd SP. Least Squares Quantization in PCM. IEEE Trans Inf Theory. 1982;28(2):129–37.
Louis EKS, Frey LC, Britton JW, Hopp JL, Korb PJ, Koubeissi MZ, et al. Electroencephalography (EEG): An Introductory Text and Atlas of Normal and Abnormal Findings in Adults, Children, and Infants. Chicago: American Epilepsy Society; 2016.
Lux AL, Edwards SW, Hancock E, Johnson AL, Kennedy CR, Newton RW, et al. The United Kingdom Infantile Spasms Study comparing vigabatrin with prednisolone or tetracosactide at 14 days: a multicentre, randomised controlled trial. Lancet (London, England). 2004 Nov;364(9447):1773–8.
Mahmoudzadeh M, Wallois F, Aarabi A, Adebimpe A, Bourel-Ponchel E. EEG Resting State Functional Connectivity Analysis in Children with Benign Epilepsy with Centrotemporal Spikes. Front Neurosci. 2016;10(March):1–9.
Markand ON. Slow spike-wave activity in EEG and associated clinical features. Neurology. 1977 Aug 1;27(8):746 LP – 746.
Mastrangelo M. Lennox-Gastaut Syndrome: A State of the Art Review. Neuropediatrics. 2017a Jun;48(3):143–51.
Mastrangelo M. Lennox – Gastaut Syndrome : A State of the Art Review. 2017b;.
Matos J, Peralta G, Heyse J, Menetre E, Seeck M, van Mierlo P. Diagnosis of Epilepsy with Functional Connectivity in EEG after a Suspected First Seizure. Bioengineering. 2022;9(11):1–21.
McGraw KO, Wong SP. Forming Inferences about Some Intraclass Correlation Coefficients. Psychol Methods. 1996;1(1):30–46.
McHugh ML. Lessons in biostatistics interrater reliability : the kappa statistic. Biochem Medica. 2012;22(3):276–82.
McTague A, Howell KB, Cross JH, Kurian MA, Scheffer IE. The genetic landscape of the epileptic encephalopathies of infancy and childhood. Lancet Neurol. 2016 Mar;15(3):304–16.
Mehraram R, Kaiser M, Cromarty R, Graziadio S, O'Brien JT, Killen A, et al. Weighted network measures reveal differences between dementia types: An EEG study. Hum Brain Mapp. 2020;41(6):1573–90.
Mensen A, Poryazova R, Huber R, Bassetti CL. Individual spindle detection and analysis in high-density recordings across the night and in thalamic stroke. Sci Rep. 2018;8(1):1–11.
Migliorelli C, Bachiller A, Alonso JF, Romero S, Aparicio J, Jacobs-Le Van J, et al. SGM: A novel time-frequency algorithm based on unsupervised learning improves high-frequency oscillation detection in epilepsy. J Neural Eng. 2020;17(2).
Miskovic V, Ma X, Chou CA, Fan M, Owens M, Sayama H, et al. Developmental changes in spontaneous electrocortical activity and network organization from early to late childhood. Neuroimage. 2015;118:237–47.
Mohamed BP, Scott RC, Desai N, Gutta P, Patil S. Seizure outcome in infantile spasms-A retrospective study. Epilepsia. 2011;52(4):746–52.
Mohammadi M, Okanishi T, Okanari K, Baba S, Sumiyoshi H, Sakuma S, et al. Asymmetrical generalized paroxysmal fast activities in children with intractable localization-related epilepsy. Brain Dev. 2015;37(1):59–65.
Mölle M, Bergmann TO, Marshall L, Born J. Fast and slow spindles during the sleep slow oscillation: Disparate coalescence and engagement in memory processing. Sleep.

2011;34(10):1411–21.
Monaco A, Amoroso N, Bellantuono L, Lella E, Lombardi A, Monda A, et al. Shannon entropy approach reveals relevant genes in Alzheimer's disease. PLoS One. 2019;14(12):1–29.
Moretti D V., Babiloni F, Carducci F, Cincotti F, Remondini E, Rossini PM, et al. Computerized processing of EEG-EOG-EMG artifacts for multi-centric studies in EEG oscillations and event-related potentials. Int J Psychophysiol. 2003;47(3):199–216.
Moshé SL, Perucca E, Ryvlin P, Tomson T. Epilepsy: New advances. Lancet. 2015;385(9971):884–98.
Murakami N, Ohtsuka Y, Ohtahara S. Early infantile epileptic syndromes with suppression-bursts: early myoclonic encephalopathy vs. Ohtahara syndrome. Jpn J Psychiatry Neurol. 1993 Jun;47(2):197–200.
Mytinger JR, Hussain SA, Islam MP, Millichap JJ, Patel AD, Ryan NR, et al. Improving the inter-rater agreement of hypsarrhythmia using a simplified EEG grading scale for children with infantile spasms. Epilepsy Res. 2015 Oct;116:93–8.
Nader RS, Smith CT. Correlations between adolescent processing speed and specific spindle frequencies. Front Hum Neurosci. 2015;9(FEB):1–8.
Nariai H, Wu JY, Bernardo D, Fallah A, Sankar R, Hussain SA. Interrater reliability in visual identification of interictal high-frequency oscillations on electrocorticography and scalp EEG. Epilepsia Open. 2018;3(S2):127–32.
Nayak CS, Anilkumar AC. EEG Normal Waveforms. In StatPearls. StatPearls Publishing; 2023.
Ohtahara S, Yamatogi Y. Epileptic encephalopathies in early infancy with suppression-burst. J Clin Neurophysiol Off Publ Am Electroencephalogr Soc. 2003;20(6):398–407.
Olejarczyk E, Marzetti L, Pizzella V, Zappasodi F. Comparison of connectivity analyses for resting state EEG data. J Neural Eng. 2017;14(3).
Omidvarnia A, Fransson P, Metsäranta M, Vanhatalo S. Functional bimodality in the brain networks of preterm and term human newborns. Cereb Cortex. 2014;24(10):2657–68.
Omidvarnia A, Warren AEL, Dalic LJ, Pedersen M, Jackson G. Automatic detection of generalized paroxysmal fast activity in interictal EEG using time-frequency analysis. Comput Biol Med. 2021;133:104287.
Onnela JP, Saramäki J, Kertész J, Kaski K. Intensity and coherence of motifs in weighted complex networks. Phys Rev E - Stat Nonlinear, Soft Matter Phys. 2005;71(6):1–4.
Ortiz E, Stingl K, Müninger J, Braun C, Preissl H, Belardinelli P. Weighted phase lag index and graph analysis: Preliminary investigation of functional connectivity during resting state in children. Comput Math Methods Med. 2012;186353.
Osborne JP, Lux AL, Edwards SW, Hancock E, Johnson AL, Kennedy CR, et al. The underlying etiology of infantile spasms (West syndrome): Information from the United Kingdom Infantile Spasms Study (UKISS) on contemporary causes and their classification. Epilepsia. 2010;51(10):2168–74.
Pavone P, Striano P, Falsaperla R, Pavone L, Ruggieri M. Infantile spasms syndrome, West syndrome and related phenotypes: what we know in 2013. Brain Dev. 2014 Oct;36(9):739–51.
Pellock JM, Hrachovy R, Shinnar S, Baram TZ, Bettis D, Dlugos DJ, et al. Infantile spasms: A U.S. consensus report. Epilepsia. 2010;51(10):2175–89.
Piña-Garza JE, Montouris GD, Vekeman F, Cheng WY, Tuttle E, Giguere-Duval P, et al. Assessment of treatment patterns and healthcare costs associated with probable Lennox–Gastaut syndrome. Epilepsy Behav. 2017;73:46–50.
Ponten SC, Douw L, Bartolomei F, Reijneveld JC, Stam CJ. Indications for network regularization during absence seizures: Weighted and unweighted graph theoretical analyses. Exp Neurol. 2009;217(1):197–204.
Primec ZR, Stare J, Neubauer D. The risk of lower mental outcome in infantile spasms increases after three weeks of hypsarrhythmia duration. Epilepsia. 2006;47(12):2202–5.

Quraan MA, McCormick C, Cohn M, Valiante TA, McAndrews MP. Altered Resting State Brain Dynamics in Temporal Lobe Epilepsy Can Be Observed in Spectral Power, Functional Connectivity and Graph Theory Metrics. PLoS One. 2013;8(7).
Rai D, Kerr MP, McManus S, Jordanova V, Lewis G, Brugha TS. Epilepsy and psychiatric comorbidity: A nationally representative population-based study. Epilepsia. 2012;53(6):1095–103.
Reus EEM, Cox FME, van Dijk JG, Visser GH. Automated spike detection: Which software package? Seizure. 2022;95(December 2021):33–7.
Riikonen R. Long-term outcome of patients with West syndrome. Brain Dev. 2001 Nov;23(7):683–7.
Riikonen RS. Favourable prognostic factors with infantile spasms. Eur J Paediatr Neurol EJPN Off J Eur Paediatr Neurol Soc. 2010 Jan;14(1):13–8.
Rijckevorsel K. Treatment of Lennox-Gastaut syndrome: overview and recent findings. Neuropsychiatr Dis Treat. 2008 Dec;4(6):1001.
Roehri N, Lina JM, Mosher JC, Bartolomei F, Benar CG. Time-Frequency Strategies for Increasing High-Frequency Oscillation Detectability in Intracerebral EEG. IEEE Trans Biomed Eng. 2016;63(12):2595–606.
Romero Milà B, Remakanthakurup Sindhu K, Mytinger JR, Shrey DW, Lopour BA. EEG biomarkers for the diagnosis and treatment of infantile spasms. Front Neurol. 2022;13.
Rosenberg RS, Van Hout S. The American Academy of Sleep Medicine inter-scorer reliability program: Sleep Stage Scoring. J Clin Sleep Med. 2013;9(1):81–7.
Rubinov M, Sporns O. Complex network measures of brain connectivity: Uses and interpretations. Neuroimage. 2010;52(3):1059–69.
Sanfeliu A, Fu K-S. A distance measure between attributed relational graphs for pattern recognition. IEEE Trans Syst Man Cybern. 1983;SMC-13(3):353–62.
Schabus M, Dang-Vu TT, Albouy G, Balteau E, Boly M, Carrier J, et al. Hemodynamic cerebral correlates of sleep spindles during human non-rapid eye movement sleep. Proc Natl Acad Sci U S A. 2007;104(32):13164–9.
Scheffer IE, Berkovic S, Capovilla G, Connolly MB, French J, Guilhoto L, et al. ILAE classification of the epilepsies: Position paper of the ILAE Commission for Classification and Terminology. Epilepsia. 2017;58(4):512–21.
Schiller K, Avigdor T, Abdallah C, Sziklas V, Crane J, Stefani A, et al. Focal epilepsy disrupts spindle structure and function. Sci Rep. 2022;12(1):1–11.
Sela M, Arnon R, Schechter B, Ferreira C, Deslandes A, Moraes H, et al. Electroencephalography: An introductory Text and Atlas. Vol. 62, Cerebral Cortex. 2002.
Seneviratne U, Cook MJ, D'Souza WJ. Electroencephalography in the diagnosis of genetic generalized epilepsy syndromes. Front Neurol. 2017;8(SEP).
Sheng S, Nalleballe K, Yadala S. EEG Benign Variants. In Treasure Island (FL); 2023.
Shields WD. Infantile Spasms: Little Seizures, BIG Consequences. Epilepsy Curr. 2006;6(3):63–9.
Shinomiya S, Nagata K, Takahashi K, Masumura T. Development of sleep spindles in young children and adolescents. Clin Electroencephalogr. 1999a Apr;30(2):39–43.
Shinomiya S, Nagata K, Takahashi K, Masumura T. Development of Sleep Spindles in Young Children and Adolescents. Clin EEG Neurosci. 1999b;30(2):39–43.
Shrey DW, Kim McManus O, Rajaraman R, Ombao H, Hussain SA, Lopour BA. Strength and stability of EEG functional connectivity predict treatment response in infants with epileptic spasms. Clin Neurophysiol. 2018a;129(10):2137–48.
Siems M, Siegel M. Dissociated neuronal phase- and amplitude-coupling patterns in the human brain. Neuroimage. 2020;209(January):116538.
Sillanpää M, Shinnar S. Long-Term Mortality in Childhood-Onset Epilepsy. N Engl J Med. 2010;363(26):2522–9.

Siniatchkin M, Van Baalen A, Jacobs J, Moeller F, Moehring J, Boor R, et al. Different neuronal networks are associated with spikes and slow activity in hypsarrhythmia. Epilepsia. 2007;48(12):2312–21.
Smit DJA, Boersma M, Schnack HG, Micheloyannis S, Boomsma DI, Hulshoff Pol HE, et al. The brain matures with stronger functional connectivity and decreased randomness of its network. PLoS One. 2012;7(5).
Smith RJ, Alipourjeddi E, Garner C, Maser AL, Shrey DW, Lopour BA. Infant functional networks are modulated by state of consciousness and circadian rhythm. Netw Neurosci. 2021a;:1–17.
Smith RJ, Hu DK, Shrey DW, Rajaraman R, Hussain SA, Lopour BA. Computational characteristics of interictal EEG as objective markers of epileptic spasms. Epilepsy Res. 2021b;176(May):106704.
Smith RJ, Shrey DW, Hussain SA, Lopour BA. Quantitative Characteristics of Hypsarrhythmia in Infantile Spasms. Annu Int Conf IEEE Eng Med Biol Soc IEEE Eng Med Biol Soc Annu Int Conf. 2018 Jul;2018:538–41.
Smith RJ, Sugijoto A, Rismanchi N, Hussain SA, Shrey DW, Lopour BA. Long-Range Temporal Correlations Reflect Treatment Response in the Electroencephalogram of Patients with Infantile Spasms. Brain Topogr. 2017 Nov;30(6):810–21.
Smith SJM. EEG in the diagnosis, classification, and management of patients with epilepsy. J Neurol Neurosurg Psychiatry. 2005;76:ii2–7.
Specchio N, Wirrell EC, Scheffer IE, Nabbout R, Riney K, Samia P, et al. International League Against Epilepsy classification and definition of epilepsy syndromes with onset in childhood: Position paper by the ILAE Task Force on Nosology and Definitions. Epilepsia. 2022;63(6):1398–442.
Sporns O. Graph theory methods: Applications in brain networks. Dialogues Clin Neurosci. 2018;20(2):111–20.
Staley KJ, White A, Dudek FE. Interictal spikes: harbingers or causes of epilepsy? Neurosci Lett. 2011 Jun;497(3):247–50.
Stamps FW, Gibbs EL, Rosenthal IM, Gibbs FA. Treatment of hypsarhythmia with ACTH. J Am Med Assoc. 1959 Sep;171:408–11.
Stockwell RG. Localization of the complex spectrum: the s transform. IEEE Trans Signal Process. 1996;44(4):993.
Stockwell RG, Mansinha L, Lowe RP. Localization of the complex spectrum: the S transform. IEEE Trans Signal Process. 1996;44(4):998–1001.
Symonds JD, Elliott KS, Shetty J, Armstrong M, Brunklaus A, Cutcutache I, et al. Early childhood epilepsies: epidemiology, classification, aetiology, and socio-economic determinants. Brain. 2021 Oct;144(9):2879–91.
Tadel F, Baillet S, Mosher JC, Pantazis D, Leahy RM. Brainstorm: A user-friendly application for MEG/EEG analysis. Comput Intell Neurosci. 2011;2011:1–13.
Tao JX, Baldwin M, Hawes-Ebersole S, Ebersole JS. Cortical substrates of scalp EEG epileptiform discharges. J Clin Neurophysiol. 2007;24(2):96–100.
Taylor PN, Goodfellow M, Wang Y, Baier G. Towards a large-scale model of patient-specific epileptic spike-wave discharges. Biol Cybern. 2013;107(1):83–94.
Tokariev A, Videman M, Palva MJ, Vanhatalo S. Functional brain connectivity develops rapidly around term age and changes between vigilance states in the human newborn. Cereb Cortex. 2016;26(12):4540–50.
Tóth B, Urbán G, Háden GP, Márk M, Török M, Stam CJ, et al. Large-scale network organization of EEG functional connectivity in newborn infants. Hum Brain Mapp. 2017;38(8):4019–33.
Ung H, Cazares C, Nanivadekar A, Kini L, Wagenaar J, Becker D, et al. Interictal Epileptiform Activity Outside the Seizure Onset Zone Impacts Cognition. Brain. 2017;18(140):2157–68.

Usui S, Amidror I. Digital low-pass differentiation for biological signal processing. IEEE Trans Biomed Eng. 1982 Oct;29(10):686–93.
Usui S, Amidror I. Digital Differentiation Filters for Biological Signal Processing. Int Ser Biomech. 1983;4 B(10):1207–14.
Vértes PE, Bullmore ET. Annual research review: Growth connectomics--the organization and reorganization of brain networks during normal and abnormal development. J Child Psychol Psychiatry. 2015 Mar;56(3):299–320.
Vinck M, Oostenveld R, Van Wingerden M, Battaglia F, Pennartz CMA. An improved index of phase-synchronization for electrophysiological data in the presence of volume-conduction, noise and sample-size bias. Neuroimage. 2011;55(4):1548–65.
Watts DJ, Strogatz SH. Strogatz - small world network. Nature. 1998;393(June):440–2.
Wheless JW, Constantinou JEC. Lennox-Gastaut Syndrome. 1997;17(97):203–11.
van Wijk BCM, Stam CJ, Daffertshofer A. Comparing brain networks of different size and connectivity density using graph theory. PLoS One. 2010;5(10).
Wilke C, Worrell G, He B, Baak JP, Mutter GL, Robboy S, Van Diest PJ, Uyterlinde AM, Ørbo A, Palazzo J, Fianne B, Løvslett K, Burger C, Voorhorst F VR. Graph analysis of epileptogenic networks in human partial epilepsy. Epilepsia. 2011 Jan;52(1):84–93.
Wu JY, Koh S, Sankar R, Mathern GW. Paroxysmal fast activity: an interictal scalp EEG marker of epileptogenesis in children. Epilepsy Res. 2008 Nov;82(1):99–106.
Xie W, Mallin BM, Richards JE. Development of brain functional connectivity and its relation to infant sustained attention in the first year of life. Dev Sci. 2019;22(1):1–18.
Yamada K, Toribe Y, Kimizu T, Kimura S, Ikeda T, Mogami Y, et al. Predictive value of EEG findings at control of epileptic spasms for seizure relapse in patients with West syndrome. Seizure. 2014;23(9):703–7.
Yap PT, Fan Y, Chen Y, Gilmore JH, Lin W, Shen D. Development trends of white matter connectivity in the first years of life. PLoS One. 2011;6(9).
Zuberi SM, Wirrell E, Yozawitz E, Wilmshurst JM, Specchio N, Riney K, et al. ILAE classification and definition of epilepsy syndromes with onset in neonates and infants: Position statement by the ILAE Task Force on Nosology and Definitions. Epilepsia. 2022;63(6):1349–97.